COMPUTATIONAL STUDY OF NOBLE METAL ALLOYS

ADEWUMI ISAAC POPOOLA

A THESIS SUBMITTED TO THE FACULTY OF SCIENCE,
UNIVERSITY OF THE WITWATERSRAND, JOHANNESBURG,
IN FULFILLMENT OF THE REQUIREMENTS FOR THE DEGREE
OF DOCTOR OF PHILOSOPHY

May 4, 2013

Declaration

I, Adewumi Isaac POPOOLA, declare that this thesis is my own work, unless otherwise acknowledged. It is being submitted for the degree of Doctor of Philosophy in Physics at the University of the Witwatersrand, Johannesburg. It has not been submitted before for any degree or examination in any other University.

_____

(Signature of candidate)

____ day of _____ 20____

Abstract

The elastic constants, phase stability, heat of formation and the Debye temperature of various noble metal compounds in the stoichiometry A_3B (where A = Pt, Ir, Rh, Ru, Pd and B = Al, Hf, Zr, Sc) were studied using the *ab initio* Density Functional Theory - Projector Augmented Wave method. A total of 24 compositions was investigated, of which 16 compounds were predicted to be thermodynamically stable. The remaining eight compounds were found not energetically favorable, due to positive or low heats of formation. According to the Density of States studies, the $L1_2$ structure was predicted in 8 compounds while four compounds had the $D0_{24}$ structure. Among compounds with the $L1_2$ structure, the hardest phase predicted was $L1_2$-Ir_3Hf. $L1_2$-Pd_3Sc was predicted as the least hard and most ductile compound. In compounds with the $D0_{24}$ structure, Pt_3Zr was predicted having highest hardness and highest melting point. In all the compounds, the strongest interaction was found between hafnium and the noble metals and least interaction was with aluminum. The melting points from *ab initio* and molecular dynamics calculations slightly over-predicted experimental values, but showed the same trends. Both the fracture toughnesses and the melting points deduced

using the Sutton-Chen potentials had similar trends to *ab initio* results, suggesting that the Sutton-Chen potentials is adequate for simulating metallic phases.

Acknowledgments

I would like to acknowledge the guidance and support I have received from my supervisors Prof. J.E. Lowther, Prof. L.A. Cornish, Prof. I.A. Fuwape and Dr. L.H. Chown. My life and career are enlightened with the trust and freedom with which I have worked with all of you during the last two academic years. I also want to thank every individual who contributed in one way or the other to the success of this study - no names mentioned, but none ignored.

The African Materials Science and Engineering Network (AMSEN), a Carnegie-RISE Network is profoundly thanked for funding this study. For as long as we both live, I shall remain indebted to my spouse **Margaret**. I thank you for taking good care of our little angels - **Jessica** and **Jarret** while away on this study. I hope you will all forgive me for denying you my presence and warmth, I love you all. Finally, unto him (God) that is able to do abundantly above all I can ever dare to think or imagine be the glory for ever and ever.

The following have been presented based on this work:

1. A.I. Popoola and J.E. Lowther, Structural properties of noble metal alloys (1^{ST} African Material Science and Engineering Network Workshop, Windhoek, 27-29 January, 2010) [**Oral presentation**].

2. A.I. Popoola and J.E. Lowther, Structure and Stability of X_3Al noble metal alloys (3^{RD} Wits University Postgraduate Cross Faculty Symposium, 26-29 October, 2010) [**Oral presentation**].

3. A.I. Popoola and J.E. Lowther, Hard Metal Alloys - A study of some noble metal compounds, (South African Department of Science and Technology/National Research Foundation Annual Workshop, Johannesburg, May 2011) [**Oral presentation**].

4. A.I. Popoola, J.E. Lowther, L.H. Chown and L.A. Cornish, Elastic properties and high temperature behavior of Pt_xAl_y phases relative to Ni_3Al (Institute of Physics (CMMP11), Manchester, 12-15 December, 2011) [**Oral presentation**].

5. A.I. Popoola, L.H. Chown and L.A. Cornish, Density Functional Calculations of Selected Platinum Phases (2^{ND} African Material Science and Engineering Network Workshop, Nairobi, 20-23 March, 2012) [**Oral presentation**].

6. A.I. Popoola, L.H. Chown and L.A. Cornish, Theoretical investigation of the Pt_3X (X = Al, Sc, Hf, Zr) ground state (South African Department of Science and Technology/National Research Foundation Annual Workshop, Johannesburg, May 2012) [**Poster presentation**].

Patent:

Advanced aluminum based alloys

A. I. Popoola and J. E. Lowther

Provisional Patent No 2010/03649 (first registered 25/05/2010)

Submitted for publication:

Computational study of Platinum Group Superalloys

A. I. Popoola and J. E. Lowther

In loving memory of my late father

Solomon Olajiga POPOOLA

Sun re o baba omo titi di ojo ajinde.

Contents

List of Figures

List of Tables

Chapter 1

Introduction

With fast computers and efficient algorithms, it is now possible to design and understand many new material properties. In designing and optimizing refractory alloys, difficulties are usually encountered. The experimental data needed on the physical, thermodynamics and mechanical properties of most new alloy systems are lacking. There are also difficulties with the processing of refractory alloys, due to high temperature requirements in their experimental preparation and synthesis. Theoretical modeling has been introduced to compliment experimental alloy development so as to avoid the traditional "trial and error" material preparation approach, which is time consuming and expensive.

The formulation and development of Quantum Theory in the 20^{th} century has led to the understanding of many aspects of the properties of condensed matter. Material properties are determined by the interaction of its constituent atoms. To make specific predictions for real materials and to design new materials, a detailed understanding of the interaction of

these atoms is important. Thereafter, properties such as hardness, structure stability etc. of a system are obtainable. Density Functional Theory [1, 2, 3, 4] has provided an important theoretical foundation for modern first principles quantum calculation of materials properties.

Many physical properties of a material can be evaluated using an *ab initio* methods or semi-empirical approach. Both methods obtain the total energy and atomic structure of interacting electrons and nuclei. In a semi-empirical modeling approach, significant information is required about the atomic interaction (force fields etc) of the system under investigation. On the other hand, *ab initio* describes a modeling method in which little or no knowledge exists about the system. The number of atoms that *ab initio* method can handle is limited by computer time and resource although an *ab initio* methods has the capability to provide direct information of various properties.

In systems where large numbers of atoms are involved, Molecular Dynamics (MD) is the preferred modeling technique. The semi-empirical molecular dynamics is an approach that makes use of inter-atomic potentials. It is an established tool to evaluate many material properties, and can be used to investigate and understand the structures of complex systems even at the atomic level [5, 6, 7].

Commercially, pure metals are rarely used. They are used in the form of an alloy according to their required physical properties. A desired property can be achieved by changing the metallic composition of the alloy. Atomic ordering controls basic properties like conductivity

and hardness [8]. Intermetallic compounds are materials consisting of metals in approximate stoichiometry ratios in ordered crystal structures. Intermetallics based on the aluminides are particularly attractive, because they have high oxidation and corrosion resistance, low density, high strength, and stiffness at elevated temperatures [9]. These exceptional properties had encouraged the interest at developing improved high-temperature structural materials. Most currently used high-temperature intermetallics are alloys in which an intermetallic compound also served as the strengthening phase [10].

1.1 Literature Review

1.1.1 Intermetallic Compounds

The property of an intermetallic compound is determined by its crystal structure. For pure metals, crystal structure and site occupations are limited. The structure for the majority of pure metals are body-centered cubic (bcc), face-centered cubic (fcc), and hexagonal close-packed (hcp). These structure types are shown in Figure 1.1.

The face-centered cubic structure (fcc) consists of an atom at each cube corner and an atom in the center of each cube face. About 20% of the elements in the periodic table crystallize with face centered cubic structures. Each atom in the fcc lattice has 12 nearest-neighbors. For atoms of same size, the fcc has the closed pack arrangement of atoms. The distance along the unit cell edges is called the lattice parameter, a. For cubic crystals, the lattice parameter

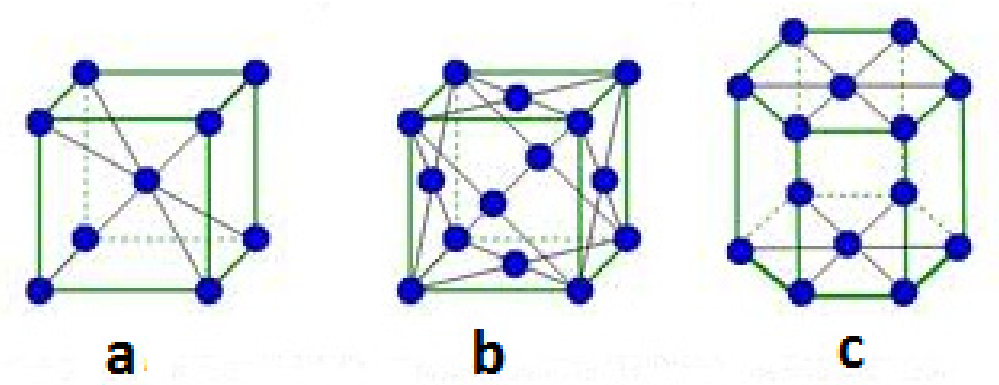

Figure 1.1: Common structure types in metallic elements a: bcc, b: fcc and c: hcp

is identical in all three crystal axes. In the body centered cubic structure, atoms exist at each cube corner and one atom is at the center of the cube. A comparison of the fcc and bcc structures shows that the bcc is less dense than the fcc structure. In contrast to fcc, bcc has only 8 nearest neighbors. The hexagonal structure comprises close packed planes.

Both fcc and hcp have closed-packed planes, and the difference is the stacking sequence. As shown in Figure 1.2 [11], there are two types of plane positions for the hcp structure, with an alternating ABAB arrangement. Conversely, three types of plane positions with the ABCABC arrangement is adopted in the fcc structure. For hcp, atoms of the third plane are in exactly the same position as the atoms in the first plane, while for fcc, atoms in rows A and C do not align. Slip occur more easily on close-packed planes. Although both fcc and hcp have closed-packed planes, there is only one set in hcp and four sets in fcc. Thus, slip can occur in almost any direction in fcc and on only one plane in hcp. This makes slip easier in fcc.

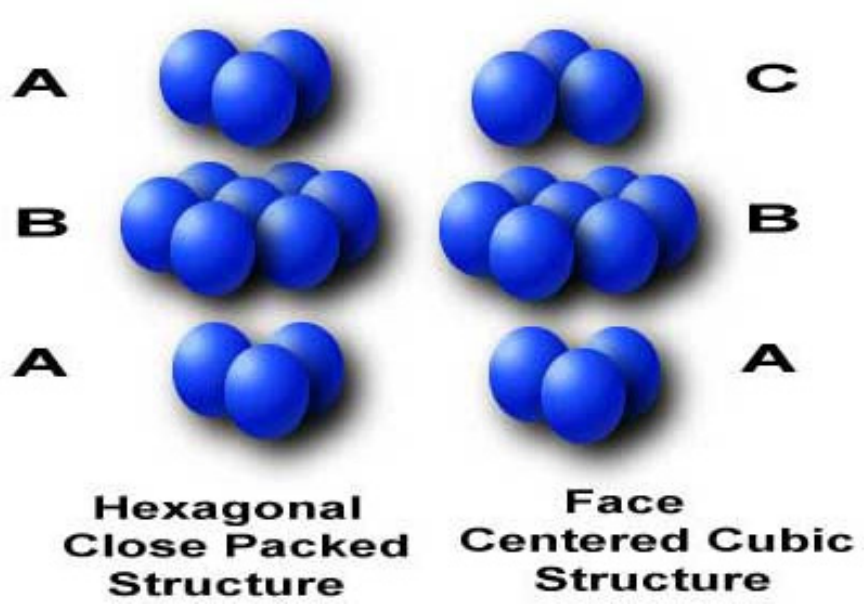

Figure 1.2: Stacking arrangements in fcc and hcp crystal structures. Adapted from [11].

When metals are alloyed together, some alloy systems exhibit complete solid solubility while others show limited solubility. The limits of solubility are determined by series of rules called Hume-Rothery rules [12, 13]. Three types of alloys (*substitutional, interstitial and transformational*) can be distinguished. In substitutional alloys, the solute substitutes the solvent in the crystal lattice without structural changes. In interstitial alloys, the solute does not occupy the sites in the lattice of the solvent but resides in crystallographic pores. In transformational alloys, a completely new lattice is formed and this occurs as a result of random arrangement of atoms in the final lattice. In solid solution, specific atoms occupy specific lattice sites, giving rise to either; ordered, disordered (random) or clustered lattices. These arrangements [14] are shown in Figure 1.3.

All heat engine performance increases with the temperature of the working fluid, the limiting

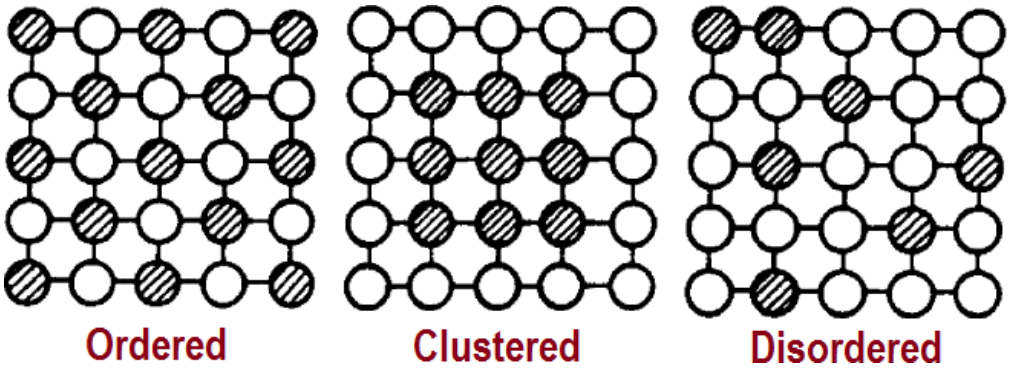

Figure 1.3: Arrangement of solute atoms in ordered, clustered and random lattices. Adapted from [14].

temperature is set by the melting temperature of available materials. Since the late 1940's, nickel-based superalloys (NBSAs) have been used as vanes and blade components in engines and gas turbine generators. The success of the NBSAs in these demanding applications is due to their excellent high melting temperatures, oxidation resistance and high yield stress [15]. To date, Ni_3Al is the most studied NBSA. The strength of Ni_3Al increases with temperature [16]. In properly controlled stoichiometry, Ni_3Al also has good ductility both in single crystal [17] and polycrystalline form [18].

In the Ni_3Al structure, Al atoms reside on the cube corners, while Ni atoms are located on the cube faces. The structure of Ni_3Al is designated as $L1_2$ in the Strukturbericht notation or as $cP4$ in the Pearson's symbol [19]. The $cP4$ (space group: $Pm\overline{3}m$) notation indicates a cubic (c) primitive (P) structure with four (4) atoms per unit cell. In an ordered $L1_2$ binary structure, the atomic ratio is A_3B, where each B atom is surrounded by twelve A atoms. Some examples of intermetallic structures are shown in Figure 1.4. The $L1_0$, $L1_2$ and B2 structures are highly symmetrical. Properties like strength and yield stress are determined by

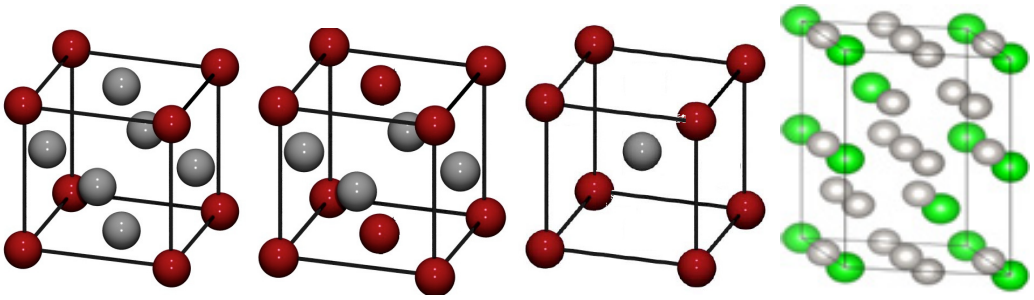

Figure 1.4: Some crystal structure of intermetallic compounds; left to right: Cu_3Au ($L1_2$), CuAu ($L1_0$), B2 and $D0_{24}$ structures.

the degree of ordering in an AB binary compound. Dislocation barriers are easily achievable in these structure types. Ordering has more A-B bonds than A-A or B-B bonds. The tendency to have more A-B bonds is determined by A atoms having more B atoms as nearest neighbors. Since unlike atoms are favored over like atoms as nearest neighbors, the chances are that any intermetallic compound where A-B bonds are more will have more strength and may retain its structure to the melting point.

1.1.2 PGM compounds with $L1_0$, $L1_2$, B2 and $D0_{24}$ structures

Although NBSAs have excellent properties, they are currently used at about 85% of their melting temperature [15]. For this reason, other materials that make use of the precepts of the NBSAs, but have higher melting temperatures are required. Among the first considerations were ceramics based on tungsten, niobium and molybdenum. The choice of these materials was based purely on high melting points and strength. However, alloys based on these refractory metals were found to suffer from creep and oxidation even at low temperatures [20]. Ceramics suffer from much lower toughness and are costlier to process than the NBSAs

[21].

Intermetallics based on the noble metals, especially the platinum group metals (PGMs), were proposed [22], and have been studied [20, 23]. Apart from the high melting point of the platinum group metals, they mostly have the fcc structure like nickel and good oxidation resistance. Pt-based alloys have received considerable attention [20, 23, 24], as a possible replacement for nickel based superalloy components. Platinum has higher melting point (1796 °C) compared to 1455 °C for Ni. It has the face centered cubic crystal structure and excellent environmental stability [25]. The major drawbacks to the use of Pt are its cost and high density. However, Pt is recyclable which could compensate for its high cost [26] and its density could also be reduced by alloying it with light-weight elements suggesting it can still find applications in the aerospace industry [27].

Listed in Table 1.1 [28] are PGM compounds with $L1_0$, $L1_2$, B2 and $D0_{24}$ structures. When $L1_2$ is distorted tetragonally, then the $L1_0$ structure is obtained. When $c = a$, the atoms are located at the positions of a face centered cubic lattice. The space group for $L1_0$ structure is P4/mmm (no. 123). It's Pearson symbol is $tP2$. The Pearson symbol for B2 compound is $cP2$ [29] with a space group of $Pm\overline{3}$m (no. 221). The stoichiometric formula for the $D0_{24}$ structure is AB_3 [30]. The structure belongs in the hexagonal system, with the abac stacking sequence. Its space group notation is $P6_3/mmc$ (no. 194). The $D0_{24}$ crystal structure is asymmetric.

Considerable experimental efforts showed that the densities of many of the alloys in Table 1.1 are above 10, except in rhodium and ruthenium-based B2 compounds. Although low density will allow considerable weight savings, these compounds may still qualify as good structural materials on account of their high melting points.

Normal temperature-hardness behavior was demonstrated by Rh_3Ti, Ir_3Ti, Ir_3Cr, Ir_3Hf and Ir_3V while anomalous strength behavior was found in Rh_3Nb, Rh_3Ta, Ir_3Nb and Ir_3Zr [31, 32, 33, 34]. The melting temperatures of $L1_2$-rhodium-based compounds was found to be lower than $L1_2$-iridium-based compounds, while their density was almost half of $L1_2$-iridium-based compounds. In addition to their low densities, the specific strengths of rhodium-based alloys were almost equivalent to those of iridium alloys. Strength improvement with element addition (ternary alloying) was found promising in Ir-based alloys [35, 36, 37], while it was ineffective in rhodium alloys [38, 39, 40, 35]. Rhodium-based alloys had better ductility - 25% for Rh-Nb and 35% for Rh-Ti, while at room temperature, the ductility of most iridium alloys were below 10% [41, 42, 43]. Currently, the hardness of Iridium-based superalloys are at about 200 MPa at 2,073 K [44, 45].

Iridium-based alloys are inherently brittle. An improvement in ductility from 10% (binary) to about 20% (quaternary alloy) have been achieved [46, 47, 48, 49, 50]. Two kinds of $fcc + L1_2$ in the quaternary alloys [51] showed higher strength compared with iridium or rhodium-based binary alloys. Although the deformation mechanism in these quaternary alloys are yet to be reported, the various results suggested that a combination of iridium and rhodium may be a

Table 1.1: Crystal structure, melting temperature (MT), and density of some noble metal-based compounds [28].

Compd.	Structure	MT(K)	Density (g.cm^{-3})
$IrNb$	$L1_0$	2,173	15.25
$Ru_{11}Ta_9$	$L1_0$	2,353	14.41
$IrAl$	B2	2,393	-
$RuAl$	B2	2,333	7.97
$RuSc$	B2	2,473	7.40
$RuTi$	B2	2,393	8.55
$RhTi$	B2	2,213	8.5
Ir_3Hf	$L1_2$	2,743	>20
Ir_3Ta	$L1_2$	2,727	>20
Ir_3Nb	$L1_2$	2,708	18.5
Ir_3Zr	$L1_2$	2,553	18.0
Ir_3Ti	$L1_2$	2,388	18.5
Ir_3V	$L1_2$	2,373	18.5
Rh_3Ta	$L1_2$	2,730	14.0
Rh_3Nb	$L1_2$	2,236	11.7
Rh_3Zr	$L1_2$	2,173	11.0
Rh_3Ti	$L1_2$	2,023	10.5
Rh_3V	$L1_2$	2,013	11.0
Pt_3Al	$L1_2$	1,829	-
Pt_3Zr	$D0_{24}$	2,427	18.0

promising way of designing next generation of high temperature materials [52, 53].

Currently, the main area of application for platinum alloys are in the glass industries. The hardness of platinum is enhanced in these applications with little rhodium addition, in a process called 'oxide dispersion-strenghtening technique' [39, 54]. Significant progress have been made by many research groups at developing Pt-based alloys with higher temperature mechanical strength comparable to most Ni-based superalloys. Many platinum-based $L1_2$ compounds including Pt_3Ti, Pt_3Cr, Pt_3In, Pt_3Ga, and Pt_3Sn showed anomalous temperature dependence of strength, while Pt_3Al showed normal temperature dependence [55, 56]. The fcc/$L1_2$ microstructure similar to the NBSA have been achieved in the Pt-Al system [57]. Further study have shown that the Pt-Al-X system has the best oxidation resistance [24, 58].

With this discovery, more work has been done on the Pt-Al alloys. It is now a common knowledge that $L1_2$-Pt_3Al transforms to a Pt_3Ga-type phase at low temperature [48, 49, 50]. Stabilization effort was also reported [57]. Cuboidal $L1_2$ precipitates, similar to what is obtained in the nickel-based superalloys is also exhibited in the fcc-platinum matrix phase. Both chromium and ruthenium have been found to improve the strength of Pt-Al system and this improvement was better than conventional platinum oxide-dispersion-strengthened (ODS) alloys [54, 56]. At high temperatures, $L1_2$ precipitation-hardened alloys are suggested with better properties than platinum-ODS alloys.

The compound, RuAl, is a highly promising alloy with the B2-structure. It has high melting

point, good oxidation resistance, good strength at elevated temperatures and useful fracture toughnesses [24]. Other reported compounds with the B2 structure includes IrAl, RhAl and RhAl-X (X = B, Co, Fe, Ti, Ni, and Ir). With additional elements (ternary alloying), these alloys maintained their B2 microstructure. Creep resistance was however found to worsen with ternary alloying. Oxidation resistance improved with Iridium alloyed with aluminium [59] and an increase in iridium content from NiAl to IrAl showed an increase in the creep rate [60]. The strength for IrAl was higher than in NiAl, $L1_2$-Ni_3Al, and $L1_0$-TiAl [59, 60]. At higher temperatures, the strength of B2-IrAl was lower than that of its equivalent $L1_2$ phase. Ductility was better in B2-IrAl alloys than in the $L1_2$ alloys. Although the ductility of B2 compounds (e.g. IrAl) improves slightly with additional elements, their creep properties also get worsened drastically [61, 62, 63].

1.1.3 PGM compounds from electronic structure calculations

The advent of density functional theory (DFT) has made it possible to describe many properties of materials. In combination with methods such as the linear muffin-tin orbital (LMTO) [64], the Korringa-Kohn-Rostocker (KKR) [65] the twenty most stable noble metal compounds have been predicted [66]. These compounds (listed in Table 1.2) were predicted based on the ab-initio calculation of their stability/heat of formation ($\triangle H_f$). Stability is a microscopic quantity, that reflects the quantum properties of the electrons in a system. It can be used as a criteria to determine whether a material can exist by thermodynamic means. Structure stability is directly calculable from electronic structure theory, because to

a large extent, it determines the resistance of the alloy to different kinds of applied external conditions - stress, high temperature, or irradiation. While the results of Table 1.2 is a display of efficient methods based on DFT, it is also a pointer to new possibilities. For example, further investigations of the Pt - Sc system [67], have confirmed Pt_3Sc to exist with an ordered $L1_2$ structure up to the melting point of (1850 °C). When compared with Ni_3Al and Ir_3Nb (Table 1.3), the calculated anisotropy and the elastic moduli of Pt_3Sc suggests that it should combine good strength with exceptional ductility. Moreover, the melting temperature of Pt_3Sc (1850 °C) is small compared with the melting temperature of Iridium based alloys such as Ir_3Nb. However, despite the higher temperature margin between Pt_3Sc and Iridium alloys, the ductility of Pt-Sc alloys is an advantage over the brittleness of Ir-based alloys.

Among the noble metals, rhodium based alloys have attracted much attention both from experimental and first principle investigations. Firstly, rhodium is a fcc metal with high melting point and compounds based on rhodium can be easily prepared with a microstructure similar to that of nickel based superalloys [71]. Additionally, density in rhodium based compounds is found to be less than that of the individual elements of the platinum group [34]. The oxidation resistance property in rhodium based alloys is also found to be superior to the other compounds [41]. Rhodium-based intermetallics of the type A_3B where A = Rh and B = Ti, Ta, Hf, Zr and Nb have been studied by electronic structure calculations [72]. These compounds are found to crystallize in Cu_3Au structure type, with the space group symmetry of $Pm\overline{3}m$. The theoretically calculated equilibrium lattice and bulk moduli (Table 1.4) indicated that the compound with highest bulk modulus was Rh_3Ta and Rh_3Hf

Table 1.2: The twenty fcc most stable alloys [66].

Alloys	$\triangle H_f$(eV/atom)
Pt_3Sc	-1.06
Pt_3Hf	-1.03
Pt_3Y	-1.02
$PdPt_2Sc$	-0.99
Pt_3Zr	-0.98
Pt_2RhHf	-0.98
$PdPt_2Y$	-0.97
$PdPt_2Hf$	-0.96
Pt_3Lu	-0.95
Pt_2RhSc	-0.94
$NiPt_2Sc$	-0.93
Pt_2RhZr	-0.92
$NiPt_2Hf$	-0.92
$PdPt_2Lu$	-0.92
$PdPt_2Zr$	-0.92
$PtPd_2Sc$	-0.91
IrPtRhHf	-0.90
$PtPd_2Y$	-0.90
$PtRh_2Hf$	-0.88
Ir_3Hf	-0.88

Table 1.3: Comparison of calculated bulk modulus B (GPa), Young modulus E (GPa), shear modulus G (GPa), B/G ratio, Poisson's ratio (v), and anisotropy constant (A_G) of Pt_3Sc , Ni_3Al, Pt_3Al and Ir_3Nb

Alloys	B	E	G	B/G	v	A_G	Refs
Pt_3Sc	246.2	203.6	74.7	3.30	0.36	0.93	[67]
Ni_3Al	173.9	203.1	77.8	2.24	0.30	3.49	[68]
Ir_3Nb	379.3	630.6	257.8	1.47	0.22	1.60	[69]
Pt_3Al	292.3	330.5	126.4	2.31	0.34	1.30	[70]

Table 1.4: Lattice parameter and bulk moduli of rhodium based compounds [72], experimental data in parentheses.

Alloys	Lattice parameter($\mathring{A}$)	Bulk Modulus (GPa)
Rh_3Ti	7.169 (7.227)	287.2
Rh_3Zr	7.356 (7.426)	277.0
Rh_3Nb	7.242 (7.289)	315.7
Rh_3Hf	7.346 (7.389)	274.8
Rh_3V	7.086 (7.154)	319.6
Rh_3Ta	7.251 (7.297)	326.3

having the least bulk modulus. As much as the equilibrium lattice parameter of these alloys compared well with experimental values, there are at present no experimental data to compare with the bulk moduli. This problem, which is evident with most noble metal compounds have hampered the possibility to verify theoretical results. It is therefore strongly suggested that an experimental study of the elastic properties of most noble metal compounds needs to be undertaken. While the constitution and properties of many binary noble metal compounds have been investigated, little has been done to characterize the ternary systems. Possible ternary systems are listed in Table 1.5.

Table 1.5: Possible ternary systems of the noble metals

$Pt-Rh-Pd$	$Pt-Rh-Ir$	$Pt-Rh-Os$	$Pt-Rh-Ru$	$Pt-Pd-Ir$
$Pt-Os-Pd$	$Pt-Pd-Ir$	$Pt-Pd-Ru$	$Pt-Ir-Ru$	$Pt-Os-Ir$
$Pt-Ru-Os$	$Pd-Rh-Ir$	$Pd-Rh-Os$	$Pd-Rh-Ru$	$Pd-Ru-Ir$
$Rh-Ru-Ir$	$Rh-Ru-Os$	$Ir-Ru-Os$	$Rh-Ir-Os$	$Pd-Os-Ir$

1.2 Motivation

In view of previous discussions, the noble metals have been found to form solid solution with other elements, resulting in many structure types. The melting points of these compounds are high, but with density mostly above 10. Mostly, the compounds have high melting points, yet strength and creep resistance remains a concern. In this research therefore, calculation efforts was on noble metal alloys with aluminum as well as their alloys with scandium, zirconium and hafnium. The structure primarily considered for simulation was the A_3B ($L1_2$), similar to Ni_3Al. This structure type is highly ordered and therefore, many defect types - defects of substitution, antiphase boundaries, super partial dislocations etc, should contribute to higher strength and fracture toughness properties of the material [73, 74].

The intention of the present research, was to use the *ab initio* quantum mechanical calculation methods to derive the heats of formation, elastic properties and the phase stability of some noble metal alloys in the stoichiometry A_3B (where A = Pt, Ir, Rh, Pd, Ru and B = Hf, Zr, Sc, Al). Some of the compounds covered are known in literature, while many others are yet to be described. The results would elucidates more on what is known and make information available regarding the unknown.

1.3 Aims and Objective

The aim is to employ *ab initio* quantum mechanical as well as empirical molecular dynamics simulations to study the mechanical properties of an alloy formed between the platinum group metals and aluminum, hafnium, zirconium or scandium in the stoichiometry A_3B (where A = Pt, Ir, Rh, Pd, Os and B = Al, Sc, Zr, Hf). Comparing results from the two approaches, predictions will be made based on the stability of various phases of the noble metal alloys.

The specific objectives are to:

1. use *ab initio* quantum mechanical DFT approach to calculate the heats of formation, elastic moduli and total DOS for the A_3B compounds.
2. use empirical molecular dynamics to simulate and compare the melting point and high temperature bulk moduli trend in the A_3Al compounds.
3. use available codes and force fields; VASP 5.2 (*ab initio* DFT) and DL-POLY 4.2 (molecular dynamics).
4. compare results from the two approaches (where available) with experimental data.
5. make predictions based on results from step 4.

All calculations were carried out with the computing facilities at the School of Physics, University of the Witwatersrand. The Sutton-Chen inter-atomic potential (S-C) will be used to study the melting points of some of the alloys. Among other things, the results would show how valid the S-C potential is in simulating melting points in metallic phases. Doing so,

particularly, without any additional empirical fittings. The structure of choice was the $L1_2$, where the interest was to have this phase maintained over the melting temperature regime of the compounds.

1.4 The Noble Metals

Reviewed in this section, are the various noble metals that form the basis for the compounds investigated in this research.

1.4.1 Platinum

Platinum is a metal that belongs in group 10 of the Periodic Table of elements. It is silvery-white in appearance and is malleable and ductile [75]. It possesses high resistance to chemical attack [76]. Platinum is very scarce, its occurrence is only about 0.003 ppb in the Earth's crust. It is often found chemically combined with other metals in alluvial deposits. Platinum alloys are widely used as catalysts in catalytic converters due to their outstanding catalytic properties. They are also used to make fine jewelry because they are highly resistant to wear and tarnish. The stable electrical properties of platinum are also exploited for many industrial applications. Platinum has the face-centered cubic crystal structure with the following additional properties: Young's modulus =168 GPa, Shear modulus = 61 GPa, Bulk modulus = 230 GPa, Poisson ratio = 0.38, Mohs hardness = 4 - 4.5 [77, 78].

1.4.2 Rhodium

Rhodium is a silvery-white, hard transition metal. It is chemically inert and has only one isotope (^{103}Rh) in its naturally occurring state. It is one of the rarest and currently the most expensive noble metal. Rhodium is usually found in platinum ores. Its reflectance is high and it does not form an oxide, even when heated. At its melting point, it readily absorbs oxygen which is released on solidification. It is less dense than platinum, but having a melting point (1964 °C) higher than platinum (1768 °C). It is resistant to acids; it is completely insoluble in nitric acid. The most use for rhodium is presently as alloying agent to harden platinum or palladium. A platinum or palladium alloy hardened with rhodium can be used as high-temperature corrosion-resistant coatings [79]. It is used in nuclear reactors to measure neutron flux levels. The crystal structure of rhodium is face-centered cubic. Its additional structural properties are: Young's modulus = 380 GPa, Shear modulus = 150 GPa, Bulk modulus = 275 GPa, Poisson ratio = 0.26 and Mohs hardness = 6.0.

1.4.3 Iridium

Iridium is a silvery-white transition metal. It is brittle and having a density second to osmium. At extremely high temperatures ($\sim$ 2000 °C), Iridium is the most corrosion-resistant metal. Due to its rarity, it is employed only in a number of specialized industrial and scientific applications where high corrosion resistance at high temperatures is required[80]. Some key areas of use of iridium are in spark plugs, crucibles for recrystallization of semiconductors,

electrodes for the production of chlorine in the chloralkali process, and as thermoelectric generators in spacecraft [79]. To date, iridium is the only metal believed to have the potential to maintain its good mechanical properties at temperatures well above 1600 °C [81]. It has a face-centered cubic structure with the following moduli parameters: Bulk modulus = 320 GPa, Young's modulus = 528 GPa, Shear modulus = 210 GPa, Poisson's ratio = 0.26 and Mohs hardness = 6.5.

1.4.4 Palladium

Palladium is a chemical element belonging in group 10 of the Periodic Table of elements. It was discovered in 1803 and it is a lustrous silvery-white metal [82]. Palladium is a rare metal, and about 70% of the world's supply comes from the North-Western Province in South Africa. Out of all the PGMs, Palladium is the least dense and has the lowest melting point. Presently, half of the world supply of palladium goes into catalytic converters. It is also widely used in the manufacture of computers, mobile phones, ceramic capacitors, component plating, low voltage electrical contacts, and LCD televisions screens. It is also actively used in medicine, especially in dentistry [79]. Hydrogen and groundwater purification is another important area of application for palladium. It also has the potential to play a key role in the technology of fuel cells. The structure of palladium is face-centered cubic, with a space group of $Fm\overline{3}m$. Its elastic properties are as follows; Young's modulus: 121 GPa, Shear modulus: 44 GPa, Bulk modulus: 180 GPa and Poisson's ratio: 0.39 [78, 83].

1.4.5 Ruthenium

Ruthenium is an element found in group 8 of the Periodic Table. It is very rare and mostly found with other PGM ores [82]. It is a hard, white metal, which does not tarnish at normal temperatures, but can oxidize at high temperatures on exposure to air to form ruthenium tetroxide, RuO_4. Ruthenium is resistant to acids [80, 84] and its addition to other metals can increase the hardness and corrosion resistance of the alloy [79]. The crystal structure of ruthenium is hexagonal with the following moduli parameters[83, 78]; Young's modulus = 447 GPa, Shear modulus = 173 GPa, Bulk modulus = 220 GPa, Poisson's ratio = 0.30 and Mohs hardness of 6.5.

1.4.6 Osmium

Osmium is a PGM, with the chemical symbol Os and atomic number 76 [82, 83]. Osmium is hard but brittle. It is the densest natural element found in nature, mostly in platinum ores. It has low vapor pressure (the lowest of the platinum group metals) and very high melting point (the fourth highest of all elements). The last makes metallic osmium difficult to manufacture and the brittleness means it is difficult to machine. The structure of osmium is hexagonal with extremely high bulk modulus (B). Osmium is reported with a B value between 395 and 462 GPa, which rivals that of diamond (443 GPa)[85]. Osmium has a low shear modulus, which is only 222 GPa [86, 87, 88]. Osmium applications and research are hampered because on exposure to air it emits osmium tetroxide (OsO_4)[89], which smells

bad and is very poisonous. Osmium is primarily used where frictional wear minimization is required. Application arrears include point pen tips, fountain pen tips, record player needles, electrical contacts etc.

The outline of the remaining part of the thesis is as follows; Chapter 2 describes the *ab initio* DFT concepts and merits of various approximations presently used to implement DFT calculations. The various methods for obtaining equilibrium properties from *ab initio* DFT calculations are discussed in chapter 3. The results of the *ab initio* calculation on noble-metal-aluminide intermetallic compounds X_3Al (where X = Pt, Ir, Rh, Os, Pd, Ru) are presented in Chapter 4. The molecular dynamics (MD) concepts are introduced in Chapter 5 with results obtained on the lattice parameter, bulk modulus, density and the melting points of the X_3Al compounds. The *ab initio* results on other X_3B compounds (where B = Sc, Hf, Zr) are presented in Chapter 6. In chapter 7, conclusions were made based on results obtained and an outlook for further work given.

Chapter 2

Ab Initio DFT Calculations

2.1 Introduction

In material physics, the first step in evaluating the properties of a material is to obtain the energy of the system. This is done by solving the time-independent Schrödinger equation [90]. The Schrödinger equation (Equation 2.1), is the most fundamental equation of quantum mechanics. The equation can only be numerically solved for few atoms. To make useful progress, the equation is solved using a series of approximations. The approximation route basically replaces the original equation with simpler ones. As much as possible, essential features of the original system are captured by these simpler equations, although the approximated equations are sometimes difficult to justify.

$$\hat{H}\Psi = E\Psi \qquad \text{(Equation 2.1)}$$

where $\hat{H}$ = Hamiltonian describing electrons and nuclei

Ψ = wave function and

E = energy of the system.

The first approximation, aimed at solving the Schrödinger equation usually decouples the electron motion from that of heavier ions. This is known as the Born and Oppenheimer approximation [91]. Following the isolation of the ions from the electrons, the ions can thereafter be treated as classical particles because it now provides a fixed potential. The Hamiltonian for this approximation can be written as:

$$\hat{H} = -\left(\frac{\hbar^2}{2m}\right)\sum_i \nabla_i^2 + \frac{1}{2}\sum_{i\neq j}\frac{e^2}{\mid r_i - r_j \mid} - \sum_{i,p}\frac{e^2 Z_p}{\mid r_i - r_p \mid} \qquad \text{(Equation 2.2)}$$

where, r_i and m are the electron co-ordinates and mass respectively, r_p is the nuclei coordinates, while eZ_p is the charge of constituent nuclei.

The Hartree approximation is a further refinement on the Born and Oppenheimer method, devised to solve the Schrödinger equation. The total wave function is written as the product of single electron wave functions (Equation 2.3), after which the variational principle is applied [92], to obtain the Hartree equation (Equation 2.4).

$$\Psi(r_1, r_2.....r_z) = \psi_1 r_1, \psi_2 r_2.....\psi_z r_z \qquad \text{(Equation 2.3)}$$

$$\left[-\frac{\hbar^2}{2m_i}\nabla_i^2 - \frac{Ze^2}{r_i} + e^2 \sum_{j \neq i} \int d^3 r_j \frac{\mid \psi_j(\overrightarrow{r_j}) \mid^2}{\overrightarrow{r_i} - \overrightarrow{r_j}} \right] \psi_i \overrightarrow{r_i} = \epsilon_i \psi_i \overrightarrow{r_i} \qquad \text{(Equation 2.4)}$$

The ϵ_i in Equation 2.4 represents the energy contribution of the i^{th} electron. The potential due to the other electrons in which the i^{th} electron moves is represented by:

$$e^2 \sum_{j \neq i} \int d^3 r_j \frac{\mid \psi_j(\overrightarrow{r_j}) \mid^2}{\overrightarrow{r_i}} \qquad \text{(Equation 2.5)}$$

Though, electron-electron interactions are easier to study within the electric field created by other electrons, the Hartree equation does not account for Pauli exclusion principle and as such, any calculation based on it is not reliable [90].

A better formalism is achieved when all orthonormal one-particle wave functions in Equation 2.4 are expressed with antisymmetric wave-functions [93]. With this, the Pauli exclusion principle is obeyed. The simplest possible type of antisymmetric wave function is obtained by antisymmetrizing all orthonormal one-particle wave functions ie.:

$$\Psi(\mathbf{r}_1, \ldots, \mathbf{r}_a, \ldots, \mathbf{r}_b, \ldots \mathbf{r}_N) = -\Psi(\mathbf{r}_1, \ldots, \mathbf{r}_a, \ldots, \mathbf{r}_b, \ldots \mathbf{r}_N) \qquad \text{(Equation 2.6)}$$

The antisymmetrization always results in wave functions that are no longer a simple product, but a sum of products. This complexity is resolved by constructing a determinant of the electron wave-functions [94]. The determinant is a linear combination of all possible Hartree wave-functions obtainable from permutations of r_i added together with weights ± 1, so as to give the condition in Equation 2.6. The Hartree-Fock equation (Equation 2.7), is obtained when all necessary simplifications are done.

$$\left[-\frac{\hbar^2}{2m_i}\nabla_i^2 - \frac{Ze^2}{r_i} + e^2 \sum_{j \neq i} \int d^3 r_j \frac{\mid \psi_j(\vec{r_j}) \mid^2}{\vec{r_i} - \vec{r_j}} - \frac{1}{2}\left[\sum_j \int \frac{\psi_j^*(r_j)\psi_i(r_j)}{\mid r_i - r_j \mid} dr_j\right] \frac{\psi_j(r_i}{\psi_i(r_i}\right] \psi_i \vec{r_i} = \epsilon_i \psi_i \vec{r_i} \qquad \text{(Equation 2.7)}$$

The last term on the left hand side of Equation 2.7 describes the exchange interaction which is applied between parallel-spin electrons. This term ensures that Equation 2.7 obeys the Pauli exclusion principle.

Due to an average non-local potential arising from the other electrons, the Hartree-Fock equation is only a first order approximation to the total energy. By also assuming a single-determinant form for the wave-functions, the HF approximation neglects correlation between electrons, which can lead to a poor description of the electronic structure [95]

2.2 Density Functional Theory (DFT)

Today's electronic structure calculations make use of the Density Functional Theory. DFT uses the electron density as a basic variable to describe a system with many particles. The idea of using the electron density as a single entity to describe a system actually started from the Thomas-Fermi (TF) theory [96, 97]. The TF density functional scheme treat electrons as independent particles, with the electron-electron interaction energy arising solely from the electrostatic energy. This scheme had limited success in describing real systems, but it is considered the prototype for all modern density functional theories. The DFT used presently by the material physics research community was formulated by Hohenberg and Kohn (known as HK-DFT) [98] and Kohn and Sham (KS-DFT) [1].

The Hohenberg-Kohn DFT states that the total energy of a many-body system is a unique functional of electron density. The total energy functional can be written as:

$$E[n] = F[n] + \int n(r)V_{ext}(r)dr \qquad \text{(Equation 2.8)}$$

where F is a universal functional of n and the minimum value of the functional E is E_0, the exact ground-state electronic energy.

The universal functional $F[n]$ is unknown, but independent of the external potential.

2.2.1 The Kohn-Sham (KS) Equations

The Hartree-Fock equation is capable of producing good results (not in metals), but is too time consuming to solve. Other DFT formulations (i.e. Thomas-Fermi equation) is quicker to solve, but produces inaccurate results. A crossbreed between these equations is the Kohn-Sham equation. This equation was introduced by Kohn and Sham [1] and it has capacity for large numerical calculations in solids. The Schrödinger equation requires that kinetic energy of electrons be high at any region where the electron density is high, and also where the gradient of their wave functions are large. The defect in the Thomas-Fermi equation comes from the approximated kinetic energy because the equation only recognizes high kinetic energy in a region of high electron density, but fails to take into account the requirement for high kinetic energy where the gradient of the wave functions is large.

To obtain an electron problem that can be solved, the Kohn-Sham formalism [1], separated the universal functional $F[n]$, in the Hohenberg-Kohn equation into three distinct parts such that:

$$F[n] = T_s[n] + \int \frac{n(r)n(r^{'})}{r - r^{'}} dr dr^{'} + \mu_{xc}(n) \qquad \text{(Equation 2.9)}$$

where $T_s[n]$ is a non-interacting kinetic energy given as:

$$T_s[n] = \frac{\hbar^2}{2m} \sum_i \int \psi_i^*(\mathbf{r}) \nabla^2 \psi_i(\mathbf{r}) d\mathbf{r} \qquad \text{(Equation 2.10)}$$

The last functional, $\mu_{xc}(n)$ is unknown and it is usually approximated.

2.2.2 Approximations for μ_{xc}

In electronic structure calculations, μ_{xc} is most commonly approximated. The local density approximation (LDA) is a well tested, most widely used and very successful approximation within KS-DFT. LDA uses a functional that depends only locally on the density for μ_{xc}. The assumption is that the exchange-correlation energy per electron in the electron gas and at point r, $\epsilon_{xc}(\mathbf{r})$ is equal to the exchange-correlation energy per electron in a homogeneous electron gas that has the same electron density at r, ie.:

$$\mu_{xc}^{LDA}[n(\mathbf{r})] = \int n(\mathbf{r}) \epsilon_{xc}[n(\mathbf{r})] d\mathbf{r} \qquad \text{(Equation 2.11)}$$

so that:

$$v_{xc}(\mathbf{r}) = \frac{\delta[n(\mathbf{r}) \epsilon_{xc} n(\mathbf{r})]}{\delta n(\mathbf{r})} \qquad \text{(Equation 2.12)}$$

with:

$$\epsilon_{xc}(n(\mathbf{r})) = \epsilon_{xc}^{hom}(n(\mathbf{r})) \qquad \text{(Equation 2.13)}$$

However, in practical calculations there is still the need to know the actual numerical value of ϵ_{xc} for all densities. As there is no exact analytical form for this, calculations based on many body perturbation theory [2] and the quantum Monte Carlo method [3] have been used to parameterize numerical formulas for ϵ_{xc} that are accurate for a wide range of values of $n(\mathbf{r})$. Popular parameterizations include those of Hedin and Lundquist [2], Von Barth and Hedin [99], Janak [100] Perdew and Zunger [4], Vosoko, Wilk and Nusair [101] and Perdew and Wang [102]. However, since the fitting parameters used in constructing DFT-LDA are distinct from those used in other theories, the accuracy to the exchange-correlation potential in real system calculations can only be validated by an agreement between calculated results and experimental data.

Another approximation for μ_{xc} is the generalized gradient approximation (GGA) [1]. The GGA is an approach that improves the LDA by including gradient corrections. This is achieved by adding an enhancement factor $F_{xc}[n(\mathbf{r}), \nabla n(\mathbf{r})]$, which directly modifies the LDA energy density as:

$$\mu_{xc}^{GGA}[n(\mathbf{r})] = \int n(\mathbf{r})\epsilon_{xc}[n(\mathbf{r})]drF_{xc}[n(\mathbf{r}), \nabla n(\mathbf{r})]d\mathbf{r} \qquad \text{(Equation 2.14)}$$

where F_{xc} is a correction chosen to satisfy many constraints for μ_{xc}. However, since it is not possible to satisfy every constraint simultaneously, F_{xc} is often chosen according to the nature of the system under study. PW91 [103] used to be a famous GGA functional within solid state DFT community. The PW91 exchange enhancement factor has the form:

$$F_{xc}^{PW91}(s) = \frac{1 + 0.19645s\sinh^{-1}(7.7956s) + (0.2743 - 0.15084e^{-100s^2})s^2}{1 + 0.19645s\ \sinh^{-1}(7.7956s) + 0.004s^4} \qquad \text{(Equation 2.15)}$$

where the reduced density gradient s is a dimensionless quantity written as a function of Seitz radius r_s, ie.:

$$r_s = \left(\frac{3}{4\pi n}\right)^{1/3} \qquad \text{(Equation 2.16)}$$

$$s(\mathbf{r}) = \frac{|\nabla n(\mathbf{r})|}{2k_F(\mathbf{r})n(\mathbf{r})} = \frac{3}{(18\pi)^{1/3}}|\nabla r_s| \qquad \text{(Equation 2.17)}$$

Equation 2.15 is an improvement over the expression formerly given by Becke, known as B88 [104]. It is tailored to obey some extra exact conditions such as scaling relations [105] and

correct behavior in a slowly varying limits of energy bounds [106]. Until recently, PW91 was the sole GGA in use. It has now been superseded by the GGA formulated by Perdew, Burke and Ernzerhof, known as PBE [107, 108]. The PBE approximation uses a much simplified exchange enhancement factor. Despite its simplicity, most important conditions satisfied by PW91 are also satisfied by PBE. For $0 < s < 3$, i.e. the range exhibited by most physical systems, the PBE and PW91 enhancement factors are virtually indistinguishable and yield the same physical properties. While the GGA corrects the over-binding tendency of the LDA, it unfortunately has the tendency to over-correct for heavy elements.

2.3 Kohn-Sham equation in plane waves

In the previous sections, the difficulty of the many body problems and how these can be circumvented through density functional theory was discussed. The Kohn - Sham (KS) equation, which is a single particle Schrödinger equation and the LDA and GGA being two approximations to the exchange-correlation term of the KS equation had also been discussed. In this section, the implementation of Kohn-Sham DFT using planewave pseudo-potentials will be discussed. This is a well established method [109], which although computationally demanding, is accurate in describing infinite periodic systems such as solids. **??** is reproduced in Figure 2.1, illustrating the various methods for its implementation.

The first step in solving problems with plane-waves is the construction of a basis set to

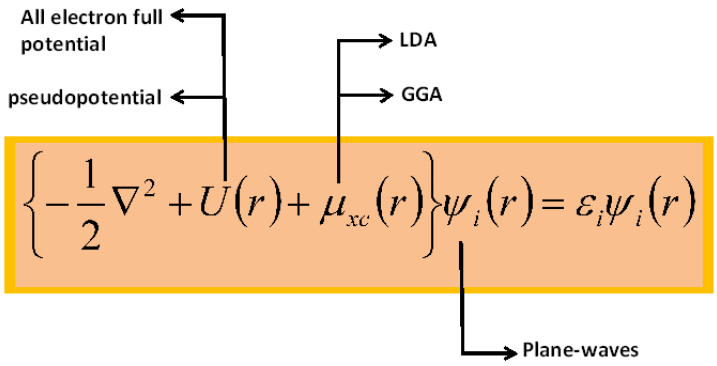

Figure 2.1: KS-DFT equation and its methods of implementation

represent the wave functions.

$$\psi(\mathbf{r}) = \sum C_i \phi_i(\mathbf{r}) \qquad \text{(Equation 2.18)}$$

where $\phi_i(\mathbf{r})$ are the basis functions and C_i are the expansion coefficients.

In a periodic potential, the Bloch theorem [110], can be used to write the wave-function ψ as a product of a periodic lattice part $u_j(\mathbf{r})$ and a wavelike part $\mathrm{e}^{i\mathbf{k}\cdot\mathbf{r}}$:

$$\psi_{j,\mathbf{k}}(\mathbf{r}) = u_j(\mathbf{r})\,\mathrm{e}^{i\mathbf{k}\cdot\mathbf{r}} \qquad \text{(Equation 2.19)}$$

Because the periodicity of $u_j(\mathbf{r})$ is same as that of the direct lattice, it can be expressed in

terms of a discrete plane-wave basis set, $\mathbf{G}$, which are wave-vectors of the crystal, i.e.

$$u_j(\mathbf{r}) = \sum_{\mathbf{G}} c_{j,\mathbf{G}}\, \mathrm{e}^{i\mathbf{G}\cdot\mathbf{r}} \qquad \text{(Equation 2.20)}$$

where $\mathbf{G} \cdot \mathbf{R} = 2\pi m$. m is an integer, $\mathbf{R}$ are the crystal lattice vectors and $c_{j,\mathbf{G}}$ are the plane-wave coefficients. Each electronic wave-function can then be written as a sum of plane waves:

$$\psi_{j,\mathbf{k}}(\mathbf{r}) = \sum_{\mathbf{G}} c_{j,\mathbf{k}+\mathbf{G}}\, \mathrm{e}^{i(\mathbf{k}+\mathbf{G})\cdot\mathbf{r}} \qquad \text{(Equation 2.21)}$$

Equation 2.21 is the expression for the reciprocal space vectors within the first Brillouin zone of the periodic cell, $\mathbf{k}$.

2.3.1 k-point sampling

The use of the Bloch theorem to obtain Equation 2.21 leads to an infinite number of reciprocal-space over the first Brillouin zone. These k-points contribute to the electronic potential of the bulk solid. For an accurate result, wave-functions need to be calculated around all the k-points in the Brillouin zone. But because electron wave-functions do not change appreciably over a small distances in k-space, ie. electronic wave-functions at k-points

that are very close together will almost be identical [111], an acceptable result can be obtained by performing the calculation over a finite, but sufficiently dense, mesh of k-points [90]. For this reason, electronic states are only calculated at a set of k-points determined by the shape of the Brillouin zone and the positions of the k-points within the Brillouin zone must be chosen carefully to obtain efficient description of a particular system, while still leading to quite significant computational savings. Different approaches for obtaining these optimal or "special" k-point sets have been discussed [112, 113, 114].

All the calculations performed in this work employ the Monkhorst-Pack (MP) method [115]. In MP method, the k-points are distributed homogeneously throughout space in columns, following the shape of the Brillouin zone, ie.

$$\mathbf{k}_j = x_{1j}\mathbf{b}_1 + x_{2j}\mathbf{b}_2 + x_{3j}\mathbf{b}_3 \qquad \text{(Equation 2.22)}$$

where $\mathbf{b}_1, \mathbf{b}_2, \mathbf{b}_3$ are the reciprocal lattice vectors, and,

$$x_{ij} = \frac{l_i}{n_j}, \quad j = 1, \ldots, n_j \qquad \text{(Equation 2.23)}$$

where l_i are the lengths of the reciprocal lattice vectors and n_j characterizes the number of special points in the set.

For less computation expense, the full special k-point set is obtained using the point-group symmetry T of the crystal:

$$n(\mathbf{k_j})_T = \frac{1}{N_T} \sum_{T_p \in T} n(\mathbf{T_p k_j}) \qquad \text{(Equation 2.24)}$$

where N_T is the number of operations, T_p in the point group T.

The full reciprocal space charge density is then obtained as:

$$n(\mathbf{k}) = \sum_i w_j n(\mathbf{k_j})_T \qquad \text{(Equation 2.25)}$$

By Fourier transformation, the full real space charge density $n(\mathbf{r})$ for a crystal with point group operations, T, is obtained as:

$$n(\mathbf{r}) = \frac{v}{(2\pi)^3} \int_{BZ} n_k(\mathbf{r}) dk \qquad \text{(Equation 2.26)}$$

where v is the unit cell volume.

The values of the weighting factors, w_j, are adjusted according to this new k-point set and

the integrals Equation 2.26 are calculated with this set. Using a point group operations, T, the charge density obtained is associated with other points throughout the zone. This is achieved by evaluating **??** with the k-point sampling approximation such that:

$$n(\mathbf{k_j}) = \sum_i \psi^*(\mathbf{k_j})\psi(\mathbf{k_j}) \qquad \text{(Equation 2.27)}$$

2.4 Pseudo-potentials

Electrons in matter are broadly categorized into those close to the nucleus (core electrons) and those far from the nucleus (valence electrons). Because the core electrons are strongly localized in the closed inner atomic shells [111], DFT wave functions have very sharp features for core electrons, resulting in much oscillation in the core states due to the orthogonality requirement. To correctly describe events at the core regions, a very large set of plane waves, or very fine grid would be required. This would be expensive and computationally demanding. This problem is circumvented by describing the collective system of nuclei and core electrons with pseudopotentials. In the pseudopotential approach, the Kohn-Sham equations are solved for the valence electrons only, while the remaining scattering potential are described by pseudopotentials at a certain radius from the core. This method reduces the number of wave functions to be calculated, so that only calculations on the valence states are needed. The drawbacks of treating core electron states with pseudopotential is that information on the

full wave function close to the nuclei is lost, which can influence the calculation of certain properties, such as electric field gradients [116]. Also, there is no before hand knowledge of when the approximation yields reliable results.

In different chemical environments, the pseudopotential concept assumes that the electronic structure of core-electrons remains unchanged. This approximation [117, 118], is used to eliminate the need to treat atomic core states and the various nuclear potential responsible for binding them. Illustration of the pseudo-potential concept is shown in Fig. 2.1 [119]. The pseudo-potential is constructed such that there are no radial nodes and that pseudo-wavefunction and the pseudo-potential are identical to the all-electron wave-function and the potential outside the cut off radius r_c. Since the scattering properties of the ion core are angular momentum dependent, the pseudo-potential is constructed so that its scattering properties or phase shifts for pseudo-wave-functions are identical to the scattering properties of the ion and core electrons for the valence wave functions [120].

2.4.1 First-Principles Pseudo-potential Generation

To generate pseudo-potentials usable in DFT calculations, the radial Schrödinger equation (Equation 2.28) must be solved self-consistently.

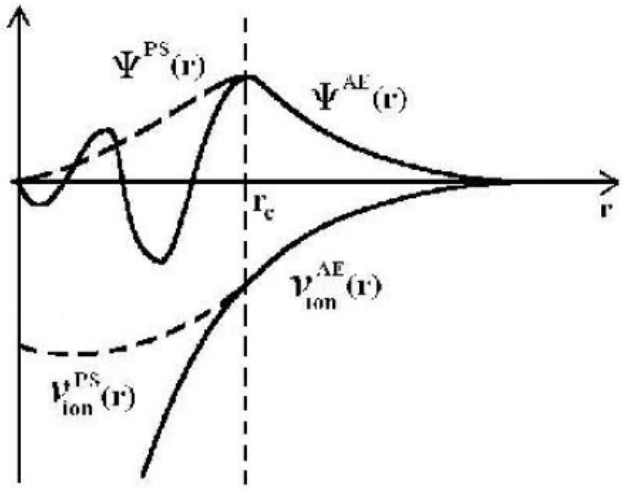

Figure 2.2: Schematic illustration of the pseudo-potential concept. The solid lines show the all-electron wave-function, $\Psi^{\mathrm{AE}}(\mathbf{r})$, and ionic potential, $v_{\mathrm{ion}}^{\mathrm{AE}}(\mathbf{r})$, while the dashed lines show the corresponding pseudo-wave-function, $\Psi^{\mathrm{PS}}(\mathbf{r})$, given by the pseudo-potential, $v_{\mathrm{ion}}^{\mathrm{PS}}(\mathbf{r})$. All quantities are shown as a function of distance, $\mathbf{r}$, from the atomic nucleus.

The cutoff radius r_c marks the point beyond which the all-electron and pseudo quantities become identical.

$$\left[-\frac{1}{2}\frac{d^2}{dr^2} + \frac{l(l+1)}{2r^2} - \frac{Z}{r} + v_H(\mathbf{r}) + v_{xc}(r) \right] \psi_l^{AE}(r) = \epsilon_l \psi_l^{AE}(r) \qquad \text{(Equation 2.28)}$$

$v_{\mathrm{H}}(r)$ and $v_{\mathrm{XC}}(r)$ are the Hartree and exchange-correlation potentials, and $\psi_{n,l}^{\mathrm{AE}}$ is the all-electron atomic wave-function with angular momentum component l.

A versatile pseudo-potential should meet the following four criteria:

(i) the valence pseudo-wave-function $\psi_l^{\mathrm{PS}}(r)$ must be the same as $\psi_l^{\mathrm{AE}}(r)$ outside a given cutoff radius r_c. (ii) the charge enclosed within r_c must be equal for the two wave-functions,

$$\int_0^{r_c} |\psi_l^{\mathrm{PS}}(r)|^2\, dr = \int_0^{r_c} |\psi_l^{\mathrm{AE}}(r)|^2\, dr \qquad \text{(Equation 2.29)}$$

and is normalized such that, $\int_0^{\infty} |\psi_l^{\mathrm{PS}}(r)|^2\, dr = \int_0^{\infty} |\psi_l^{\mathrm{AE}}(r)|^2\, dr = 1$. This is commonly referred to as norm-conservation.

(iii) $\psi_l^{\mathrm{PS}}(r)$ must not contain any nodes and be continuous at r_c, as well as its first and second derivatives.

(iv) the valence electron and pseudo-potential eigenvalues must be equal.

The essence of the above conditions is to permit freedom when generating pseudo-wave-functions and consequently, when constructing pseudo-potentials. The ionic pseudo-potential is then obtained by inverting Equation 2.28 once the pseudo-wave-function had been created, giving:

$$v_{\mathrm{ion},l}^{\mathrm{PS}}(r) = \epsilon_l - v_H^{PS}(r) - \frac{l(l+1)}{2r^2} + \frac{1}{2\psi_l^{\mathrm{PS}}(r)} \frac{d^2}{dr^2} \psi_l^{\mathrm{PS}}(r) \qquad \text{(Equation 2.30)}$$

where $v_{\mathrm{H}}^{\mathrm{PS}}(r)$ and $v_{\mathrm{XC}}^{\mathrm{PS}}(r)$ are calculated from the pseudo-wave-functions. However, the consequence of this procedure is that a separate pseudo-potential must be generated for each angular momentum component l.

Pseudo-potentials of this type are referred to as *non-local-norm-conserving* pseudo-potentials, and are capable of describing core ion scattering in a variety of environments. Non-local-norm-conserving pseudo-potential are transferable. A pseudo-potential is said to be transferable if it is accurate in a variety of different chemical environments.

2.4.2 Ultra-soft pseudo-potentials

It has been observed that norm-conserving pseudo-potentials give wrong descriptions of first row and transition metal elements [121]. These elements contain highly localized valence orbitals, which makes it difficult to represent the pseudo-wave function in plane wave basis. In these elements, the norm-conserving criteria will force the pseudo-wave function to vary rapidly, meaning that to adequately describe their properties, large basis sets will be required. As this is not practicable, the only compromise is to increase the core radius, which will then adversely affect the transferability and reduce the quality of the pseudo-potential. To cure this problem, other pseudo-potentials, known as "ultra-soft" pseudo-potential [122], developed by Vanderbilt [123] in the early 1990s are in use.

Compared with other pseudo-potentials, ultra-soft pseudo-potentials result in smoother pseudo-wave-functions. Therefore, they use fewer plane-waves for calculations of the same accuracy. Ultra-soft pseudo-potentials yield results that are indistinguishable from those obtainable from the best all-electron methods currently available [124]. The procedure is achieved by relaxing the norm-conservation constraint Equation 2.29, which offers greater flexibility in

the construction of the pseudo-wave-functions. In this scheme the total valence density $n(\mathbf{r})$ is partitioned into so-called hard and soft contributions:

$$n(\mathbf{r}) = \sum_n \left[|\phi_n(\mathbf{r})|^2 + \sum_j \rangle\langle \beta_i | \phi_n \rangle \right] \qquad \text{(Equation 2.31)}$$

where β_i are projector functions that depend on the ionic positions, and the augmentation function $Q_{ij}(\mathbf{r})$ is given by

$$Q_{ij}(\mathbf{r}) = \psi_i^*(\mathbf{r})\psi_j(\mathbf{r}) - \phi_i^*(\mathbf{r})\phi_j(\mathbf{r}) \qquad \text{(Equation 2.32)}$$

where $\psi_i(\mathbf{r})$ are the all-electron wave-functions. The norm-conservation condition ($Q_{ij}(\mathbf{r}) = 0$) is not satisfied in the construction of the ultra-soft wave-functions, $\phi_i(\mathbf{r})$.

Also, the orthonormal condition takes on a generalized form:

$$\langle \phi_i | S(\{\mathbf{R}_I\}) | \phi_j \rangle = \epsilon_{ij} \qquad \text{(Equation 2.33)}$$

where $S(\mathbf{R}_I)$ depends on the ionic positions through $|\beta_i\rangle$ and is defined as:

$$S = 1 + \sum_{ij} q_{ij} |\beta_j\rangle\langle\beta_i| \qquad \text{(Equation 2.34)}$$

with

$$q_{ij} = \int Q_{ij}(\mathbf{r})\, d\mathbf{r} \qquad \text{(Equation 2.35)}$$

When using ultra-soft pseudo-potentials, the cutoff energy E_{cut} is typically about half that of conventional norm-conserving pseudo-potentials [124]. For simple estimates, the number of plane-waves scales as $E_{\text{cut}}^{\frac{3}{2}}$, meaning that the number of plane waves required in a given calculation is one-third less.

2.5 Projector Augmented-Wave Method

The projector augmented wave (PAW) method was introduced by Blöchl in 1994 [125]. This method has the physics of all-electron formalisms with the numerical advantages of pseudo-potential techniques. The method has been successfully used for density functional studies due to its formal simplicity. As earlier pointed out, the features of the wave functions, are very different for both the valence and core regions. At the valence region, it is smooth, but near the nuclei it displays rapid oscillations, which places a highly demanding numerical

representation on the wave functions. The Blöchl formalism addressed this problem by providing a transformation between an auxiliary smooth wave function to the true all electron Kohn-Sham single particle wave function according to Equation 2.36.

$$| \psi_n\rangle = \hat{T} \, |\widetilde{\psi}_n\rangle \qquad \text{(Equation 2.36)}$$

where n is the quantum state label, containing a band index, a k index and a spin index.

By this transformation, the transformed KS equations is:

$$\hat{T^\dagger}\hat{H}\hat{T} \, |\widetilde{\psi}_n\rangle = \epsilon_n \hat{T^\dagger}\hat{T} \, |\widetilde{\psi}_n\rangle \qquad \text{(Equation 2.37)}$$

which needs to be solved instead of the usual KS equation. Since the wave functions are already smooth at certain minimum distance from the core, $\hat{T}$ is modified in Equation 2.37 to obtain a smooth auxiliary wave functions close to the nuclei. In a suitable way, $\hat{T}$ can be defined as:

$$\hat{T} = 1 + \sum_a \hat{T}^a \qquad \text{(Equation 2.38)}$$

where a is an atom index and $\hat{T}^a$ is the atom-centered transformation, which has no effect outside certain atom-specific augmentation region defined as:

$$| r - R^a | < r_c^a \qquad \text{(Equation 2.39)}$$

where the cutoff radius r_c^a is chosen to ensure that there is no overlap of the augmentation spheres.

Inside the augmentation spheres, the true wave function is expanded in terms of a partial waves ϕ_i^a, and for each partial waves, a corresponding auxiliary smooth partial wave $\widetilde{\phi}_i^a$ is defined such that:

$$| \phi_i^a\rangle = (1 + \hat{T}^a) \, |\widetilde{\phi}_i^a\rangle \Leftrightarrow \hat{T}^a \, |\widetilde{\phi}_i^a| \phi_i^a\rangle - |\widetilde{\phi}_i^a\rangle \qquad \text{(Equation 2.40)}$$

Given ϕ and $\widetilde{\phi}$ respectively, Equation 2.40 completely defines T^a for all i and a.

However, since T^a is required to do nothing outside the augmentation sphere, both the partial wave and its smooth counterpart need to be identical outside the augmentation sphere. In Equation 2.40, this can be obtained by setting:

$$\phi_i^a(r) = \widetilde{\phi_i^a}\,(r) \qquad \text{(Equation 2.41)}$$

for $r > r_c^a$. Where $\phi_i^a(r) = \langle r \mid \phi_i^a(r) \rangle$ and likewise for $\widetilde{\phi_i^a}$.

Inside the augmentation sphere, the complete set of all electron wave functions can thus be expanded in terms of the smooth particle waves as:

$$|\widetilde{\psi_n}\rangle = \sum_i P_{ni}^a \, |\widetilde{\phi_i^a}\rangle, \qquad \text{(Equation 2.42)}$$

for $\mid r - R^a \mid < r_c^a$.

where P_{ni}^a is an expansion coefficient.

Since $\mid \phi_i^a \rangle = \hat{T} \, |\widetilde{\phi_i}^a$ then the expansion;

$$\mid \psi_n \rangle = \hat{T} \, |\widetilde{\phi_n}\rangle = \sum_i P_{ni}^a \, |\widetilde{\phi_i^a}\rangle \qquad \text{(Equation 2.43)}$$

for $\mid r - R^a \mid < r_c^a$, has the same expansion coefficients, P_{ni}^a.

As $\hat{T}$ is required to be linear, P^a_{ni} is also a linear functional of $|\widetilde{\psi}_n\rangle$, i.e.

$$P^a_{ni} = \langle \widetilde{p}^a_i | p\widetilde{si}_n \rangle = \hat{T} \, |\widetilde{\phi}_n\rangle = \int dr \, \widetilde{p}^{a*}_i \, (r - R^a) \, \widetilde{\psi}_n \, (r) \qquad \text{(Equation 2.44)}$$

where $|\widetilde{p}^a_i\rangle$ are some fixed functions known as smooth projector functions.

To ensure no overlap between the projector functions, a one center all electron wave function, defined as:

$$\mid \psi^a_n \rangle = \sum_i \mid \phi_i \rangle \langle \widetilde{p}^a_i \mid \psi_n \rangle \qquad \text{(Equation 2.45)}$$

must reduce itself to $|\widetilde{\psi}_n\rangle$ inside the augmentation sphere defined by a. This is satisfied by:

$$\sum_i |\widetilde{\phi}^a_i \, \rangle \langle \widetilde{p}^a_i \, | = 1 \qquad \text{(Equation 2.46)}$$

which also implied that:

$$\langle \widetilde{p}^a_i \, | \widetilde{\phi}^a_i \, \rangle = \delta_{i_1, i_2} \qquad \text{(Equation 2.47)}$$

For $r > r_c^a$ (i.e. outside the augmentation spheres), there are no restrictions on $\widetilde{p_i}^a$. For convenience therefore, $\widetilde{p_i}^a$ is treated as local functions, i.e. $\widetilde{p_i}^a\ (r) = 0$.

To ensure that $\widetilde{p_i}^a$ produces correct expansion coefficients of the form in Equation 2.42 and Equation 2.43, it was restricted with the completeness relation in Equation 2.46, while Equation 2.47 is an implication of this restriction.

The translation of Equation 2.46 to the projector functions is a difficult procedure. According to Blöchl [125], the general form of the projector functions can be written as:

$$\langle \widetilde{p_i}^a | = \sum_j \left(\left\{ \langle f_k^a \, | \widetilde{\phi_l}^a \rangle \right\} \right)^{-1}_{ij} \langle f_j^a \, | \qquad \text{(Equation 2.48)}$$

where $| f_j^a \rangle$ is any set of linearly independent functions.

Using the relation in Equation 2.46, the atom-centered transformation, $\hat{T}^a$ becomes:

$$\hat{T}^a = \sum_j \hat{T}^a \, | \widetilde{\phi_l}^a \rangle \langle \widetilde{p_i}^a | \qquad \text{(Equation 2.49)}$$

The first equality in Equation 2.49 is true in all space. The second equality is due to Equation 2.46 where outside the augmentation sphere, $| \phi_l^a \rangle - | \widetilde{\phi_l}^a \rangle = 0$.

Using these transformations, the all electron Kohn-Sham wave function $\psi_n(r) = \langle r \mid \psi_n \rangle$ can then be written as:

$$\psi_n(r) = \widetilde{\psi}_n\ (r) + \sum_a \sum_i \left(\phi_i^a(r) - \widetilde{\phi}_i^{\,a}\ (r) \right) \langle \widetilde{p}_i^{\,a} | \widetilde{\psi}_n \rangle \qquad \text{(Equation 2.50)}$$

The smooth (auxiliary) wave function $\widetilde{\psi}_n\ (r)$ is now numerically convenient to obtain by solving the eigenvalue Equation 2.37.

The transformation in Equation 2.50 have separated the original wave functions into a contribution that contains rapid oscillations in certain, small, areas of space and auxiliary wave functions that are smooth everywhere. The major advantage of PAW and this transfomation formalism is that the sets of functions needed to define the transformation are system independent, and as such, they can conveniently be pre-calculated and tabulated for each element of the periodic table [116].

2.5.1 Ultra-soft vs PAW Potentials

Both ultra-soft pseudo-potential and PAW potentials have similarities as pointed out by Blöchl and derived by Kresse and Joubert [126]. Although, the PAW potential is based on a different philosophy and was generated about 5 years after the ultra-soft potentials (US-PP), yet, the construction scheme for both pseudo-potential are the same. Generally, the PAW

potentials, uses less parameters and are more accurate for; magnetic materials, alkali and alkali earth elements, early 3d elements, lathanides and actinides [126, 127]. US-PP becomes progressively softer down the periodic table [127] while the performance of PAW potentials are similar across the periodic table.

PAW potentials are more superior for treating compounds having species with very different covalent radii. The US-PP is faster for a one component system, but at reduced precision [126, 127]. Both US-PP and PAW works well with LDA and GGA.

2.6 Energy Minimization

In order to determine the physical properties of a system, the total energy of the system has to be calculated. To do this, the electronic states that minimizes the Kohn-Sham total energy needs to be determined. There are two methods that are usually used for this: *steepest descent* method and *conjugate gradient* method.

2.6.1 Steepest Descent Method

The steepest descent minimization technique attempts to locate the minimum total energy along the steepest descent path. It calculates the direction from the minimal until the ground-state is located. The path of calculation is chosen using information from the present

sampling point only, while information regarding previous search directions are ignored[128]. This method requires a large number of iterations and the results of its convergence may not be reliable.

2.6.2 Conjugate Gradient Method

Compared with the steepest descent method, the conjugate gradient technique is a more expedient minimization technique. This method combines information from all search directions to create a new search direction that is independent (conjugate) to all previous directions. The new search directions are linearly independent. To minimize storage, it is only the previous search direction that is saved, rather than all other previous directions [120]. After each iteration, the dimensionality of a problem is reduced by 1. It is computationally cheaper and faster as any n-dimensional vector-space is determined in n iterations [129].

2.6.3 Preconditioning

The number of plane-wave coefficients required to implement conjugate gradient minimization technique is typically of the order of $\sim 10^5$, meaning that a long time is required to minimize a band. The efficiency of the method also reduces as the kinetic energy cutoff increases. A preconditioning scheme [130] is usually applied with the conjugate gradient method to overcome these problems. Preconditioning is achieved by separating the high kinetic energy

plane waves and the low kinetic energy plane waves. In most cases, high kinetic energy plane-waves dominate search directions, and are therefore sought, leaving the low kinetic energy waves untouched. With this done, the range of Eigenvalue energies are compressed, leading to faster convergence. The calculations performed in this work use preconditioned conjugate gradient minimization scheme.

2.6.4 The Vienna *ab initio* Simulation Package (VASP)

All *ab initio* calculations and results reported in this thesis were done with the VASP computer code [131, 132]. VASP is a package for performing quantum mechanical calculations on molecules and solids. It uses an iterative variational method to solve the Kohn-Sham equation of a system [109]. This approach is preferred over the direct diagonalization method, because the latter is inefficient for large systems. The Car-Parrinello (CP) [133] and the conjugate-gradient [120] energy minimization methods are both implemented in the VASP code. Both the local density approximation (LDA) and the generalized gradient approximation (GGA) are currently the most used functionals for treating μ_{xc} in VASP. Other high hierarchy functionals such as the meta-GGA or hyper-GGA functionals do not presently lead to any systematic improvement over the GGA [134, 135].

In practice, VASP uses a plane-wave (PW) basis-set to iteratively solve the Kohn-Sham equation. An appropriate set of basis functions are chosen to expand the orbitals. The plane-wave basis-sets are chosen and adopted in such a way that:

(i) Basis-set convergence is adequately controlled, which is crucial for the accuracy of a calculation.

(ii) It is easy to calculate the force and stresses on atoms using the Hellmann-Feynman theory [136].

(iii) The effect of strongly bound core-electrons are treated using pseudo-potentials.

The Projector Augmented Wave (PAW) [125] method is implemented in VASP. While avoiding nonlinear core-corrections, the PAW method makes all-electron density calculations feasible for d- and f-electron systems. This not only allow reduced computational effort, but also increases accuracy. VASP-PAW is very accurate when compared with other all-electron calculations, such as the full-potential linearized augmented plane-wave (FLAPW) method [109].

Apart from being able to solve the Kohn-Sham equations of a material, additional functionalities of the VASP code include a set of routines for calculating wide range of materials properties such as atomic, electronic and magnetic structures, spectra (electronic, optical, vibrational, ...), mechanical properties such as elastic constants, heats of formation, anisotropy energies, activation energy for phase transitions etc.

Chapter 3

Ab Initio Equilibrium Properties

For strong materials, mechanical properties are the main concern. After obtaining the ground total energy for a given chemical composition and lattice structure, mechanical properties such as ideal strength, elastic constants can be evaluated. The purpose of electronic structure methods is to be able to predict the ground state equilibrium volumes, elastic and thermodynamic properties of materials. Various techniques used to evaluate the equilibrium volumes, elastic constants, bulk moduli and cohesive properties are discussed in this chapter.

3.1 Thermodynamic Stability and Cohesive Energies

Theoretically, if a substance is thermodynamically stable relative to some other phases, it should be possible to make it by some conventional means. For *ab initio* studies, the enthalpy of formation is traditionally used as the key parameter in the study of thermodynamic

stability [137, 138]. In the case of a binary compound of the form X_mAl_n, where m and n are integers, the formation energy ($\triangle E^{\phi}$) is the energy of X_mAl_n relative to pure X and Al atoms in their equilibrium crystal structures [139]:

$$\triangle E^{\phi}(X_mAl_n) = \frac{1}{m+n}E^{\phi}_{X_mAl_n} - \left[\frac{m}{m+n}E^{\Phi}_{X} + \frac{n}{m+n}E^{\psi}_{Al}\right] \qquad \text{(Equation 3.1)}$$

where $E^{\phi}_{X_mAl_n}$ is the total energy of X_mAl_n with ϕ structure , E^{Φ}_{X} is the total energy per atom of X with Φ structure and E^{ψ}_{Al} is the total energy per atom of Al with ψ structure.

A negative heat of formation is an indication of a thermodynamically stable system [140], while a positive value is an indication of an unstable or metastable system.

The cohesive energy for any material can be defined as the difference between the total energy of the bulk material and energy of the free atoms. The expression for a binary system is given in Equation 3.2.

$$E^{coh} = E_T - \sum_{a}^{N} E_a \qquad \text{(Equation 3.2)}$$

where E_T is the total energy of the compound. E_a is the energy for each atom (or ion) belonging to the crystal unit cell and N is the number of atoms in the unit cell.

The cohesive energy E^{coh}, correlates to the binding strength and therefore to the hardness of a compound. In some materials however (e.g. transition metal carbides and nitrides), cohesive energy alone does not provide reliable indication of the binding strength. Additional information such as the elastic moduli, melting temperature etc in the condensed matter phases are required to adequately describe hardness/bonding strength in such materials.

3.2 Compressibility

A fundamental property of a strong material is its compressibility. In materials science the important properties are often termed"mechanical properties" rather than physical properties. Examples of mechanical properties include *hardness* and *ductility*. Popular equation of state that relates with compressibility are those by Murnaghan [141], Vinet [142] and Birch [143, 144]. Such an equation shows how volume varies with pressure. A desirable and common feature between equation of states is that it contain few parameters and it is able to predict correctly high pressure behaviors irrespective of the material being studied. Birch-Murnaghan EoS [143] is mostly used to obtain the bulk modulus of materials at ground state because it is often used to fit experimental data. The third-order Birch-Murnaghan isothermal equation of state is given by:

$$P(V) = \frac{3B_0}{2}\left\{\left[\frac{V_0}{V}^{\frac{7}{3}} - \frac{V_0}{V}^{\frac{5}{3}}\left\{1 + \frac{3}{4}(B_0^{'} - 4)\left[\frac{V_0}{V}^{\frac{2}{3}} - 1\right]\right\}\right\}\right. \qquad \text{(Equation 3.3)}$$

The energy E(V), is found by integrating Equation 3.3 and;

$$E(V) = E_0 + \frac{9V_0B_0}{16}\left\{\left[\frac{V_0}{V} - 1\right]^3 B_0^{'} + \left[\frac{V_0}{V} - 1\right]^2 \left[6 - 4(\frac{V_0}{V}^{\frac{2}{3}}\right]\right\} \qquad \text{(Equation 3.4)}$$

where V_0 is the isothermal volume, B_0 is the isothermal bulk modulus, $B_0^{'}$ is the pressure derivative of B_0 and E_0 is the energy of the material at V_0.

The bulk modulus of a crystal is defined as:

$$B_0 = -V_0\frac{dP}{dV} \qquad \text{(Equation 3.5)}$$

The bulk modulus is determined by doing a least square fit to Equation 3.3.

3.3 Elastic Constants

Elastic constants are important information that determine the response of a material to applied stress. Atoms are displaced from their equilibrium positions when deformed by interatomic forces. For small deformations, the forces are proportional to the displacement of the atoms. The Hookes law (Equation 3.6) shows that the force F, acting on an atom, is

proportional to the displacement u.

$$F = -ku \qquad \text{(Equation 3.6)}$$

The constant k is an interatomic force constant. In describing elastic properties, crystals are considered to be a homogeneous continuum medium rather than a periodic array of atoms and the problem is generally formulated as follows [145]:

(i) The applied force, is described in terms of the stress σ, and the displacements of atoms are described in terms of strain ε.
(ii) The elastic constants c relates stress σ and ε, so that $\sigma = c\varepsilon$.

Stress is defined in units of force per unit area ($\sigma = F/A$) and can be characterized in the general case by the stress tensor. The strain ε, is a dimensionless constant which describes the relative displacement (deformation). In a 3-dimensional crystal, the stress and the strain are tensors. The stress has components σ_{ij}, showing that the force can be applied along 3 directions i and 3 faces j. The stress is defined locally, so that $\sigma_{ij} = \sigma_{ij}(\mathbf{r})$.

The compression stresses $(\sigma_{xx}, \sigma_{yy}, \sigma_{zz})$, are defined as:

$$\sigma_{xx} = \frac{F_x}{A_x},$$

$$\sigma_{yy} = \frac{F_y}{A_y},$$
$$\sigma_{zz} = \frac{F_z}{A_z} \qquad \text{(Equation 3.7)}$$

and the shear stresses $(\sigma_{xy}, \sigma_{yx}, \sigma_{xz}, \sigma_{zx}, \sigma_{yz}, \sigma_{zy})$, are defined as:

$$\sigma_{xy} = \frac{F_x}{A_y},$$
$$\sigma_{yx} = \frac{F_y}{A_x},$$
$$\sigma_{xz} = \frac{F_x}{A_z},$$
$$\sigma_{zx} = \frac{F_z}{A_x},$$
$$\sigma_{zy} = \frac{F_z}{A_y},$$
$$\sigma_{yz} = \frac{F_y}{A_z} \qquad \text{(Equation 3.8)}$$

To conserve angular acceleration inside a crystal, the shear forces must be in pairs. This condition makes the stress tensor to be diagonal, i.e. $\sigma_{ij} = \sigma_{ji}$.

Atomic displacements are determined relatively by the strain as:

$$\varepsilon_{ij}(\mathbf{r}) = \frac{du_i}{dx_j} \qquad \text{(Equation 3.9)}$$

where u_i is the displacement in i direction and x_j is the direction along which u_i may vary.

For *compression strain* $(\varepsilon_{xx}, \varepsilon_{yy}, \varepsilon_{zz})$,

$$\varepsilon_{xx} = \frac{du_x}{dx},$$
$$\varepsilon_{yy} = \frac{du_y}{dy},$$
$$\varepsilon_{zz} = \frac{du_z}{dz} \qquad \text{(Equation 3.10)}$$

In a homogeneous crystal, $\varepsilon_{xx} = \varepsilon_{yy} = \varepsilon_{zz}$ and it is equal to a constant ($\varepsilon_{xx} = \frac{u}{L}$). u is the change in the crystal length L.

The *shear strain* $(\varepsilon_{xy}, \varepsilon_{yx}, \varepsilon_{xz}\varepsilon_{zx}, \varepsilon_{yz}, \varepsilon_{zy})$ is given as:

$$\varepsilon_{xy} = \frac{du_x}{dy} \qquad \text{(Equation 3.11)}$$

Since $\sigma_{ij} = \sigma_{ji}$ are always applied together, shear strains can also be defined symmetrically as [145]:

$$\varepsilon_{ij} = \varepsilon_{ji} = \frac{1}{2}\left(\frac{du_i}{dx_j} + \frac{du_j}{dx_i}\right) \qquad \text{(Equation 3.12)}$$

In a linear way, the elastic constants c relates the strain and the stress as:

$$\sigma_{ij} = \sum_{k,l=1}^{N} c_{ijkl}\varepsilon_{kl} \qquad \text{(Equation 3.13)}$$

Equation 3.13 is a general form of the Hookes law. The matrix c, would have $3\times3\times3\times3 = 81$ components [145]. Due to the symmetrical nature of σ_{ij} and ε_{ij}, each will have 6 independent components, thereby giving 36 elastic constants [145].

A convention (c_{mn}) is generally used to denote these constants. The indices m and n are defined as 1 = xx, 2 = yy, 3 = zz for the compression components and as 4 = yz, 5 = zx, 6 = xy for the shear components. For example, $c_{11} = c_{xxxx}, c_{12} = c_{xxyy}, c_{44} = c_{yzyz}$. The general form of the Hookes law is therefore given by:

$$\begin{pmatrix} \sigma_{xx} \\ \sigma_{yy} \\ \sigma_{zz} \\ \sigma_{yz} \\ \sigma_{zx} \\ \sigma_{xy} \end{pmatrix} = \begin{pmatrix} c_{11} & c_{12} & c_{13} & c_{14} & c_{15} & c_{16} \\ c_{21} & c_{22} & c_{23} & c_{24} & c_{25} & c_{26} \\ c_{31} & c_{32} & c_{33} & c_{34} & c_{35} & c_{36} \\ c_{41} & c_{42} & c_{43} & c_{44} & c_{45} & c_{46} \\ c_{51} & c_{52} & c_{53} & c_{54} & c_{55} & c_{56} \\ c_{61} & c_{62} & c_{63} & c_{64} & c_{65} & c_{66} \end{pmatrix} \begin{pmatrix} \varepsilon_{xx} \\ \varepsilon_{yy} \\ \varepsilon_{zz} \\ \varepsilon_{yz} \\ \varepsilon_{zx} \\ \varepsilon_{xy} \end{pmatrix} \qquad \text{(Equation 3.14)}$$

All the 36 elastic constants in Equation 3.14 are independent. Due to crystal symmetry however, many of them are the same. For a cubic crystal, the number of elastic constants descring its structure are 3 (c_{11}, c_{12}, c_{44}). The number is 5 for hexagonal and 6 for a tetragonal

Table 3.1: Independent elastic constants describing each crystal system

Crystal Structure	Elastic Constants
Cubic	c_{11}, c_{12}, c_{44}
Hexagonal	$c_{11}, c_{12}, c_{13}, c_{33}, c_{55}$
Tetragonal	$c_{11}, c_{12}, c_{13}, c_{33}, c_{44}, c_{66}$
Trigonal	$c_{11}, c_{12}, c_{13}, c_{14}, c_{33}, c_{44}$
Orthorhombic	$c_{11}, c_{12}, c_{13}, c_{22}, c_{23}, c_{33}, c_{44}, c_{55}, c_{66}$
Monoclinic	$c_{11}, c_{12}, c_{13}, c_{22}, c_{23}, c_{33}, c_{44}, c_{51}, c_{52}, c_{53}, c_{55}, c_{64}, c_{66}$

material. Table 3.1 contains the independent elastic constants needed to describe known crystal systems [145].

Effective isotropic polycrystalline bulk and shear modulus are calculated by two approximations due to Reuss [146] and Voigt [147]. The average between the two approximations (Voigt and Reuss) is referred to as the Hill value, and it gives the actual effective moduli than either of the two approximations [148]. For an isotropic crystallite, the limiting values of the Voigt and Reuss bulk modulus are the same for cubic crystals.

Elements and compounds discussed in the following chapters exists either in the cubic, tetragonal or hexagonal structures. The expressions for obtaining the aggregate bulk and shear moduli for cubic, tetragonal and hexagonal structure are discussed subsequently. Information regarding other structures is provided elsewhere [149, 150, 151].

3.3.1 Cubic Structure

By symmetry, x, y and z are equal in a cubic crystal. Therefore, the elastic constants $c_{11} = c_{22} = c_{33}$; $c_{12} = c_{21} = c_{23} = c_{32} = c_{13} = c_{31}$; $c_{44} = c_{55} = c_{66}$. The off diagonal shear components ($c_{45} = c_{54} = c_{56} = c_{65} = c_{46} = c_{64}$) are zero. Also, mixed compression/shear coupling does not occur, therefore, $c_{14} = c_{41} = 0$. The elasticity matrix in a cubic system is therefore of the form:

$$\begin{pmatrix} \sigma_1 \\ \sigma_2 \\ \sigma_3 \\ \sigma_4 \\ \sigma_5 \\ \sigma_6 \end{pmatrix} = \begin{pmatrix} c_{11} & c_{12} & c_{12} & 0 & 0 & 0 \\ c_{12} & c_{11} & c_{12} & 0 & 0 & 0 \\ c_{12} & c_{12} & c_{11} & 0 & 0 & 0 \\ 0 & 0 & 0 & c_{44} & 0 & 0 \\ 0 & 0 & 0 & 0 & c_{44} & 0 \\ 0 & 0 & 0 & 0 & 0 & c_{44} \end{pmatrix} \begin{pmatrix} \varepsilon_1 \\ \varepsilon_2 \\ \varepsilon_3 \\ \varepsilon_4 \\ \varepsilon_5 \\ \varepsilon_6 \end{pmatrix} \qquad \text{(Equation 3.15)}$$

and the general expression for the aggregate bulk and shear moduli for Voigt and Reuss bounds are of the form:

$$B_V = \frac{(c_{11} + 2c_{12})}{3} \qquad \text{(Equation 3.16)}$$

$$G_V = \frac{(c_{11} - c_{12} - 3c_{44})}{5} \qquad \text{(Equation 3.17)}$$

$$B_R = \frac{(c_{11} + 2c_{12})}{3} \qquad \text{(Equation 3.18)}$$

$$G_R = \frac{5(c_{11} - c_{12})c_{44}}{[4c_{44} + 3(c_{11} - c_{12})]} \qquad \text{(Equation 3.19)}$$

3.3.2 Tetragonal Structure

According to Hooke's law, the matrix notation in tetragonal system is of the form:

$$\begin{pmatrix} \sigma_1 \\ \sigma_2 \\ \sigma_3 \\ \sigma_4 \\ \sigma_5 \\ \sigma_6 \end{pmatrix} = \begin{pmatrix} c_{11} & c_{12} & c_{13} & 0 & 0 & 0 \\ c_{12} & c_{11} & c_{13} & 0 & 0 & 0 \\ c_{13} & c_{13} & c_{33} & 0 & 0 & 0 \\ 0 & 0 & 0 & c_{44} & 0 & 0 \\ 0 & 0 & 0 & 0 & c_{44} & 0 \\ 0 & 0 & 0 & 0 & 0 & c_{66} \end{pmatrix} \begin{pmatrix} \varepsilon_1 \\ \varepsilon_2 \\ \varepsilon_3 \\ \varepsilon_4 \\ \varepsilon_5 \\ \varepsilon_6 \end{pmatrix} \qquad \text{(Equation 3.20)}$$

When expressed in c_{ij}, the Voigt bound for tetragonal systems are:

$$B_V = \frac{1}{9}(2c_{11} + c_{12}) + c_{33} + 4c_{13}) \qquad \text{(Equation 3.21)}$$

$$G_V = \frac{1}{30}(M + 3c_{11} - 3c_{12} + 12c_{44} + 6c_{66}) \qquad \text{(Equation 3.22)}$$

where

$$M = c_{11} + c_{12} + 2c_{33} - 4c_{13} \qquad \text{(Equation 3.23)}$$

and the Reuss bounds are:

$$B_R = \frac{C^2}{M} \qquad \text{(Equation 3.24)}$$

$$G_R = 15\Big[(18B_V/C^2) + (6/(c_{11} - c_{12})) + (6/c_{44}) + (3/c_{66})\Big]^{-1} \qquad \text{(Equation 3.25)}$$

where

$$C^2 = (c_{11} + c_{12})c_{33} - 2c_{13}^2 \qquad \text{(Equation 3.26)}$$

3.3.3 Hexagonal structure

For hexagonal structures, the matrices describing its elastic constant array [145, 149, 152] is of the form:

$$\begin{pmatrix} \sigma_1 \\ \sigma_2 \\ \sigma_3 \\ \sigma_4 \\ \sigma_5 \\ \sigma_6 \end{pmatrix} = \begin{pmatrix} c_{11} & c_{12} & c_{13} & 0 & 0 & 0 \\ c_{12} & c_{11} & c_{13} & 0 & 0 & 0 \\ c_{13} & c_{13} & c_{33} & 0 & 0 & 0 \\ 0 & 0 & 0 & c_{55} & 0 & 0 \\ 0 & 0 & 0 & 0 & c_{55} & 0 \\ 0 & 0 & 0 & 0 & 0 & (c_{11} - c_{12})/2 \end{pmatrix} \begin{pmatrix} \varepsilon_1 \\ \varepsilon_2 \\ \varepsilon_3 \\ \varepsilon_4 \\ \varepsilon_5 \\ \varepsilon_6 \end{pmatrix} \qquad \text{(Equation 3.27)}$$

For Voigt and Reuss bounds, the expressions are:

$$B_V = \frac{1}{9}[2(c_{11} + c_{12}) + c_{33} + 4c_{13}] \qquad \text{(Equation 3.28)}$$

$$G_V = \frac{1}{30}[12c_{66} + 12c_{44}) + c_{11} + c_{12} + 2c_{33} + 4c_{13}] \quad \text{(Equation 3.29)}$$

$$B_R = \frac{(c_{11} + c_{12})c_{33} - 2c_{13}^2}{c_{11} + c_{12} + 2c_{33} - 4c_{13}} \quad \text{(Equation 3.30)}$$

$$G_R = \frac{5}{2}[\frac{c_{44}c_{66}[(c_{11} + c_{12})c_{33} - 2c_{13}^2]}{(c_{44} + c_{66})[(c_{44} + c_{12})c_{33} - 2c_{13}^2] + 3B_V c_{44}c_{66}}] \quad \text{(Equation 3.31)}$$

In all crystal systems, the Hill average values are obtained by:

$$B = \frac{1}{2}(B_V + B_R) \quad \text{(Equation 3.32)}$$

$$G = \frac{1}{2}(G_V + G_R) \quad \text{(Equation 3.33)}$$

And the other two elastic properties; the Young modulus (E) and the Poisson's ratio (v), can be calculated from the following relations:

$$E = \frac{9BG}{3B + G} \quad \text{(Equation 3.34)}$$

$$v = \frac{3B - 2G}{2[3B + G]} \qquad \text{(Equation 3.35)}$$

The Poisson's ratio v, is the ratio of transverse contraction strain to longitudinal extension strain in the direction of stretching force. The strain is elementarily defined as the change in length divided by the original length.

3.4 Mechanical stability from elastic constants

The mechanical stability for a structure can be evaluated from the calculated elastic constants. For cubic crystals [153], the necessary conditions for mechanical stability are given as:

$$(C_{11} - C_{12}) > 0$$

$$(C_{11} + 2C_{12}) > 0$$

$$C_{11} > 0,\ C_{44} > 0$$

Equation 3.36

The stability criteria for a tetragonal crystal are given by Equation 3.36 [153].

$$(C_{11} + C_{33} - 2C_{13}) > 0,\ (C_{11} - C_{12}) > 0$$

$$C_{11} > 0,\ C_{33} > 0,\ C_{44} > 0,\ C_{66} > 0$$

$$(2C_{11} + C_{33} + 2C_{12} + 4C_{13}) > 0$$

Equation 3.37

For orthorhombic structures, the mechanical stability criteria [153, 154] are given by Equation 3.37.

$$(C_{11} + C_{22} - 2C_{12}) > 0,\ C_{11} > 0,\ C_{22} > 0$$

$$(C_{11} + C_{33} - 2C_{13}) > 0,\ C_{33} > 0,\ C_{44} > 0$$

$$(C_{22} + C_{33} - 2C_{23}) > 0,\ C_{55} > 0,\ C_{66} > 0$$

$$(C_{11} + C_{22} + C_{33} + 2C_{12} + 2C_{13} + 2C_{23}) > 0$$

Equation 3.38

For hexagonal structures, only five elastic constants are independent [145]. Therefore, the mechanical stability criterion in this case [155] are as given in Equation 3.38.

$$C_{11} + C_{12} - \frac{2C_{13}^2}{C_{33}} > 0$$

$$C_{66} = \frac{C_{11}+C_{12}}{2} > 0,\ C_{44} > 0$$

Equation 3.39

3.5 Density of States (DOS)

The DOS of a system describes the number of states per interval of energy at each energy level that are available to be occupied by electrons. For a free electron gas, the density of states can be defined as:

$$N(E) = \frac{1}{2\pi^2}\left(\frac{2m}{\hbar^2}\right)^{\frac{3}{2}} E^{\frac{1}{2}} \qquad \text{(Equation 3.40)}$$

This definition is not met in practice where finite atomic interactions are important. Many interesting compounds are generally complex. The calculation of the density of states for these complex systems are in most cases difficult. However, with computer simulations, there are sets of sampling algorithms to evaluate the density of states with high accuracy.

3.5.1 Correlation between DOS and some physical properties

The microscopic electronic structure of an intermetallic compound is influenced by its physical properties. The understanding of the underlying physics that governs properties of an intermetallic compound is a prerequisite in correlating the electronic structure of structural intermetallic compounds with their various physical properties. Due to ionicity, hybridization or covalence [156, 157], different shapes in the DOS curve are created. Electron redistribution

(electro-negativity) that takes place when a compound is formed can lead to a maximum or a minimum (pseudogap) in the vicinity of Fermi level (E_F).

On a DOS plot where the density of states is usually plotted against energy, the structure of an intermetallic compound is considered most stable if E_F (see Figure 3.1(a)) falls exactly on the pseudogap. An unstable structure occurs when E_F falls on a peak (see Figure 3.1(d)) or on the anti-bonding (higher energy side) of the pseudogap (see Figure 3.1(c)) [158, 159, 160]. Maximum stability is ensured when $W_{occ}/W_b \approx 1$ where W_{occ} is the width of the occupied part of DOS and W_b is the width of the region of the bonding states. A compound having its E_F exactly at the pseudogap means the structure has a high melting point [161]. If E_F lies at higher energy than the pseudogap (anti-bonding region), the crystal will exhibit a disordered or amorphous tendency. Since the value of $N(E)$ in this state is high, the structure will try to assume another structure in order to minimize the energy. Phase stability can be achieved by preventing structure transition to another structure type, which can be achieved by adding elements with lower electron concentrations [161].

If on the other hand, E_F lies to the left of the pseudogap (see Figure 3.1(b)), i.e. within the bonding state, it indicates that not all bonding states are filled, necessitating additional electrons to make the system more stable. In summary, stable and ordered compounds tend to have small $N(E_F)$. Apart from being an unstable structure, a compound having its E_F on a peak in the DOS curve shows a more ductile compound [161, 162].

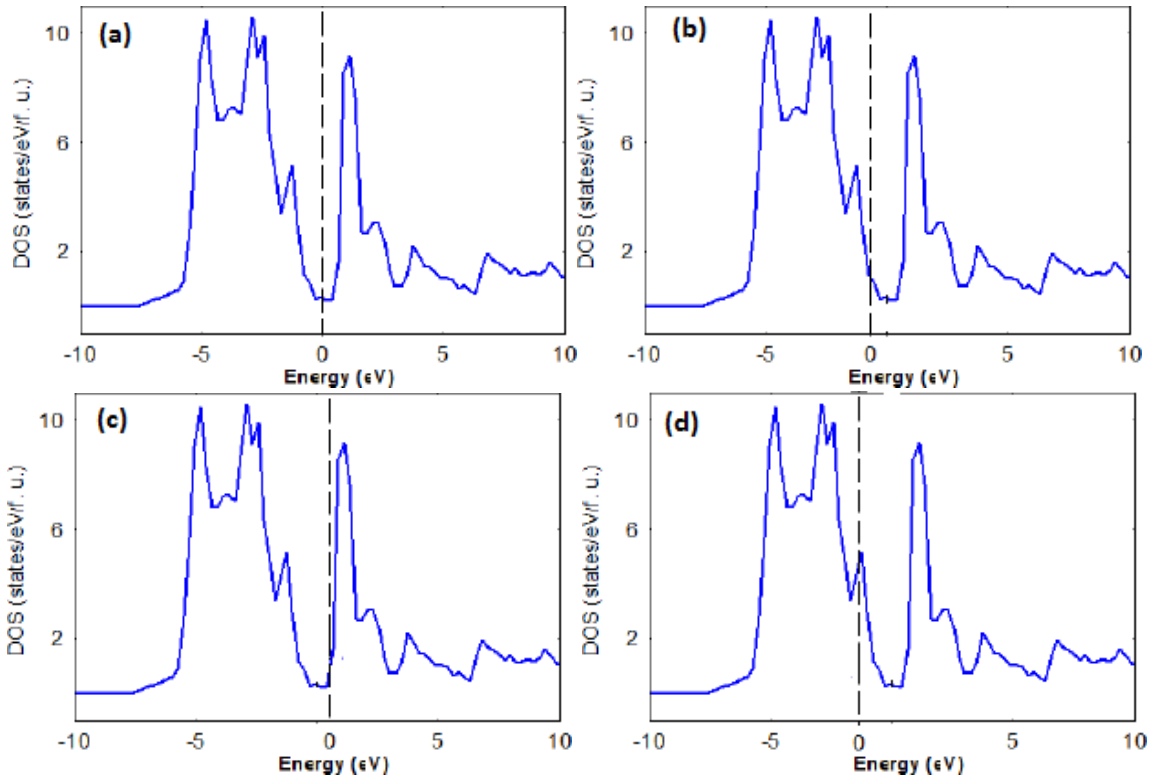

Figure 3.1: Sample DOS plots. (a): stable structure, (b): E_F is on the non-bonding side of pseudogap (a more stable structure can be obtained with addition of elements having high electrons. (c): E_F is on the anti-bonding side of pseudogap (high tendency for metastability). (d) E_F is on a peak (unstable structure).

3.6 Strength of Materials

For any engineering material to be useful at high temperature, it must have an acceptable level of hardness. Hardness is defined as "resistance to plastic deformation" [163], or as "the resistance of a mineral to scratching" [164]. Hardness is a complex property [165] that is dependent on many parameters such as temperature, pressure, porosity, impurities , the nature of the chemical bond etc. Since hardness is not a fundamental property, its value can be influenced by a combination of tensile strength, yield strength and modulus of elasticity [166]. The principle of all hardness test methods is the forcing of an object (known as an

indenter) into the sample surface and the dimensions of the indentation produced are then measured.

Depending on the force of the indenter, hardness test can be either macro, micro or nano-hardness. The macro-hardness tests (such as Rockwell, Brinell or Vickers) are the most widely used methods. In these tests, the indenting force range from 50N to 30000N [166]. For coatings and other related phases, micro-hardness tests (micro-Vickers, Knoop) is the best choice. The indenter is a small diamond pyramid, loaded with a small force of 10 to 1000gf. In the nano-hardness test methods, the indenter is a small load of about 1nN.

Most popular hardness test methods, including; brinell hardness test, rockwell hardness test, vickers hardness test and the knoop hardness test are discussed next.

Brinell Hardness Test

The indenter used in this case is a hardened steel ball. The diameter of the indenter ranges from 2.5 - 10mm. The setup and procedure is depicted in Figure 3.1. For lead alloys, the loading force is 300N, 5000N for aluminum alloys, 10000N for copper alloys and 30000N for steels. The Brinell Hardness (H_B) value is calculated by the formula:

$$H_B = \frac{2F}{3.14D \times (D - (D^2 - D_i^2)^{\frac{1}{2}}} \qquad \text{(Equation 3.41)}$$

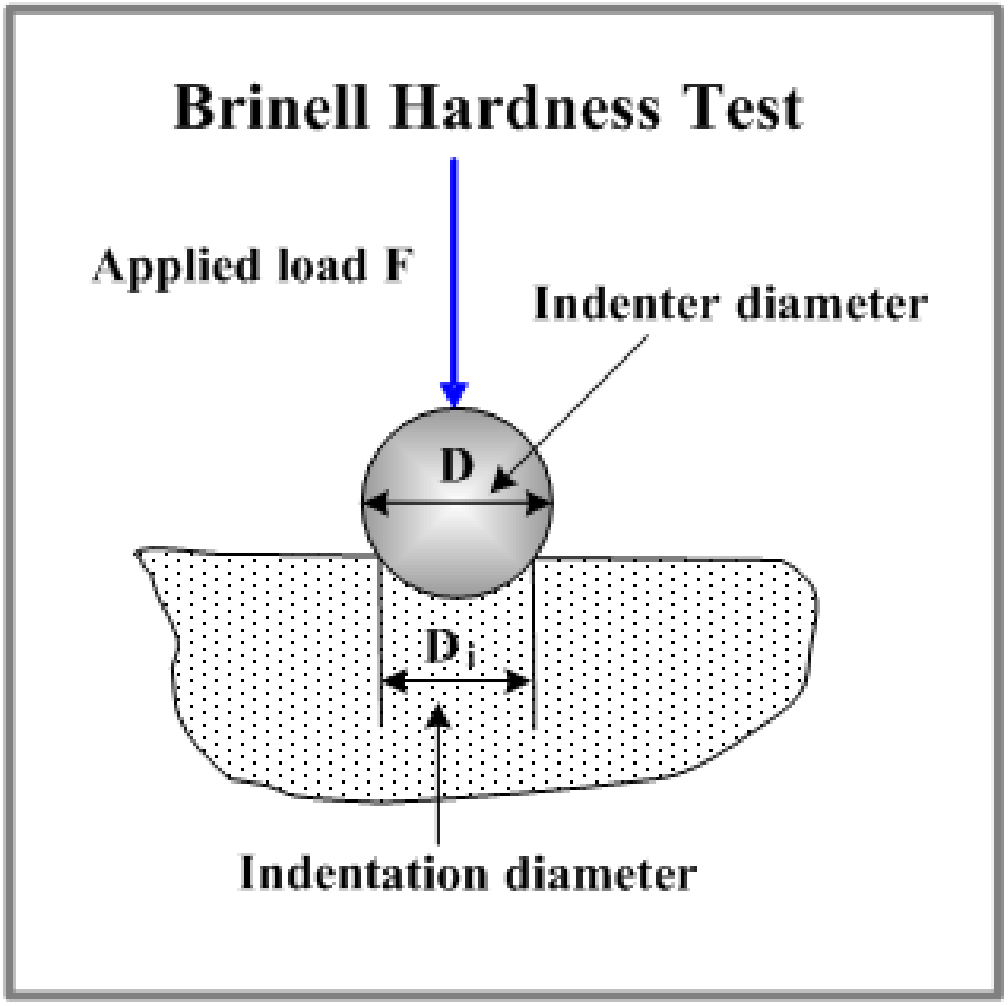

Figure 3.2: Brinell hardness test setup method. Adapted from [166].

where F = applied load in kg, D = indenter diameter in mm and D_i is indentation diameter in mm.

For an accurate hardness measurement, hard alloy specimen should be seven times or more thicker than the indentation depth while soft alloys should be fifteen times or more thicker than indentation depth.

Vickers Hardness Test

The indenter in the Vickers Hardness test method is a square-based diamond pyramid. The loads vary form 1kgf to 120 kgf and it is applied for about 30 seconds. The length of the indentation created is measured with a microscope, and the microscope is often an integral part of any Vickers hardness tester. The method is more accurate, as the impression produced is clearer than the impression of Brinell indenter. The Vickers number (H_V) is calculated by the formula:

$$H_V = \frac{1.854 \times F}{D^2} \qquad \text{(Equation 3.42)}$$

where F = applied load in kg, D = length of the impression diagonal in mm.

Knoop Hardness Test

The indenter in the Knoop test is also a diamond pyramid with an angle of 130 ° and 170 °30′ respectively. The loading forces used in this testing method ranges from 10gf - 1000gf. The penetration depth of the indenter is usually very small which is why the method is more suitable to soft material and thin coating.

The Knoop hardness number (H_K), is calculated by the formula:

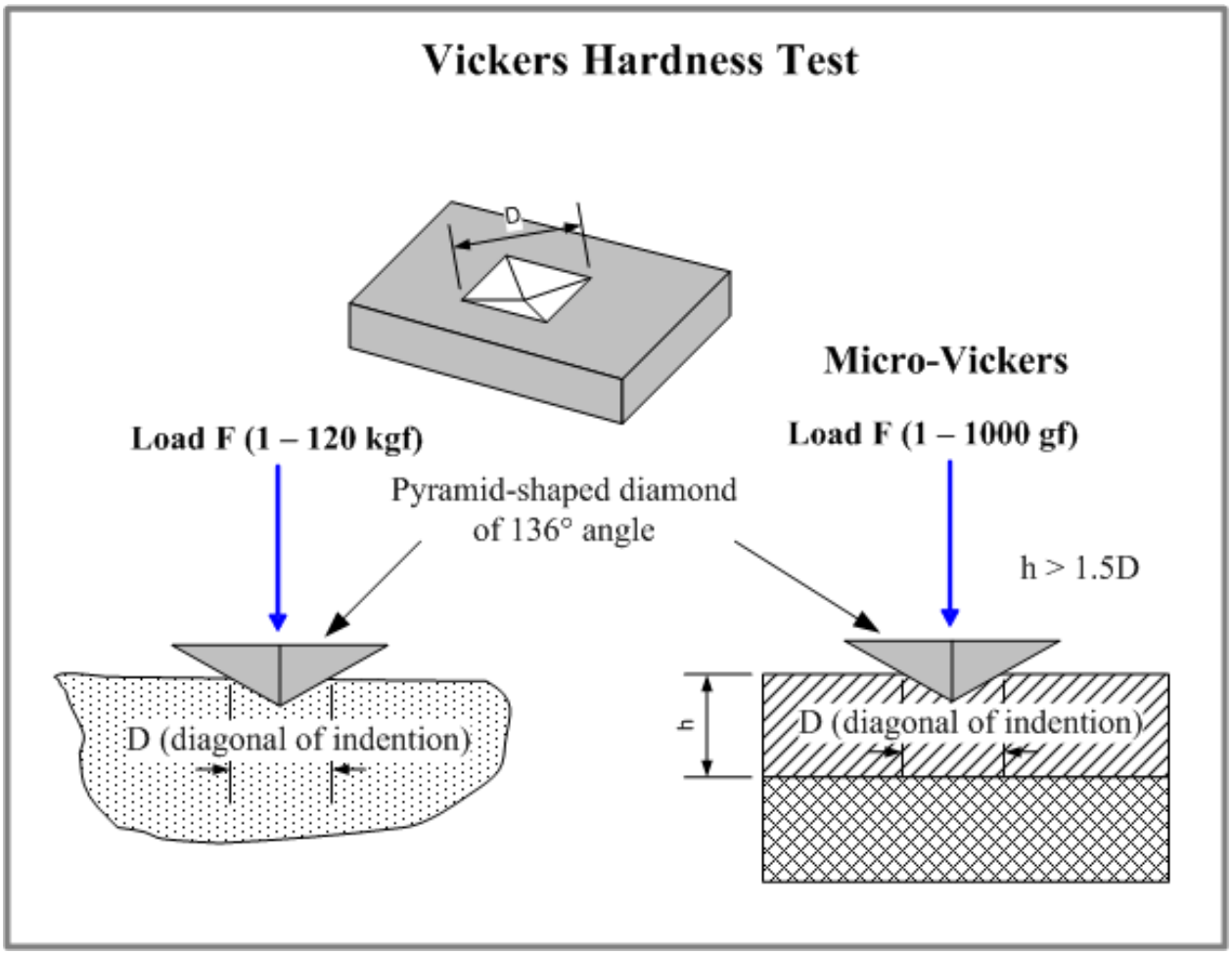

Figure 3.3: Vickers hardness test setup method. Adapted from [166].

$$H_K = \frac{14.229 \times F}{L^2} \qquad \text{(Equation 3.43)}$$

where F = applied load in kg, and L = long diagonal of the impression in mm.

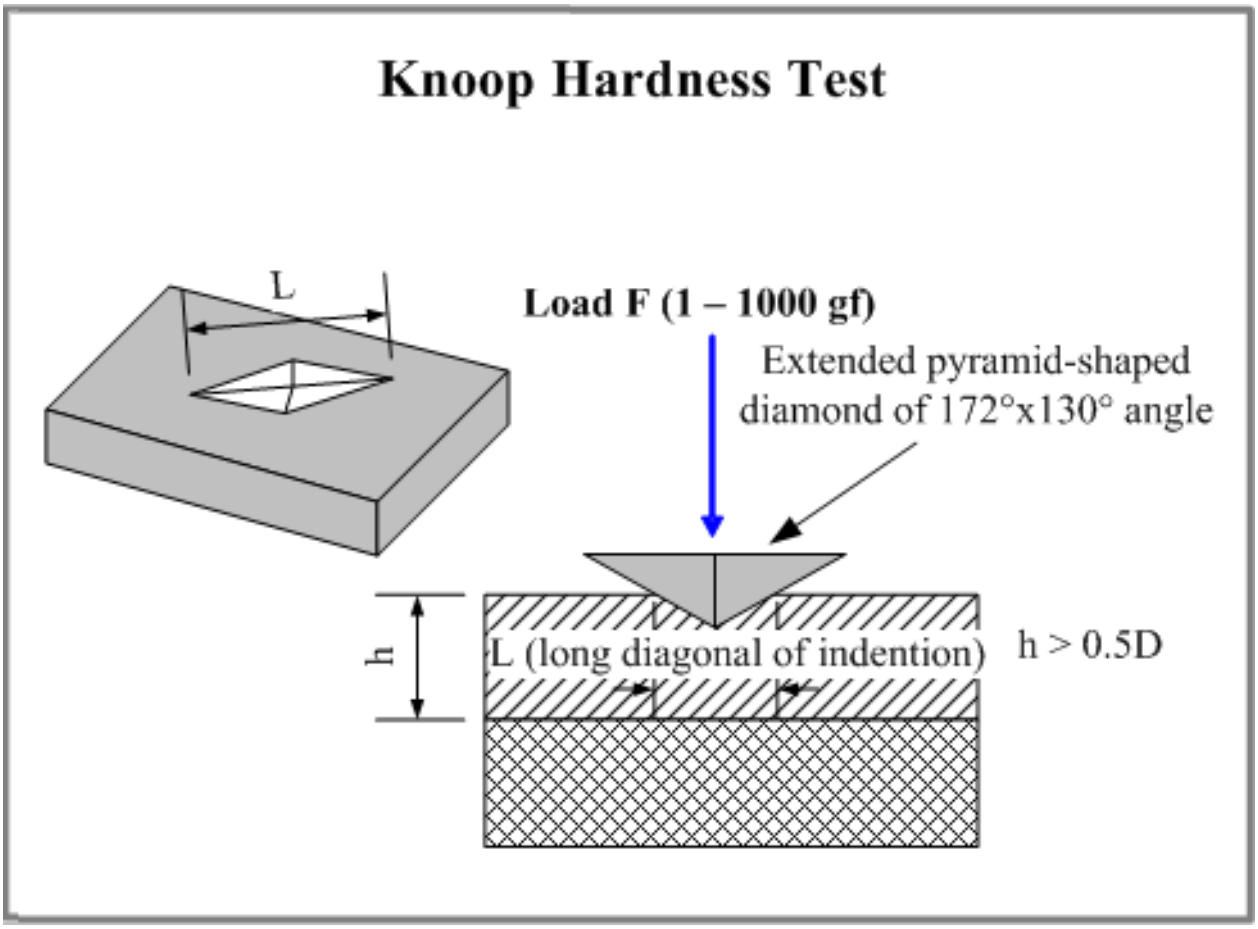

Figure 3.4: Knoop hardness test setup method. Adapted from [166].

Rockwell Hardness Test

Two types of indenter are used in the Rockwell hardness tests. The first is a hardened steel ball of diameter $1/16''$ and $1/8''$ or a spherical diamond cone of $120\,°$. Before making any test, the penetration depth indicator is first adjusted to zero, after which the indenter (60 - 150 kgf) is applied. The penetration depth is measured after removal of the major load.

Rockwell method are categorized in different scales (A, B, C, D, E, F, G, H, K) and in

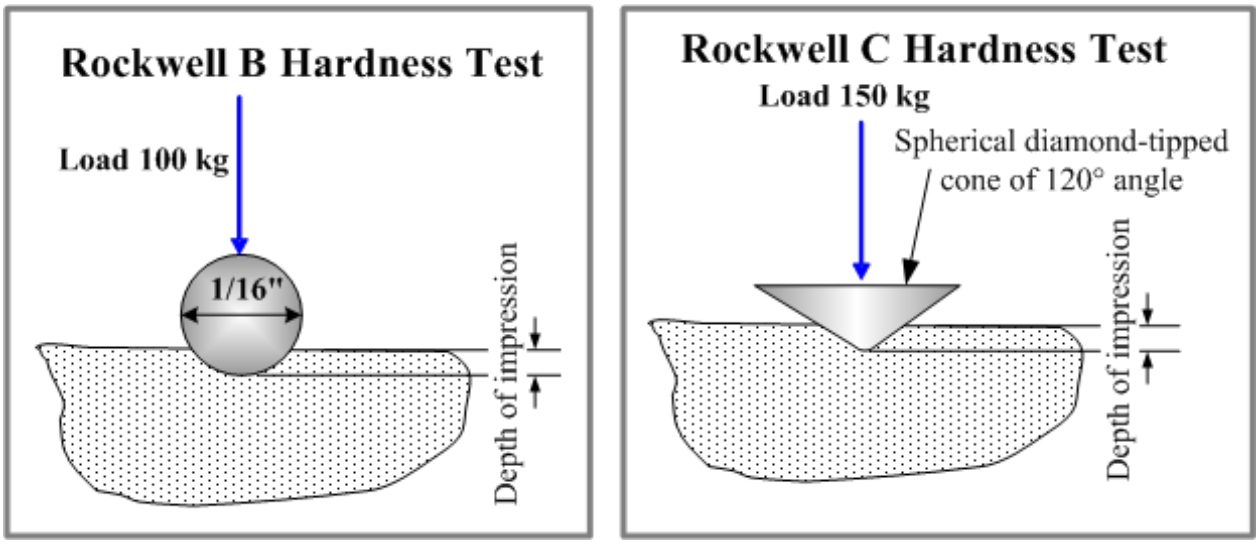

Figure 3.5: Rockwell hardness test for scale B and C. Adapted from [166].

numbers, with no units. The setup for scales B and C are shown in Figures 3.4. For soft steels, aluminum alloys and copper alloys, the Rockwell hardness scale B is applicable. Harder alloys such as cast iron, then the Rockwell hardness scale C is more applicable. For example, a Rockwell test result of 53 H_RC, will mean, 53 units, measured in the scale C by the Rockwell Hardness (H_R) method.

Hardness can be studied indirectly because it correlates to several physical properties such as ionicity, melting point, elasticity, cohesive energy, etc. [167]. From the basic crystal-chemical parameters, several formulae have been proposed for estimating hardness of materials. These formula contain terms involving valence and mean interatomic distance, as well as various constants related to such factors as the crystal structure, the valency of the bonds, the co-ordination number and atomic number. From mechanical point of view, the hardness of a material is usually defined as the resistance of the material to deformations [11]. Therefore,

because the Bulk Modulus (i. e. the elastic response of a material to hydrostatic pressure) scales roughly with hardness [165, 168, 169], it has been used with success as a guide for theoretical predictions of hard materials. The Bulk Modulus, B, is a measure of the resistance of a material to volume change.

It has been shown that the Shear Modulus (i.e. the material's resistance to shape change) is more correlated to hardness than the Bulk Modulus [170, 171, 172]. One of the methods for predicting hardness in non-metallic solids include the volumetric cohesive energy ($\frac{U}{V}$). U = cohesive or structure energy and V = molecular volume. The unit is given in kcal.cm^{-3}. In the case of Mohs hardness (H_m) scale [173], $\frac{U}{V}$ is expressed as:

$$\frac{U}{V} = 24[H_m - 2.7] \qquad \text{(Equation 3.44)}$$

$4 < H_m < 9$ for "hard core solids"

$$\frac{U}{V} = 48[H_m - 3.3] \qquad \text{(Equation 3.45)}$$

$H_m > 4$ for "soft core solids",

$$\frac{U}{V} = \frac{1}{2}H_m^3 \qquad \text{(Equation 3.46)}$$

$H_m > 4$ for all solids

The"hardcore" is defined as binary solids either of the AB type in which one or both has an atomic number below 10, or of any other type in which one element has an atomic number below 10 and the other element has an atomic number below 18. "Soft-core" solids include all others.

Hardness and toughness are important properties of engineering materials. Since hard materials are less responsive to plastic deformation and are brittle, cracks can be initiated and/or propagated easily thereby limiting their potential use where deformation would occur [174]. Toughness is defined as the ability of a material to withstand plastic deformation before fracturing. For most materials, some degree of toughness is required, depending on the actual use . Room temperature toughness of a material is important. Toughness can also be defined as the ability of a material to withstand plastic deformation without rupture [175]. The toughness (ductility) of many materials can change if conditions are altered. An increase in temperature will usually increase ductility and a decrease in temperature will usually reduce ductility [175]. Additions to metals (i.e. alloying) or impurities, can alter the ductility, as can heat treatment [175]. There are many heat treatments which affects the phases, their microstructure and so the properties.

Figure 3.1 shows that the Poisson's ratio is related to the elongation (and by extension, the ductility) of crystalline alloys and amorphous metals [176, 177, 178, 179, 180]. At low temperatures, the higher the Poisson's ratio, the better the ductility of a crystalline or amorphous metal. Niobium (bcc) for example has 0.40 Poisson's ratio at room temperature and it has an elongation of 44%; gold (fcc) has a Poisson's ratio of 0.42 and an elongation of 50% [176, 178]. Other ductile metals which are fcc such as palladium, copper and silver also have high values of Poisson's ratio. Metals with low values of Poisson's ratio are known to be brittle, and the crystal structure has also to be considered. A good example is beryllium, which is hexagonally close-packed, and has a Poisson's ratio value of 0.08, and tensile elongation of only 1% . In wholly or partially amorphous metallic alloys, similar trends are also evident [179, 180]. A classification rule was given by Frantsevich et al. [181] to distinguish brittleness and ductility by Poisson's ratio. The critical value for Poisson's ratio is 1/3. For brittle materials , the Poisson's ratio is less than 1/3.

Another empirical relation linking materials ductility and its elastic moduli (B/G)was proposed by Pugh . A high B/G ratio signified ductility while a low value corresponded to brittle nature [176]. The critical value separating ductile and brittle materials is around 1.75. If $B/G > 1.75$, the material behaves in a ductile manner, otherwise the material behaves in a brittle manner [176]. For engineering purposes, if two materials have the same hardness (assuming all other things are equal: melting point, density, ease of processing availability etc), that with the higher ductility is more likely to be preferred. It is possible to gauge ductility with the Poisson's or B/G ratio because it can be evaluated completely from first

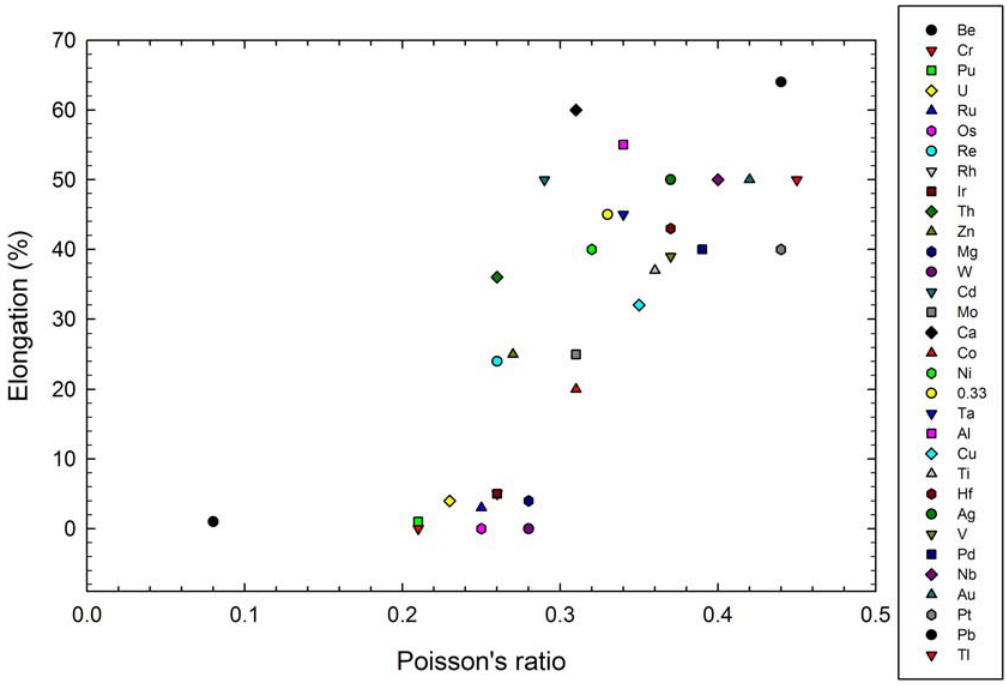

Figure 3.6: Elongation vs. Poisson's ratio for some pure elements (purity $\geq$ 99.95%). Adapted from [177, 178].

principles calculations without any additional empirical information [182].

The brittle-ductile behavior of selected cubic materials was studied by Pettifor [183], showing that the angular character of bonds relates to the Cauchy pressure $C_{12} - C_{44}$. A positive Cauchy pressure corresponded to metallic character in bonds, and therefore to ductile behavior of materials [183].

3.7 Debye Temperature

The Debye temperature (Θ_D), is defined as the highest temperature that a crystal can attain under single normal vibration. It is an essential quantity characterising phonon-related properties of materials [184]. It reflects the strength of bonds between its elements, structure stability, density and structure defects [185]. The connection between these properties and the elastic coefficient of poly-atomic solids was first introduced by the German physicist Paul Debye [186]. There is increased interest in calculating the Debye temperature of materials, because in combination with first principle total energy calculations, it offers a simple, but very effective, method to understand the ground state structure properties as well as the thermo-physical properties and phase stability of materials at finite temperatures [187, 188, 189].

According to the Debye theory the Debye temperature (Θ_D), can be calculated from density (ρ) data and the data related to the longitudinal (V_l) and transverse (V_t) wave velocities in the solid [190, 191, 192]:

$$\Theta_D = \frac{\hbar}{k_B}\left[\frac{3n}{4\pi}\left(\frac{N_A\rho}{M}\right)\right]^{1/3} v_m \qquad \text{(Equation 3.47)}$$

where k_B is the Boltzmann's constant, $\hbar$ is Planck's constant, N_A is Avogadro's number, M is the molecular mass, n is the number of atoms per formula unit, ($\rho = M/V$) is the density

and v_m is the average sound velocity, which is further expanded as [193]:

$$v_m = \left[\frac{1}{3}\left(\frac{2}{v_l^3} + \frac{1}{v_t^3}\right)\right]^{-1/3} \qquad \text{(Equation 3.48)}$$

Since the Debye temperature is related to many material properties such the elastic constants, specific heat, hardness and melting temperature, its theoretical calculations is made possible using the frozen phonon approach [194], linear response theory [195] , or the *ab initio* force constant method [191, 196]. However, all of these schemes are computationally demanding. In easier way, the Debye temperature can be approximated from elastic moduli [197, 198], using the sound velocity [199]. For nonmagnetic systems, an approximation in which the average sound velocity correlates to the *ab initio* bulk (B) and shear (G) modulus is [193, 200]:

$$v_l = \left(\frac{3B + 4G}{3\rho}\right)^{1/2}, v_t = \left(\frac{G}{\rho}\right)^{1/2} \qquad \text{(Equation 3.49)}$$

Without any detailed knowledge of the phonon spectrum of a compound, the Debye temperature can be calculated, since the elastic constants is obtainable easily from first principles calculations. Due to bond mixture in some crystal structures, Equation 3.47 is not universal. With the exception of the alkali metals, it is poorly fulfilled for other cubic elements and compounds [201]. At zero temperature, an expression given by Blackman [202, 203] showed a better relationship between Debye temperature and elastic constants, for various cubic

structures [201].

$$\Theta_D = C_B(\frac{aG_B}{M})^{\frac{1}{n}} \quad \text{(Equation 3.50)}$$

$$G_B = [c_{44}(c_{11} - c_{12}(c_{11} + c_{12} + 2c_{44})]^{\frac{1}{3}} \quad \text{(Equation 3.51)}$$

$$C_B = 3.89 \times 10^{11} s^{\frac{-1}{6}} \frac{\hbar}{k_B} \quad \text{(Equation 3.52)}$$

where $\hbar$ = Plancks constant, k_B = Boltzmann constant and s = no of atoms per formular unit.

On the average, a crystal with a large Debye temperature should be a stiffer crystal. This is because the optical phonons have a higher frequency and therefore require greater energy to activate.

3.7.1 Melting Point

The melting point (m. p.) of a material refers to the temperature at which the substance changes from the solid to the liquid state. In other words, is the temperature at which

the vapor pressure of the solid and the liquid are equal is regarded as the melting point of the solid. At the melting point, the solid and liquid phase are equal. While the melting and freezing points of most substances are approximately equal (e.g. mercury), certain substances possess different solid-liquid transition temperatures on heating or cooling(e.g. agar). Unlike the boiling point, the melting point of a solid is relatively insensitive to pressure, because there is only a small change in volume between solid/liquid transition phases [204]. It is more difficult to compress a solid and liquid than a gas.

The melting point of a pure substance is usually higher than for an alloy or impure substance. The more impurity present, the lower the melting point and the broader the melting temperature range [205], pure metal has single melting point, while alloys have both a *solidus* (temperature at which melting starts) and *liquidus* temperature (temperature at which the alloy is completely molten). Materials that have high melting points, like tantalum, niobium, molybdenum and tungsten are refered to as refractory materials. The element with the highest melting point is tungsten (3410 °C). Tantalum hafnium carbide (Ta_4HfC_5) is a refractory compound with a very high melting point of 4215 °C [205].

At the melting point, while the enthalpy (H) and the entropy (S) of the material are changing ($\triangle H, \triangle S > 0$) the Gibbs free energy ($\triangle G$) of the material is zero [205]. Melting occurs for a particular material when the latent heat of fusion of the liquid becomes lower than that for the solid. At various pressures, this happens at a specific temperature which is known to be:

$$T = \frac{\triangle H}{\triangle S} \qquad \text{(Equation 3.53)}$$

where $\triangle H$, $\triangle S$, and T are the change of enthalpy of melting, change of entropy of melting and temperature at the melting point.

The melting point of bulk crystalline materials can be predicted, based on the Lindemann criterion [206]. The Lindermann criteria specifies an increase in thermal vibrations with increase in temperature. Melting is initiated at large enough vibrations when adjacent atoms partly occupy the same space. The Lindemann criterion conludes that melting begins when the vibration amplitude exceeds a certain threshold value. If all the atoms in a crystal are assumed to vibrate with the same frequency, then the average thermal energy E, of the system can be estimated using the equipartition theorem [207];

$$E = 4\pi^2 m\nu^2 \; u^2 = k_B T \qquad \text{(Equation 3.54)}$$

where T is the absolute temperature, m is the atomic mass, k_B is the Boltzmann constant, ν is the frequency and u is the average vibration amplitude. Should the threshold value of $u^2 = c^2 a^2$ then the melting point can be estimated as:

$$T_m = \frac{4\pi^2 m\nu^2 c^2 a^2}{k_B} \qquad \text{(Equation 3.55)}$$

where c is the Lindemann constant and a is the atomic spacing.

Other expressions for evaluating melting points are possible [208], depending on how the average thermal energy is obtained. One of such commonly used expression is based on the Lindemann criterion [209]:

$$T_m = \frac{m\nu^2 c^2 a^2}{k_B} \qquad \text{(Equation 3.56)}$$

If the expression for the Debye frequency ν is replaced in Equation 3.56, then the melting temperature becomes:

$$T_m = \frac{2\pi m c^2 a^2 \Theta_D^2 k_B}{\hbar^2} \qquad \text{(Equation 3.57)}$$

where $\hbar$ is the Planck constant and Θ_D is the Debye temperature. Values of the Lindemann constant c, range from 0.15 - 0.3 for most materials [210].

The melting temperature of a material can be estimated from the elastic constants, where the

elastic constants and moduli are in GPa. For cubic crystals [211, 212], a simple relationship, empirically linking the equilibrium values of C_{ij} to the melting temperatures are:

$$T_m(K) = 553 + (591/Mbar)C_{11} \pm 300 \quad \text{(Equation 3.58)}$$

$$T_m(K) = 607 + (930/Mbar)B \pm 500 \quad \text{(Equation 3.59)}$$

$$T_m(K) = 277 + 8.16 \times E \quad \text{(Equation 3.60)}$$

For tetragonal systems, the expression is:

$$T_m = 354K + (450K/Mbar)[\frac{1}{3}(2C_{11} + C_{33})] \pm 300K \quad \text{(Equation 3.61)}$$

Chapter 4

Ab Initio Results for X_3Al Compounds

All the *ab initio* results in this work were derived with the *ab initio* simulation package (VASP). The exchange and correlation functionals were treated in the generalized gradient approximation of Perdew-Burke-Ernzerhof [108] with projector augmented wave (PAW) potentials [125]. An energy cutoff of 500 eV was used for the plane wave basis to achieve energy convergence within 10^{-5} eV. These conditions were maintained both for structure relaxations and density of states (DOS) calculations. The Brillouin zone was sampled with an 8×8×8 grids for structure relaxations and 16×16×16 for the DOS according to the Monkhorst-Pack scheme [115]. A face-centered cubic structure (space group $Pm\overline{3}m$) similar to Ni_3Al was adopted for each binary system. Atoms occupy two inequivalent sites, where the noble metals, X, are located at $(0, \frac{1}{2}, \frac{1}{2}), (\frac{1}{2}, 0, \frac{1}{2}), (\frac{1}{2}, \frac{1}{2}, 0)$ and the Al atoms at (0, 0, 0).

4.1 Properties of X_3Al compounds

The calculated lattice parameter, elastic constants and theoretical density (ρ^{cal}) for the base elements and compounds in the stoichiometry X_3Al (where X = Pt, Ir, Pd, Ru, Os) are shown in Tables 4.1 and 4.2. For all the compounds, the elastic stiffness coefficients (c_{11}, c_{12} & c_{44}) satisfied the generalized mechanical stability criteria, Equation 3.35.

Given in Table 4.2. are the calculated elastic moduli, Debye temperature, heats of formation and the melting points calculated within the PAW-GGA framework. All the moduli were computed using the Voigt-Reuss-Hill averaging methods.

The experimental lattice constants and elastic parameter for many of these compounds are presently not available in the literature. For lack of experimental data , these lattice constants and elastic moduli cannot be compared. It is therefore strongly suggested that an experimental study of the elastic moduli be carried out in order to verify the theoretical results. For the noble metal elements however, the proximity between the theoretical results and experimental data suggest that the calculations are accurate and reliable enough for predictions. In the binary compositions, the results showed that rhodium, ruthenium and palladium based alloys are much lighter that iridium, osmium and platinum based alloys. When one atom of rhodium, ruthenium or palladium (about 25% of the binary composition) was substituted with platinum (ternary alloying), an increase of about 52% in density was observed (i.e. ρ^{cal} of Pd_3Al = 7.43 $g.cm^{-3}$ while ρ^{cal} for $PtPd_2Al$ was 11.28 $g.cm^{-3}$).

Table 4.1: Calculated lattice parameter and the elastic constants (c_{ij}). All the elastic constants are in GPa and experimental data are in square brackets.

Material	Cell ($\AA$)	c_{11}	c_{12}	c_{13}	c_{22}	c_{23}	c_{33}	c_{44}	c_{55}
Al	**4.025 [4.050]**[a]	**125 [108]**[b]	**49 [61]**[b]					**40 [29]**[b]	
Ir	**3.876 [3.839]**[a]	**570 [590]**[c]	**251 [249]**[c]					**237 [262]**[c]	
Pd	**3.954 [3.891]**[a]	**202 [227]**[c]	**159 [176]**[c]					**73 [72]**[c]	
Rh	**3.843 [3.803]**[a]	**408 [413]**[c]	**192 [194]**[c]					**174 [184]**[c]	
Pt	**3.977 [3.803]**[a]	**306 [347]**[c]	**231 [251]**[c]					**76 [76]**[c]	
Ru		**569 [563]**[d]	**223 [188]**[d]	**180 [168]**[d]			**651 [624]**[d]	**173 [181]**[d]	**174**
Os		**767**	**270**	**231**			**832**	**249**	**243**
Ni_3Al	**3.591 [3.572]**[c,d]	**235 [230]**[c,d]	**157 [150]**[c,d]					**128 [131]**[c,d]	
Ir_3Al	**3.863**	**389**	**239**					**164**	
Os_3Al	**3.863**	**407**	**270**					**66**	
Pd_3Al	**3.906**	**171**	**125**					**87**	
Pt_3Al	**3.919 [3.920]**[e]	**327**	**179**					**115**	
Rh_3Al	**3.835**	**271**	**196**					**128**	
Ru_3Al	**3.833**	**217**	**184**					**79**	
Pt_2IrAl	**a = 3.983; b,c = 3.889**	**378**	**178**		**352**	**207**		**147**	**155**
$PtIr_2Al$	**a,b = 3.895; c = 3.848**	**367**	**183**	**230**			**333**	**149**	**173**
Pt_2OsAl	**a = 4.006; b,c = 3.845**	**369**	**190**		**326**	**246**	**143**	**177**	
$PtOs_2Al$	**a,b = 3.799; c = 4.048**	**392**	**244**	**214**			**371**	**49**	**147**
Pt_2PdAl	**a = 3.879; b,c = 3.933**	**268**	**171**		**287**	**167**		**96**	**106**
$PtPd_2Al$	**a,b = 3.903; c = 4.047**	**212**	**152**	**137**			**219**	**85**	**73**
Pt_2RhAl	**a = 3.942; b,c = 3.864**	**320**	**174**		**317**	**188**		**131**	**144**
$PtRh_2Al$	**a,b = 3.888; c = 3.807**	**313**	**156**	**192**			**298**	**123**	**149**
Pt_2RuAl	**a = 4.032; b,c = 3.825**	**313**	**178**		**297**	**230**		**126**	**179**
$PtRu_2Al$	**a,b = 3.791; c = 4.011**	**310**	**202**	**204**			**295**	**59**	**133**

[a]Refs [78, 83], [b]Ref [203], [c,d]Refs [177, 213], [e]Ref [214].

Table 4.2: Calculated Modulus (B, G, E), Poisson's ratio (v), density(ρ^{cal}), Debye temperature, Θ_D, (K), melting temperature (MT$\pm$300K) and heat of formation (H_f) in eV/at. All moduli are in GPa and experimental data are in square brackets.

Material	B	G	E	B/G	v	$\rho^{cal}(g.cm^{-3})$	P^c	Θ_D	MT	$\triangle H_f$
Al	76 [76]	42	107	1.79	0.26 [0.35]	2.8 [2.7]	12	544 [433]	1289 [933]	
Pt	256 [278]	65 [61]	179 [168]	3.95	0.38 [0.38]	21 [21]	155	265 [237]	2361 [2041]	
Ir	357 [355]	226 [210]	560 [528]	1.58	0.24 [0.26]	22 [22]	14	450 [420]	3922 [2739]	
Pd	174 [180]	52 [44]	142 [121]	3.35	0.37 [0.39]	11 [12]	86	307 [271]	1745 [1828]	
Rh	264 [270]	161 [150]	402 [275]	1.63	0.25 [0.26]	12 [12]	17	518 [512]	2962 [2237]	
Os	425 [418]	255 [222]	639	1.67	0.25 [0.25]	22 [22.6]	-	426 [467]	3903 [3306]	
Ru	338 [321]	184 [173]	467 [447]	1.78	0.26 [0.30]	12 [12.4]	-	491 [555]	3037 [2607]	
Ni_3Al	183[171]	92	237	1.98	0.28 [0.40]	6.14[7.26]	29	268	1942	
Ir_3Al	289	136	352	2.34	0.30	12.63	76	282	2846	-0.40
Os_3Al	316	73	204	4.31	0.39	12.50	205	234	2957	+0.15
Pt_3Al	228	108	279	2.12	0.30	12.24	64	255	2486	-0.69
Pd_3Al	140	60	158	2.33	0.31	7.43	38	247	1566	-0.62
Rh_3Al	220	91	240	2.42	0.32	7.64	68	308	2155	-0.46
Ru_3Al	195	51	140	3.85	0.38	7.55	105	240	1835	-0.03
Pt_2IrAl	245	124	319	1.98	0.28	14.87	-	254	1998	-0.55
Pt_2OsAl	253	119	308	2.13	0.30	14.79	-	250	1934	-1.89
Pt_2PdAl	206	82	218	2.51	0.32	12.29	-	227	1575	-0.67
Pt_2RhAl	225	109	282	2.06	0.29	11.98	-	258	1774	-0.64
Pt_2RuAl	231	108	279	2.14	0.30	11.50	-	257	1724	-1.75
$PtIr_2Al$	261	127	328	2.06	0.29	15.71	-	258	1939	-0.44
$PtOs_2Al$	278	101	269	2.75	0.34	21.99	-	237	2062	-2.28
$PtPd_2Al$	166	61	162	2.72	0.34	11.28	-	216	1308	-0.64
$PtRh_2Al$	223	110	283	2.03	0.29	12.50	-	284	1727	-0.57
$PtRu_2Al$	237	85	229	2.79	0.34	12.41	-	257	1712	-2.85

Experimental data are from Refs [29, 77, 78, 83, 215, 216, 217].

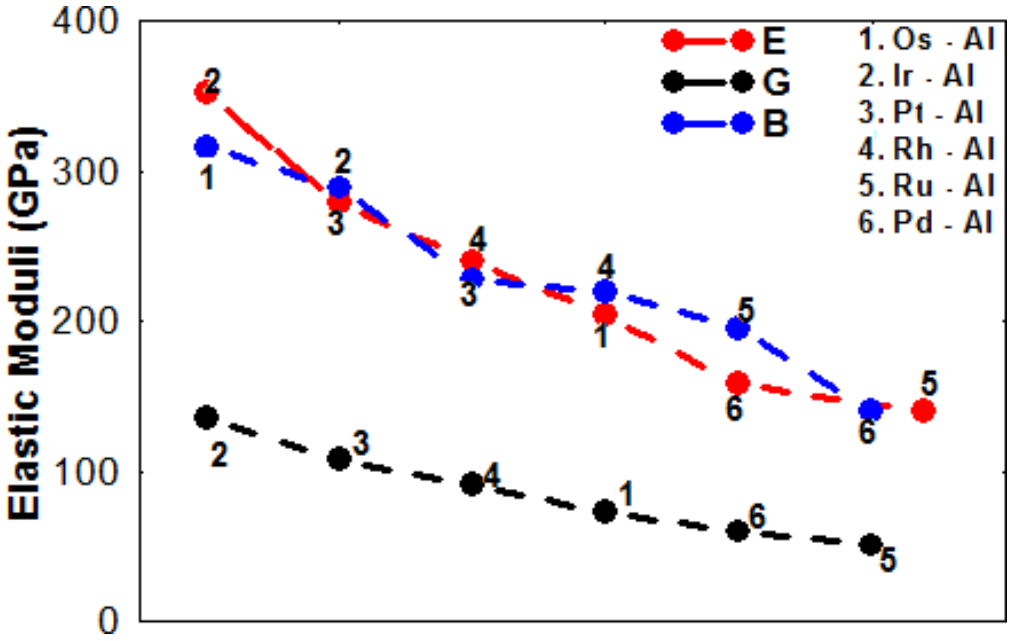

Figure 4.1: Bulk (B), shear (G) and Young (E) modulus trends in X_3Al noble metal compounds,

The final structure of the ternary alloys Pt_2XAl/PtX_2Al was found not to be $L1_2$. but a tetragonal ($L1_0$) structure, hence the six elastic constants describing the compounds.

The trends for the elastic moduli (i.e. bulk, shear and Young modulus) are shown in Figure 4.1. The bulk modulus increases from palladium (Pd) based alloys to iridium and osmium based alloys. Accordingly, the compressibility of these alloys increases in the sequence $c(Os_3Al) < c(Ir_3Al) < t(PtPd_2Al)$. Since strong correlation exists between the shear modulus and hardness of a material, we conclude from these data that the material with the highest hardness are the iridium based alloys, while the lowest hardness will be for ruthenium based alloys. Comparing the elastic moduli (i.e. B & G), most of the noble metal compounds should be mechanically better than Ni_3Al. If the Pugh criteria (ie. $B/G > 1.75$) is adopted to gauge ductility, then all the noble metal compounds are predicted to be ductile.

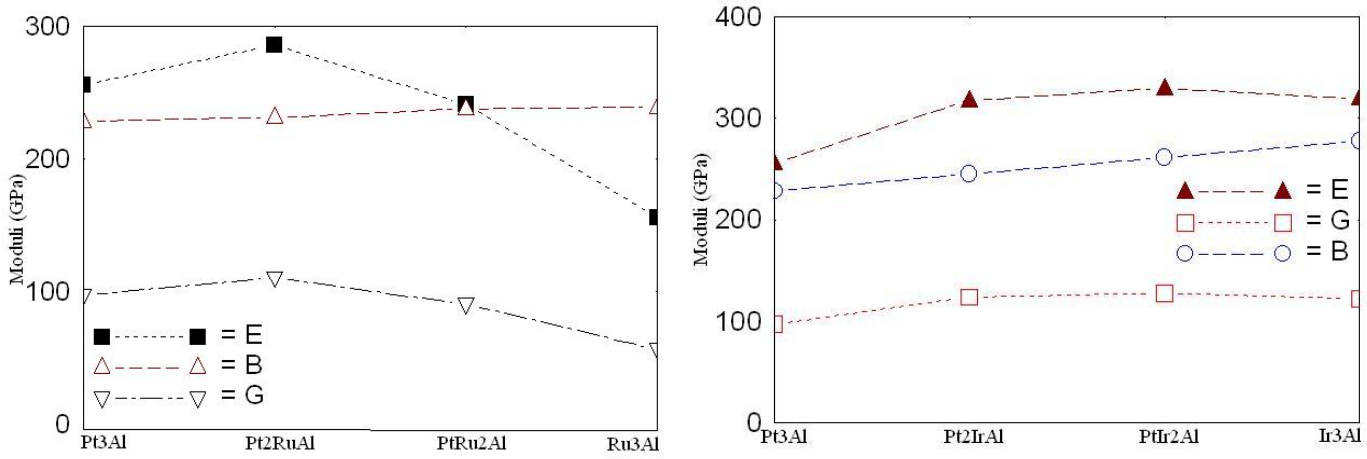

Figure 4.2: Elastic Moduli trends in $Pt - Ru - Al$ (left) and $Pt - Ir - Al$ (right) systems

The effect of change in the elastic moduli due to replacement of one atom of Pt *per unit cell* in each compound are shown in Figures 4.2 - 4.4. According to the results in Figure 4.2 (left), replacement of one atom of Pt with Ru in $Pt - Ru - Al$ system showed an improvement both in the Young (E) and Shear (G) moduli. Beyond one atom of Pt replacement, the Young and Shear moduli drastically reduced. However, the Bulk modulus (B), was steadily improved across the entire atom replacement regime. Pt substitution with Ir in the Pt-Ir-Al system, showed steady improvements in B, while the improvements in G & E are similar and not substantial after one Pt atom replacement (see Figure 4.2 (right)).

The trend in $Pt - Os - Al$ system (Figure 4.3 (left)) was similar to that earlier discussed in the $Pt - Ru - Al$ system. While steady improvement was observed in B, the best E and G values were obtained when one atom of Pt was replaced with Os. Further substitution of Pt with Os yielded no further improvement in E and G. Both E and G were improved when one atom of Rh was substituted for Pt (Figure 4.3 (right)). With additional Rh, a reduction

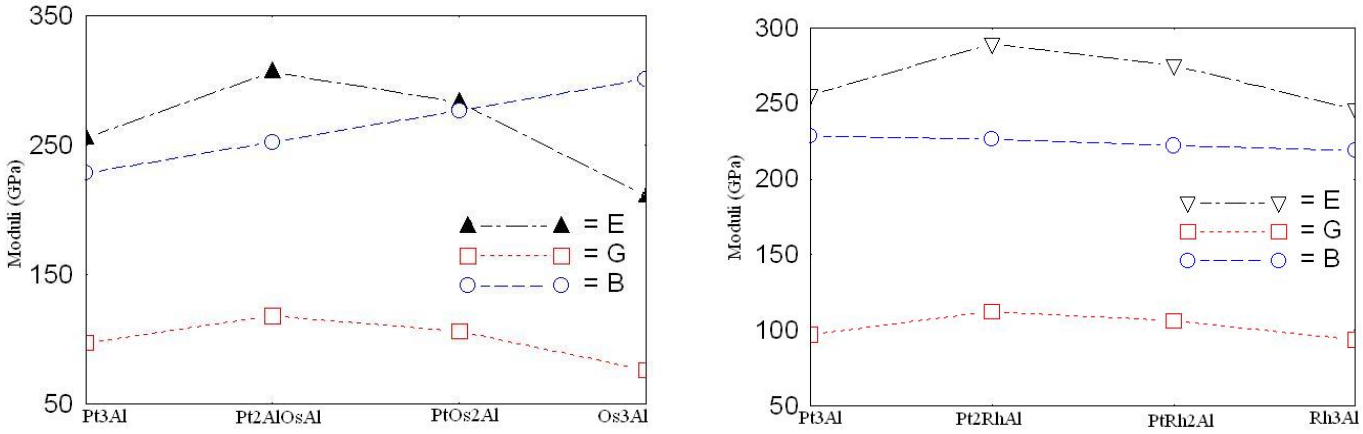

Figure 4.3: Elastic moduli trend in $Pt - Os - Al$ (left) and $Pt - Rh - Al$ (right) systems

in the values of all elastic moduli was observed.

Replacement of Pt with Pd within $Pt - Pd - Al$ system did not produce any encouraging result. All the elastic moduli (B, G & E) showed downward trend (see Figure 4.4).

4.2 Electronic Density of States of cubic binary X_3Al compounds

Valuable information, particularly regarding phase stability can be obtained from electronic structure studies. The DOS plot for all the $L1_2$-X_3Al compounds are shown in Figures 4.5. At zero temperature and according to the DOS plots, the $L1_2$ structure is very unlikely in all the compounds. However, the $L1_2$ phase is achievable in Ir_3Al, Pt_3Al, Rh_3Al and Os_3Al. The density of states at the Fermi level for this compounds are small compared to that of Pd_3Al and Ru_3Al. Due to the Fermi level been on the non-bonding side of their DOS plots,

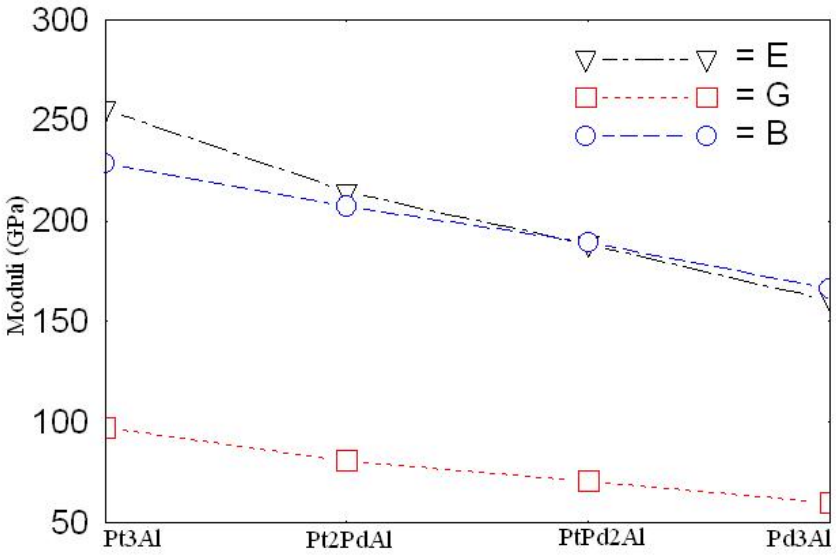

Figure 4.4: Elastic moduli in $Pt - Pd - Al$ alloy system

interstitial ternary alloying with elements having high electrons (i.e. Palladium, Cobalt, Chromium etc) should lead into a more stable $L1_2$ structure in Ir_3Al, Pt_3Al and Rh_3Al. With the E_F falling on a sharp peak and close to the pseudogap, the compound Pt_3Al is predicted to be a ductile compound, with low self diffusion and reduced creep.

The Fermi level of Pd_3Al and Ru_3Al are on the anti-bonding side of the DOS plots. These compounds will be metastable. To achieve the $L1_2$ structure in these compounds, energy reduction is necessary and this could be achieved by adding low-electron elements such as Ru, Rh, Mo, Nb and Lr. For the ternary alloy to have lightweight, the density of the chosen element must be given consideration.

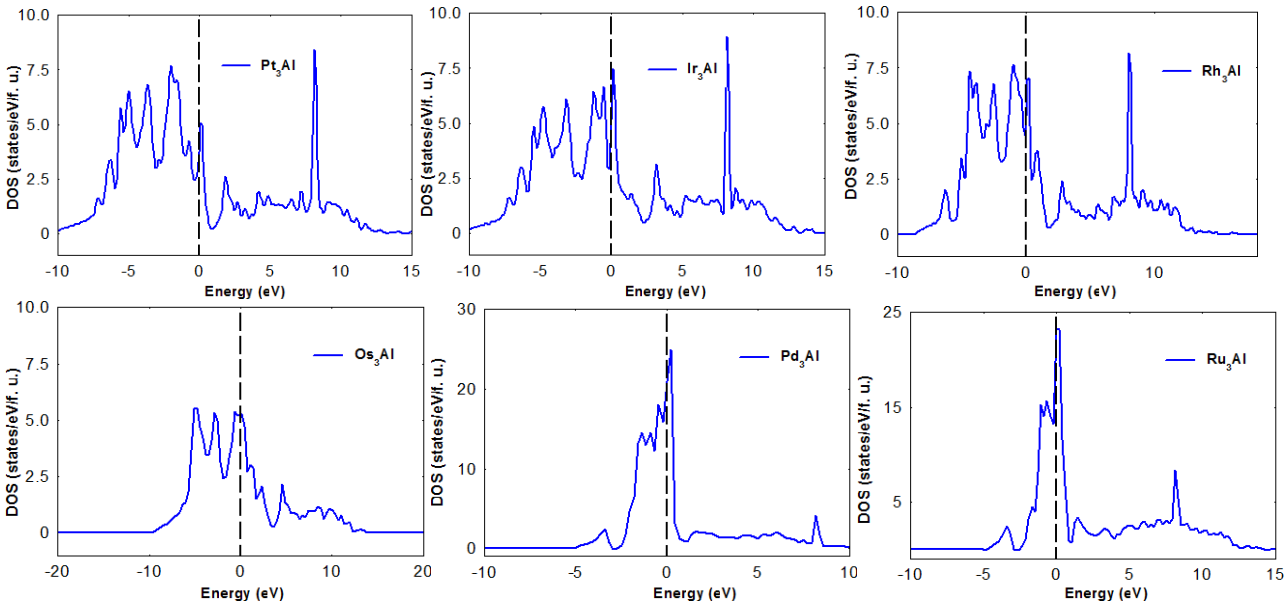

Figure 4.5: The total electronic density of states for phases of X_3Al compounds. Energies relative to Fermi level are indicated by the dotted vertical line.

4.3 Summary

The bulk modulus was highest for Os_3Al and least for Pd_3Al. The shear modulus was highest for Ir_3Al and this phase is predicted the hardest compound compared with Ru_3Al that had the least shear modulus value. The compound with highest melting point was Os_3Al. Melting point in the compounds show similar trend to the bulk modulus (i.e. high bulk modulus corresponded to high melting point). Although, Os_3Al had the highest bulk modulus and melting point, its heat of formation was positive and its phase stability was unfavorable as shown by the DOS calculations. There is no reported phases in Os-Al, while the stoichiometry; Ir_3Al, Rh_3Al, Pd_3Al and Ru_3Al does not exist on phase diagrams [218, 219]. The calculated $\triangle H_f$ agreed with the phase diagrams on the existence of $L1_2$-Pt_3Al. The DOS calculation also agreed with the phase diagrams on the instability of $L1_2$-Pt_3Al at

ground state. The heats of formation for most of the other compounds are small. However, as shown by the DOS plots, additional elements into some of the compounds (i.e. Pt_3Al) would play a significant role at getting a more stable structure at ground state. The results in Table 4.2, showed that none of the ternary (i.e. Pt_2XAl/PtX_2Al) compounds had better melting/mechanical properties compared with the binary compounds (X_3Al). However, on overall, all the X_3Al compounds had higher melting points and elastic properties compared with Ni_3Al.

Chapter 5

Semi-empirical Molecular Dynamics

5.1 Introduction

Molecular Dynamics (MD) is a technique for computing thermodynamic and kinetic properties of molecular systems using Newton equations of motions. The MD method was first used to study the interactions of hard spheres by Alder and Wainwright [220, 221]. A first set of realistic potential was used to study liquid argon [222, 223]. In MD calculations, information which include atomic positions and velocities are generated at the microscopic level. Macroscopic observables such as the energy, the pressure, the heat capacities etc, are then evaluated. To evaluate these macroscopic quantities, Newtons second law or the equation of motion has to be solved.

The Newtons second law can be written as:

$$\vec{F_i} = m_i \vec{a_i} \qquad \text{(Equation 5.1)}$$

$\vec{F_i}$ = force on particle i, m_i = mass of particle i and $\vec{a_i}$ = acceleration of particle i. The relationship between the force and the gradient of the potential energy V, is also defined as:

$$\vec{F_i} = -\nabla_i \vec{V} \qquad \text{(Equation 5.2)}$$

Combining Equation 5.1 and Equation 5.2 will yield Equation 5.3.

$$-\frac{d\vec{V}}{dr_i} = m_i \frac{d^2 \vec{r_i}}{dt^2} \qquad \text{(Equation 5.3)}$$

as a function of time, Equation 5.3 relates the derivative of the potential energy $\vec{V}$ to the change in position.

For constant acceleration, the Newton's second law can be re-written as:

$$\vec{F} = m\vec{a} = m\frac{d\vec{v}}{dt} = m\frac{d^2\vec{x}}{dt^2} \qquad \text{(Equation 5.4)}$$

where

$$\vec{a} = \frac{d\,\vec{v}}{dt} \qquad \text{(Equation 5.5)}$$

which after integration becomes:

$$\vec{v} = \vec{a}\,t + \vec{v_0} \qquad \text{(Equation 5.6)}$$

and since

$$\vec{v} = \frac{d\,\vec{x}}{dt} \qquad \text{(Equation 5.7)}$$

Equation 5.7 is integrated to obtain:

$$\vec{x} = \vec{v}\,t + \vec{x_0} \qquad \text{(Equation 5.8)}$$

combining Equation 5.6 and Equation 5.8 gives:

$$\vec{x} = \vec{a}\,t^2 + \vec{v_0}\,t + \vec{x_0} \qquad \text{(Equation 5.9)}$$

Equation 5.9 gives the expression that relates $\vec{x}$ at time t to the acceleration, $\vec{a}$, where the

initial position is $\vec{x_0}$, and the initial velocity is $\vec{v_0}$.

The derivative of the potential energy with respect to position $\vec{r}$, gives the acceleration as:

$$\vec{a} = -\frac{1}{m}\frac{d\vec{E}}{dr} \qquad \text{(Equation 5.10)}$$

According to Equation 5.9 and Equation 5.10, the trajectory of a system is calculated by only knowing the initial positions of the atoms, their velocity distributions and the acceleration. Material properties are determined from the trajectories. This is a deterministic process [224, 225], since the positions and the velocities at time zero will determine the positions and velocities at all other times. A way to obtain the initial positions from experimental data structures includes NMR spectroscopy or x-ray crystallography.

The initial velocity is determined according to the Maxwell-Boltzmann or Gaussian distribution [226]:

$$P(\vec{v_i}) = \left(\frac{m_i}{2\pi k_B T}\right)^{\frac{1}{2}} exp\left[-\frac{1}{2}\frac{m_i\,\vec{v_i^2}}{k_B T}\right] \qquad \text{(Equation 5.11)}$$

At temperature T, the velocity $\vec{v_i}$ is a random choice, corrected to have an overall momentum of zero (Equation 5.12):

$$\vec{P} = \sum_{i=1}^{N} m_i \vec{v_i} = 0 \qquad \text{(Equation 5.12)}$$

The implication of Equation 5.11 is that an atom i at temperature T would have velocity v.

The temperature, T of a system can be evaluated from Equation 5.13, where N is the number of atoms in the system.

$$T = \frac{1}{3N} \sum_{i=1}^{N} \frac{|\vec{P_i}|}{2m_i} \qquad \text{(Equation 5.13)}$$

5.2 Integration Algorithms

The equations of motion can only be solved numerically. Analytical solution is impossible because the relationship between the potential energy and atomic positions in the system is somewhat complicated. Several numerical algorithms have been developed for integrating the equations of motion. Among molecular dynamics programmers, the most popular group of integration algorithms are the Verlet algorithms (listed below). They only differ slightly in their usefulness, but are of equivalent accuracy and stability [227, 228].

1. Verlet algorithm.

2. Leap-frog algorithm.

3. Beeman's Algorithm.

4. Velocity Verlet.

When choosing an algorithm for MD simulations, such an algorithm [228], must satisfy the fundamental requirements of:

Accuracy - does it give an accurate description of the atomic motion?

Stability - does it conserve the system energy and temperature?

Simplicity - is it easy to write a computer program for it?

Speed - does it calculate the atomic motion as quickly as possible?

Economy - does it use a minimum of computing resources e.g. memory.

All integration algorithms [225], assume that the velocities, positions and accelerations of each particle in a molecular system can be approximated by Taylor series expansion as:

$$r(t + \partial t) = r(t) + v(t)\partial t + \frac{1}{2}a(t)\partial t^2 + ... \qquad \text{(Equation 5.14)}$$

$$v(t + \partial t) = v(t) + a(t)\partial t + \frac{1}{2}b(t)\partial t^2 + ... \quad \text{(Equation 5.15)}$$

$$v(t + \partial t) = a(t) + b(t)\partial t + ... \quad \text{(Equation 5.16)}$$

Where v is the velocity, a is the acceleration and r is the position.

5.2.1 Verlet Algorithm

The Verlet algorithm [229], is derived by writing;

$$r(t + \partial t) = r(t) + v(t)\partial t + \frac{1}{2}a(t)\partial t^2 \quad \text{(Equation 5.17)}$$

and

$$r(t - \partial t) = r(t) - v(t)\partial t - \frac{1}{2}a(t)\partial t^2 \quad \text{(Equation 5.18)}$$

Summing Equation 5.17 and Equation 5.18, Equation 5.19 is obtained:

$$r(t + \partial t) = 2r(t) - r(t - \partial t)a(t)\partial t^2 \qquad \text{(Equation 5.19)}$$

Both the accelerations and positions at time t and time $t - dt$ are used by the Verlet algorithm to calculate new positions at time $t + dt$. Their is no explicit definition for velocities in the Verlet algorithm. The advantages with the Verlet algorithm are that; it is straightforward, and it requires a modest storage. However, it is of moderate precision.

5.2.2 The Leap-frog Algorithm

In the leap-frog algorithm, the position and velocity of a particle can be derived by writing:

$$r(t + \partial t) = r(t) + v\left(t + \frac{1}{2}\partial t\right)\partial t \qquad \text{(Equation 5.20)}$$

$$v\left(t + \frac{1}{2}\partial t\right) = v\left(t - \frac{1}{2}\partial t\right) + a(t)\partial t \qquad \text{(Equation 5.21)}$$

The velocities are first calculated at time $t + 1/2dt$; and thereafter used to calculate the positions, r, at time $t + dt$. The advantage of leap-frog algorithm is that the velocities are explicitly calculated. Its disadvantage is that all velocities are not calculated at the same

time as the positions. At time t, the velocities can be approximated by the relationship in Equation 5.22:

$$v(t) = \frac{1}{2}\left[v\left(t - \frac{1}{2}\partial t\right) + v\left(t + \frac{1}{2}\partial t\right)\right] \qquad \text{(Equation 5.22)}$$

5.2.3 Beeman's Algorithm

The Beeman's algorithm is closely related to the Verlet algorithm and it can be shown to be given by the following expressions:

$$r(t + \partial t) = r(t) + v(t)\partial t + \frac{2}{3}a(t)\partial t^2 - \frac{1}{6}a(t - \partial t)\partial t^2 \qquad \text{(Equation 5.25)}$$

$$v(t + \partial t) = v(t) + v(t)\partial t + \frac{1}{3}a(t)\partial t + \frac{5}{6}a(t)\partial t - \frac{1}{6}a(t - \partial t)\partial t \qquad \text{(Equation 5.26)}$$

Compared with the Verlet algorithm, this algorithm provides a better energy conservation and more accurate expression for the velocities. However, the algorithm expression is more complex and therefore, more expensive to calculate.

5.2.4 The Velocity Verlet Algorithm

This algorithm [230], can be shown to be given by the following expressions:

$$r(t + \partial t) = r(t) + v(t)\partial t + \frac{1}{2}a(t)\partial t^2 \qquad \text{(Equation 5.23)}$$

$$v(t + \partial t) = vt + \frac{1}{2}\left[a(t) + a(t + \partial t)\right]\partial t \qquad \text{(Equation 5.24)}$$

The velocity Verlet algorithm is regarded as the most complete form of Verlet algorithm because without any compromise on precision, it provides both the atomic positions and velocities at the same instant of time, thereby requiring less computer memory.

All MD integrating algorithms will typical evolves through three distinct stages. These are the *initialization, equilibration and production* stages. The positions and velocities of atoms are defined at the initialization stage, while the dynamics of the interacting atoms is developed at the equilibration stage. This stage usually takes some time for proper system updating. Past history of the system is lost after equilibration. The production stage is used to generate the space-phase trajectory, from which equilibrium material properties are calculated. An example of integrating algorithm is shown in Figure 5.1.

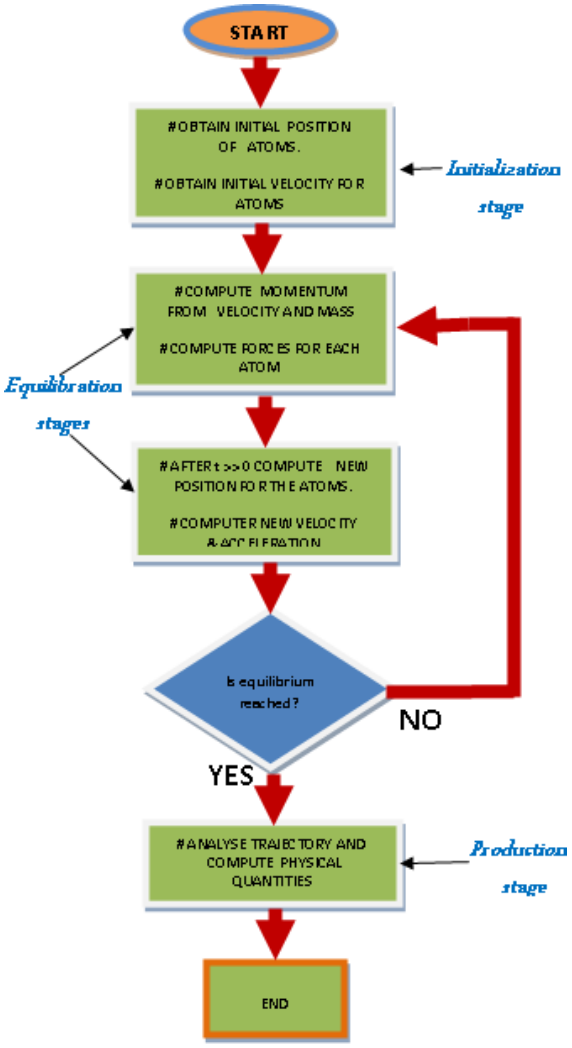

Figure 5.1: Flowchart for implementing MD calculations

5.3 Ensembles and boundary conditions

Due to the huge size of molecular systems, time independent statistical averages are often introduced to connect the macroscopic system to the microscopic system. This is achieved by defining the thermodynamic state of the system with a small set of parameters, for example, the pressure, P, the temperature, T, and the number of particles, N. Other thermodynamic properties can then be derived from the equations of state and other fundamental

thermodynamic equations.

The microscopic state of a system is defined by the atomic positions and their momenta. In MD, an *ensemble* is a collection of all systems with different microscopic states but identical macroscopic or thermodynamic state. Different types of ensembles [231] with their characteristics are listed as follows:

1. Microcanonical ensemble (NVE) : The thermodynamic state [232], is characterized by a fixed number of atoms (N), volume (V) and a fixed energy (E). This corresponds to an isolated system.
2. Canonical Ensemble (NVT): This is a system in which the thermodynamic state is characterized by fixed number of atoms (N), volume (V) and temperature (T).
3. Isobaric-Isothermal Ensemble (NPT): The NPT ensemble [233, 234, 235, 236] is characterized by a fixed number of atoms (N), a fixed pressure (P) and a fixed temperature (T)
4. Grand canonical Ensemble (μVT): The thermodynamic state for this ensemble is characterized by a fixed chemical potential (μ), a fixed volume (V), and a fixed temperature (T).

For bulk phases, the trajectory needed to evaluate the macroscopic properties is easier to evaluate when the sample is subjected to boundary conditions. Boundary conditions are applied to mimic the presence of an infinite bulk, surrounding the N atoms in a system. For a periodic system containing N atoms and confined to volume V, application of boundary

condition allows a small portion of the cell (called primary cell) to be treated. The bulk material, which is considered a replica of the primary cell is then sampled in all directions [227, 231]. To obtain an accurate result, it is important that a molecular dynamics simulation is allowed to run for sufficiently long time so that enough representative of the bulk system is sampled.

5.4 Interatomic Potentials

The interactions between atoms and molecules in a material is either of covalent or non-covalent type [237, 238]. Covalent interaction occurs when one or more pairs of electron are shared. As a result, overlapping of partially occupied orbitals takes place. Conversely, attraction in non-covalent interactions are from the electrical properties of the atoms or molecules. Covalent interactions are much stronger than the non-covalent types, and are of short range, while the non-covalent interactions are of longer range. The number of valence electron on an atom determines the number of covalent bonds it can form. Most frequently, covalent bonds are more favored between atoms of similar electronegativity. For successful calculations, MD simulations adopt physically correct interatomic potential models. Interatomic models are designed to give statistically-averaged representations for macroscopic systems consisting of many particles. This approach has proved effective as interactions between atoms are adequately described and the calculation can handle thousands to millions of atoms. A good knowledge of the nature and magnitude of an interatomic and intermolecular interactions is

important for the correct prediction of material properties.

In metallic systems, cohesion are due mainly to metallic bonding [239]. Any system with many electrons is a many-body interaction, which can only be described by many-body effects. For this reason, the embedded atom model (EAM) potentials [240] have been developed and used to study elemental metals and their alloys [241, 242, 243]. Other variants of EAM includes the Glue Model potentials [244], the Finis-Sinclair potential for the bcc elemental metals [228], which have also been developed for noble metals [245], the Sutton-Chen (S-C) potentials [246] for the ten specified fcc elemental metals, and the Rafii-Tabar and Sutton potentials for the fcc random binary alloys [247].

According to the EAM model [240], the total energy of an elemental system can be written as:

$$\Phi^{EAM} = \sum_i F_i[\rho_{h,i}] + \frac{1}{2}\sum_i \sum_{j \pm i} \phi_{ij}(r_{ij}) \qquad \text{(Equation 5.27)}$$

where $\rho_{h,i}$ is the electron density of the host at the site of atom i, $F_i[\rho]$ is the energy needed to embed the atom i into the background electron density ρ, and ϕ_{ij} is a pairwise central potential between atoms j and i, separated by a distance r_{ij}, which represents the core-core repulsive electrostatic interactions. $F_i[\rho]$ is a universal functional [248].

The host electron density is obtained from linear superposition of the individual contributions and is given by:

$$\rho_{h,i} = \sum_{ji\not/} \rho_j^*(r_{ij}) \qquad \text{(Equation 5.28)}$$

where ρ_j^* is the electron density of atom j relative to interatomic separation.

For ordered binary alloys, the EAM potentials can be written as [249]:

$$\Phi_{Alloy}^{EAM} = \sum_{ti} F_i[\rho_{h,i}] + \frac{1}{2} \sum_i \sum_{j \neq i} \phi_{ti.tj}(r_{ij}) \qquad \text{(Equation 5.29)}$$

where ϕ depends on the type of atom t_i and t_j.

The host electron density then becomes:

$$\rho_{h,i} = \sum_{j \neq i} \rho_{tj}^*(r_{ij}) \qquad \text{(Equation 5.30)}$$

where each term in the sum depends on the type of neighbor atom j.

5.4.1 Many-Body Rafii-Tabar and Sutton Long-Range Alloy Potentials

The Rafii-Tabar and Sutton (RTS) potentials [247, 250] are another variant of the Sutton-Chen (SC) potentials, which model the energetics of fcc binary metallic alloys. RTS is otherwise called the quantum Sutton-Chen potentials (Q-SC). Quantum effects are catered for in its parameterization. It provides a more accurate calculation of temperature dependent physical properties than the ordinary S-C potentials [251].

The Q-SC potential is given by:

$$\Phi^{RTS} = \frac{1}{2}\sum_{i}\sum_{i\neq j} P_i^* P_j^* V^{AA}(r_{ij}) + (1-P_i^*)(1-P_j^*)V^{BB}(r_{ij}) +$$

$$[P_i^*(1-P_j^*) + P_j^*(1-P_i^*)]V^{AB}(r_{ij}) - d^{AA}\sum_{i} P_i^*[\sum_{j\neq i} P_j^*\Phi^{AA}(r_{ij}) +$$

$$(1-P_j^*)\Phi^{AB}(r_{ij})]^{\frac{1}{2}} - d^{BB}\sum_{i}(1-P_i^*)[\sum_{j\neq i}(1-P_j^*)\Phi^{BB}(r_{ij}) + P_j^*\Phi^{AB}(r_{ij})]^{\frac{1}{2}} \quad \text{(Equation 5.31)}$$

the site occupancy operator, P_i^* is defined as

$$P_i^* = 1$$

when site i is occupied by an A atom, and defined as:

$$P_i^* = 0$$

when site i is occupied by a B atom.

The functions $V^{AA}, V^{BB}, V^{AB}, \Phi^{AA}, \Phi^{BB}, \Phi^{AB}$ are defined as:

$$V^{AA}(r) = \varepsilon^{AA}[a^{AA}/r]^{n^{AA}} \quad \text{(Equation 5.32)}$$

$$V^{BB}(r) = \varepsilon^{BB}[a^{BB}/r]^{n^{BB}} \quad \text{(Equation 5.33)}$$

$$V^{AB}(r) = \varepsilon^{AB}[a^{AB}/r]^{n^{AB}} \quad \text{(Equation 5.34)}$$

$$\Phi^{AA}(r) = [a^{AA}/r]^{m^{AA}} \quad \text{(Equation 5.35)}$$

$$\Phi^{BB}(r) = [a^{BB}/r]^{m^{BB}} \quad \text{(Equation 5.36)}$$

$$\Phi^{AB}(r) = [a^{AB}/r]^{m^{AB}} \quad \text{(Equation 5.37)}$$

The constants d^{AA} and d^{BB} are further defined as:

$$d^{AA} = \varepsilon^{AA} c^{AA} \qquad \text{(Equation 5.38)}$$

$$d^{BB} = \varepsilon^{BB} c^{BB} \qquad \text{(Equation 5.39)}$$

where ε^{AA}, c^{AA}, a^{AA} , m^{AA} and n^{AA} are equated with the parameter ε, c, a, m and n of the pure A metal as tabulated by Sutton and Chen [246]. Similarly, ε^{BB}, c^{BB}, a^{BB}, m^{BB} and n^{BB} are equated with the parameter ε, c, a, m and n of the pure B metal.

Expressing the functions V^{AB} and Φ^{AB} as:

$$V^{AB} = (V^{AA} V^{BB})^{\frac{1}{2}} \qquad \text{(Equation 5.40)}$$

$$\Phi^{AB} = (\Phi^{AA} \Phi^{BB})^{\frac{1}{2}} \qquad \text{(Equation 5.41)}$$

Thus for a binary A-B alloy systems, the parameters ϵ^{AB}, c^{AB}, m^{AB}, n^{AB} and a^{AB} are obtained by arithmetic and geometric means as:

$$\epsilon^{AB} = \left(\epsilon^A \epsilon^B\right)^{\frac{1}{2}}, \qquad \text{(Equation 5.42)}$$

$$m^{AB} = \frac{m^A + m^B}{2}, \qquad \text{(Equation 5.43)}$$

$$n^{AB} = \frac{n^A + n^B}{2}, \qquad \text{(Equation 5.44)}$$

$$a^{AB} = \left(a^A a^B\right)^{\frac{1}{2}} \qquad \text{(Equation 5.45)}$$

The procedure for deriving the potential for osmium and ruthenium made use of the Sutton-Chen form of EAM. For pure metals, the total potential energy in the Sutton-Chen form of EAM is given as [246]:

$$\Phi_l^{SC} = \varepsilon[\frac{1}{2}\sum_i \sum_{j \neq i} \phi_{rep}(r_{ij}) - c\sum_i (\rho_i)^{\frac{1}{2}}] \qquad \text{(Equation 5.46)}$$

where $\phi_{rep}(r_{ij})$ is a pair potential accounting for repulsion between i and j atomic cores and ρ_i is a local density accounting for the cohesion associated with i. $\phi_{rep}(r_{ij})$ is given by:

$$\phi_{rep}(r_{ij}) = (\frac{a}{r_{ij}})^n \qquad \text{(Equation 5.47)}$$

and

$$\rho_i = \sum_{j \neq i} (\frac{a}{r_{ij}})^m \qquad \text{(Equation 5.48)}$$

In Equation 5.46 - Equation 5.48, c is a dimensionless quantity, r_{ij} is the spacing between atoms i and j, ε is a quantity with the unit of energy, a is the lattice parameter and m and n are positive integers with $n > m$.

The potentials for Os and Ru was deduced from the density functional calculations wherein m and n completely defines Equation 5.46. The value of c was fixed by the equilibrium condition for each crystal structure [246].

The potential parameters for platinum, iridium, palladium and rhodium were obtained from [252], while those for ruthenium and osmium were derived for the first time in this thesis, and they are given in Table 5.1.

The newly derived S-C type potential was used to calculate the bulk modulus and melting points of osmium and ruthenium. To ascertain the correctness of the newly derived potentials, results based on it was compared with those obtained from existing S-C potentials for the other PGMs. All calculations were implemented with the DL-POLY computer code [253].

Table 5.1: Sutton-Chen potential parameters used in present work.

Metal	n	m	ϵ (eV)	c	a($\AA$)
Pt	11	7	9.7894E-3	71.336	3.9163
Rh	13	5	2.4612E-3	305.499	3.7984
Pd	12	6	3.2864E-3	148.205	3.8813
Ir	13	6	3.7674E-3	224.815	3.8344
Os	13	6	3.8665E-3	230.728	3.8640
Ru	14	5	2.6060E-3	323.468	3.8330

5.4.2 Radial Distribution Function

The **R**adial **D**istribution **F**unction (RDF) (or pair correlation function), describes on average, how atoms in a system are radially packed (see Fig. 5.2) around each other. In simplest terms, it is a measure of the probability of finding a particle at a distance away from a given reference particle, relative to that for an ideal gas. The RDF is an effective way of describing the average structure of disordered molecular systems [254]. The RDF can be deduced experimentally from x-ray or neutron diffraction studies, thus providing a direct way for comparing experimental and simulation results. In conjunction with the interatomic pair potential function, RDF can be accurately used to calculate the internal energy of a system [254].

Mathematically, the formula for RDF is:

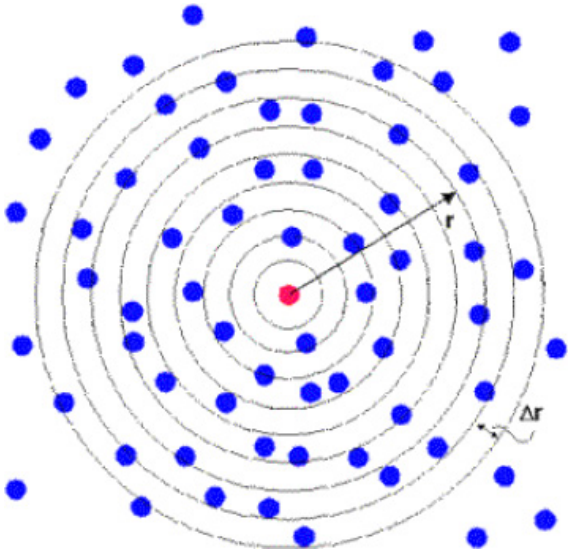

Figure 5.2: Schematic diagram showing a heavy element, with nucleus (red) and electrons (blue) to explain the RDF concept. Adapted from [254].

$$g(r) = \frac{n(r)}{\rho 4\pi r^2 \triangle r} \qquad \text{(Equation 5.49)}$$

where $g(r)$ is the RDF, $n(r)$ is the mean number of atoms in a shell of width $\triangle r$ at distance r, ρ is the mean atom density.

In a typical RDF plot (see Fig. 5.3), the RDF is usually plotted against the interatomic separation r. A number of important features can be obtained from an RDF plot. The RDF is zero at short separations (small r) and this indicates the effective width of the atoms, since they cannot approach any more closely. A number of peaks are also observed, which indicates the packing of the atoms around each other in 'shells' of neighbors. A high degree of ordering is indicated when peaks are observed at long ranges. The peaks are usually broad at high

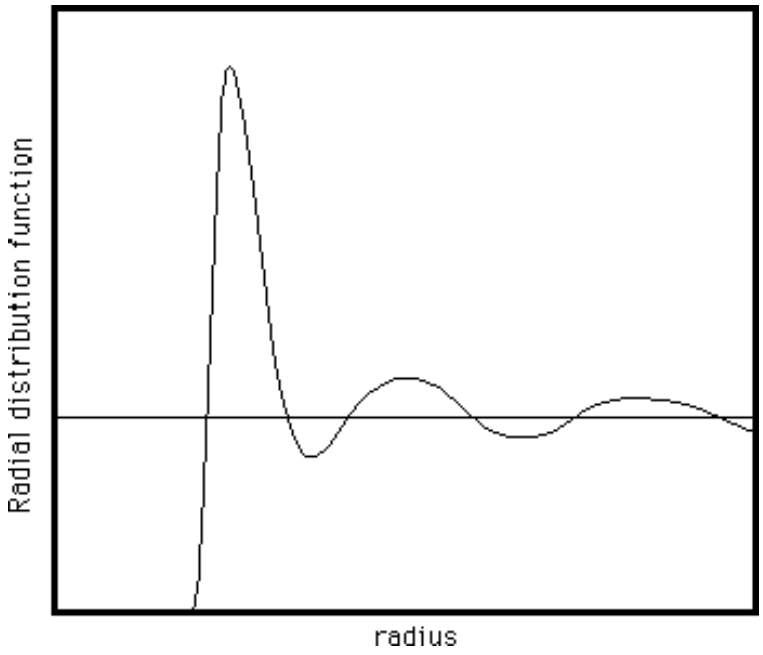

Figure 5.3: Sample plot to illustrate the RDF concept. Adapted from [254].

temperature, indicating thermal motion, while at low temperature they are sharp. The peaks are usually sharp in crystalline materials, due to their atoms being strongly confined in their positions. Every RDF tends to a value of 1 at very long range. This happens because the RDF describes the average density at this range [254].

In pure metals, melting takes place at a fixed, well defined point. In an alloy, melting does not take place at a fixed temperature, but over a range of temperatures. In MD, melting temperature can be obtained from phase transition phenomena. The phase transition from the solid state into liquid can be determined using three approaches:

(1) a jump on the total energy vs temperature plot,

(2) drastic increase in the diffusion coefficient and

(3) a change in the shape of the radial distribution function (RDF).

5.5 The DL-POLY Package

DL-POLY is a molecular dynamics simulation package developed at Daresbury Laboratory. The DL-POLY computer code is able to simulate ten-of-thousands of atoms, in most popular MD ensembles and boundary conditions. There are basically two forms of the code: DL-POLY 2 [255] and DL-POLY 4 [247]. The DL-POLY 4 is a recent version of DL-POLY 2 and it can handle more atoms than DL-POLY 2. For scientific research of non-commercial nature, both versions are issued free under license to individuals or academic institutions.

The DL-POLY 2 is fully compatible to the DL-POLY 4. The DL-POLY package is designed to accommodate many force fields. The package is also easier to adapt to other user specific force fields. For calculation efficiencies, DL-POLY integration techniques were more of the Leapfrog Verlet (LFV) and Velocity Verlet (VV) [256].

5.6 Results from MD calculations

The elastic properties of a material varies with temperature. In materials for high temperature application, knowledge of the thermoelastic properties is vital for describing the mechanical response of such materials to fracture toughness, stress etc. In this section, the focus is on the temperature dependence of bulk moduli and the melting point of the fcc structured noble metals, nickel and their associated X_3Al compounds. All intramolecular

forces are modeled with the Sutton-Chen (S-C) potentials. The bulk modulus and the melting points of the metals are evaluated to compare the validity of osmium and ruthenium potentials generated for the first time in this work with existing S-C potentials for the other PGMs available in the literature.

Calculation Method

To study melting, a super-cell containing 6912 atoms was generated and simulated with the cubic periodic boundary condition. The relaxation time was fixed at 0.1ps with the constant temperature-pressure (NPT) Berendsen ensemble [236]. The equations of motion for interacting atoms was solved with the Velocity Verlet (VV) algorithm at a time-step of 10^{-15}s. Each system was simulated at temperature increments of 100K and latter reduced to 50K to limit fluctuations near the melting points. All calculations were carried out for 100000-steps of equilibration, with a production time of 1ps. The melting temperature for each compound was determined by analyzing their diffusion coefficient (DCO), the radial distribution function (RDF) and lattice atom distribution pattern at different temperatures.

A smaller super-cell, consisting of 3456 atoms was used for structure relaxations and bulk modulus calculations. Each cell was simulated first with the NPT ensemble to obtain the equilibrium volume, after which it was switched to the NVT ensemble [235] to distort the cell and obtain change in energy. To obtain the lattice parameters and the bulk moduli, a

least-square fit of the energy-volume data was done using the Birch-Murnaghan equation of state.

5.6.1 Bulk modulus and Melting of X_3Al

The result of the bulk modulus and melting points obtained with the Sutton-Chen potential for nickel and some noble metals are listed in Table 5.2. Also listed are available experimental data. The bulk modulus obtained for osmium from the MD calculation lied between values given by available experimental data, suggesting that the S-C parameters derived in this work is valid and suitable for simulation. A high bulk modulus coincided with high MD derived melting temperatures. However, experimental melting points were over-predicted by the MD calculation. The higher the experimental melting point of an element, the higher the over-prediction. Defects is one of the known factors that promote melting, therefore, the observed over-prediction may have been influenced by different defect types.

For $L1_2$-X_3Al compounds, the results of the lattice parameter, density and bulk modulus from 1K - 2000K are shown in Table 5.3. The analysis of the bulk modulus (Figure 5.3), shows that Os_3Al has the highest bulk modulus, followed by Ir_3Al and Pt_3Al. However, the trends in Pt_3Al and Ir_3Al was almost constant across the temperature regime, suggesting that $L1_2$-Pt_3Al and $L1_2$-Ir_3Al should have better strength than the other compounds. The strength of the $L1_2$-X_3Al compounds were much better when compared with that of $L1_2$-Ni_3Al. As

Table 5.2: Calculated bulk modulus and melting temperature for nickel and some noble metals using the Sutton-Chen Potentials listed in Table 5.1. Experimental data are in curly brackets.

Metal	B (GPa)	MP (K)	Refs.
Ni	237, {180}	1850, {1728}	[78, 83]
Pd	195, {180}	1950, {1828}	[78, 83]
Pt	387, {230}	2300, {2041}	[78, 83]
Ir	422, {306, 320, 355}	3600, {2739}	[29, 257, 258]
Rh	398, {380}	2850, {2237}	[78, 83]
Ru	322, {220}	3200, {2607}	[78, 83]
Os	428, {395±15, 411±6, 443, 462}	3700, {3306}	[87, 259, 260]

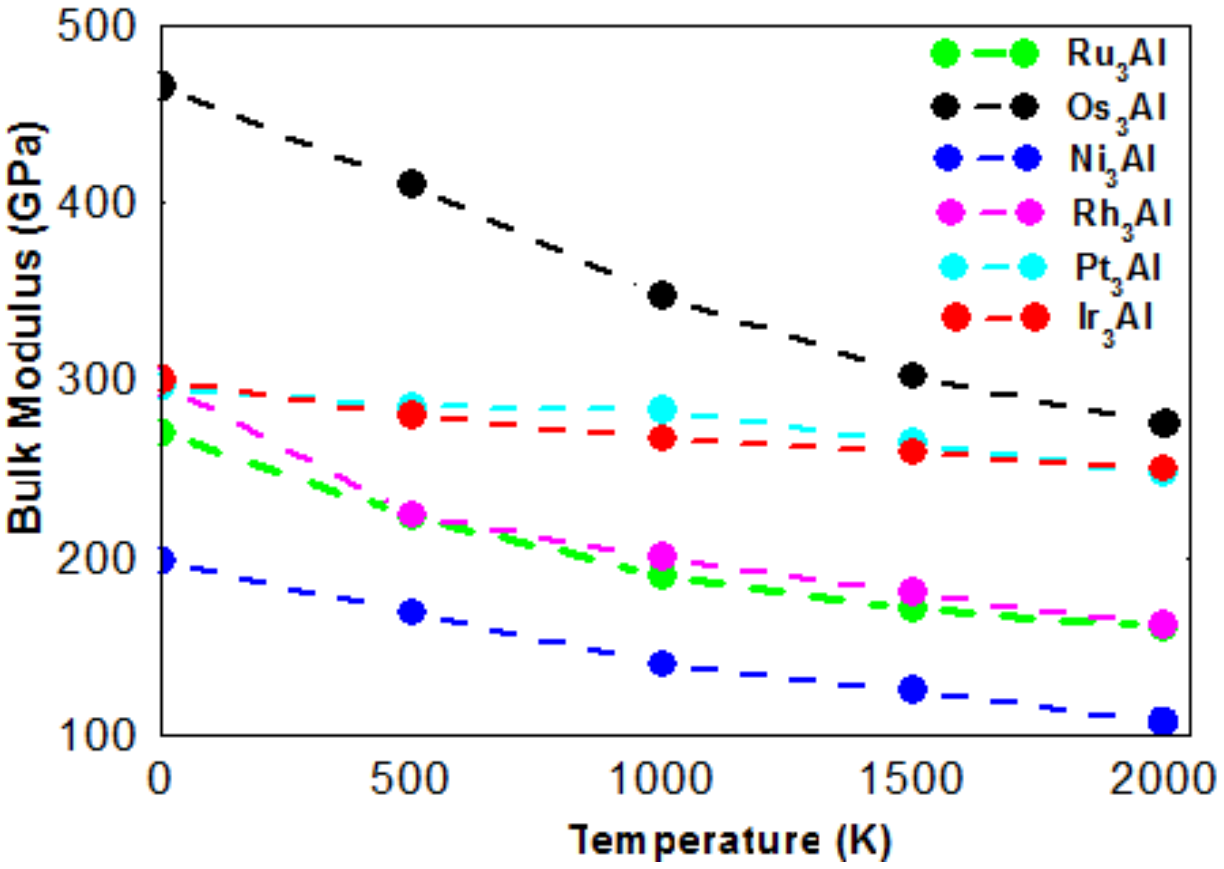

Figure 5.4: Molecular dynamics results for the bulk modulus for $L1_2$-X_3Al from 1K to 2000K.

would be expected, the density is lowest in Rh_3Al compound.

5.6.2 Melting in X_3Al alloys

The result of diffusion coefficient (DCO) analysis, radial distribution function (RDF) and lattice atom distribution as a function of temperature for $L1_2$-Pt_3Al are shown in Figure 5.4 (a - c) . On the DCO plot (Fig. 5.4(a)), the melting point was identified by monitoring where a discontinuity or jump occurred, and this occurred between 1890K and 1900K. A drastic

Table 5.3: Calculated lattice parameter, density and bulk modulus at 1K, 500K, 1000K, 1500K and 2000K of some X_3Al alloys using the Sutton-Chen potentials given in Table 5.1.

Material	Properties	1K	500K	1000K	1500K	2000K
	a $(\mathring{A})$	3.672	3.723	3.767	3.808	3.845
Ni_3Al	B (GPa)	198	140	125	113	108
	$\rho(g.cm^{-3})$	4.36	4.26	4.20	3.70	3.66
	a $(\mathring{A})$	3.885	3.920	3.951	3.982	4.011
Pt_3Al	B (GPa)	296	285	283	265	247
	$\rho(g.cm^{-3})$	9.54	9.51	9.41	9.34	9.11
	a $(\mathring{A})$	3.852	3.887	3.918	3.948	3.976
Ir_3Al	B (GPa)	300	280	267	259	250
	$\rho(g.cm^{-3})$	9.63	9.44	9.30	9.20	9.11
	a $(\mathring{A})$	3.651	3.693	3.732	3.768	3.803
Rh_3Al	B (GPa)	298	224	200	180	162
	$\rho(g.cm^{-3})$	6.67	6.61	6.55	6.51	6.44
	a $(\mathring{A})$	3.972	4.014	4.052	4.087	4.120
Ru_3Al	B (GPa)	270	223	190	171	161
	$\rho(g.cm^{-3})$	4.84	4.76	4.70	4.66	4.62
	a $(\mathring{A})$	3.787	3.818	3.839	3.871	3.897
Os_3Al	B (GPa)	465	410	347	302	294
	$\rho(g.cm^{-3})$	10.09	9.93	9.52	9.29	9.18

change in the shape of the RDF (Fig. 5.4(b)) between 1890K and 1900K also identified the melting point, while the temperature where a change occurred in lattice ordering was used to identify the melting point on lattice atom distribution as a function of temperature plots (Fig. 5.4(c)). In the temperature-lattice ordering plots, initially at 1880K and 1890K, the cubic lattice has only slightly lost ordering, but at higher temperatures 1900K and 1960K, the ordering was completely lost, showing that the material has melted.

It was seen from the DCO that aluminium had a higher diffusion coefficient than platinum. Structurally, aluminum has a larger interatomic spacing than platinum, which would have naturally subjected it to easier polarization. Additionally, elements with higher atomic mass are expected to have higher melting points. This observation is not surprising, as the melting of a substance depends both on the single-molecule properties and their spatial arrangement (packing).

From Figure 5.5, the melting point of $L1_2$-Rh_3Al according to the DCO, the RDF and the atom distribution plots was between 2590K and 2600K. This result also showed aluminum having higher diffusion coefficient than rhodium.

The various results in Figure 5.6, showed that $L1_2$-Pd_3Al melting point was between 1390K and 1400K. The DCO result also showed aluminum having higher diffusion coefficient than palladium.

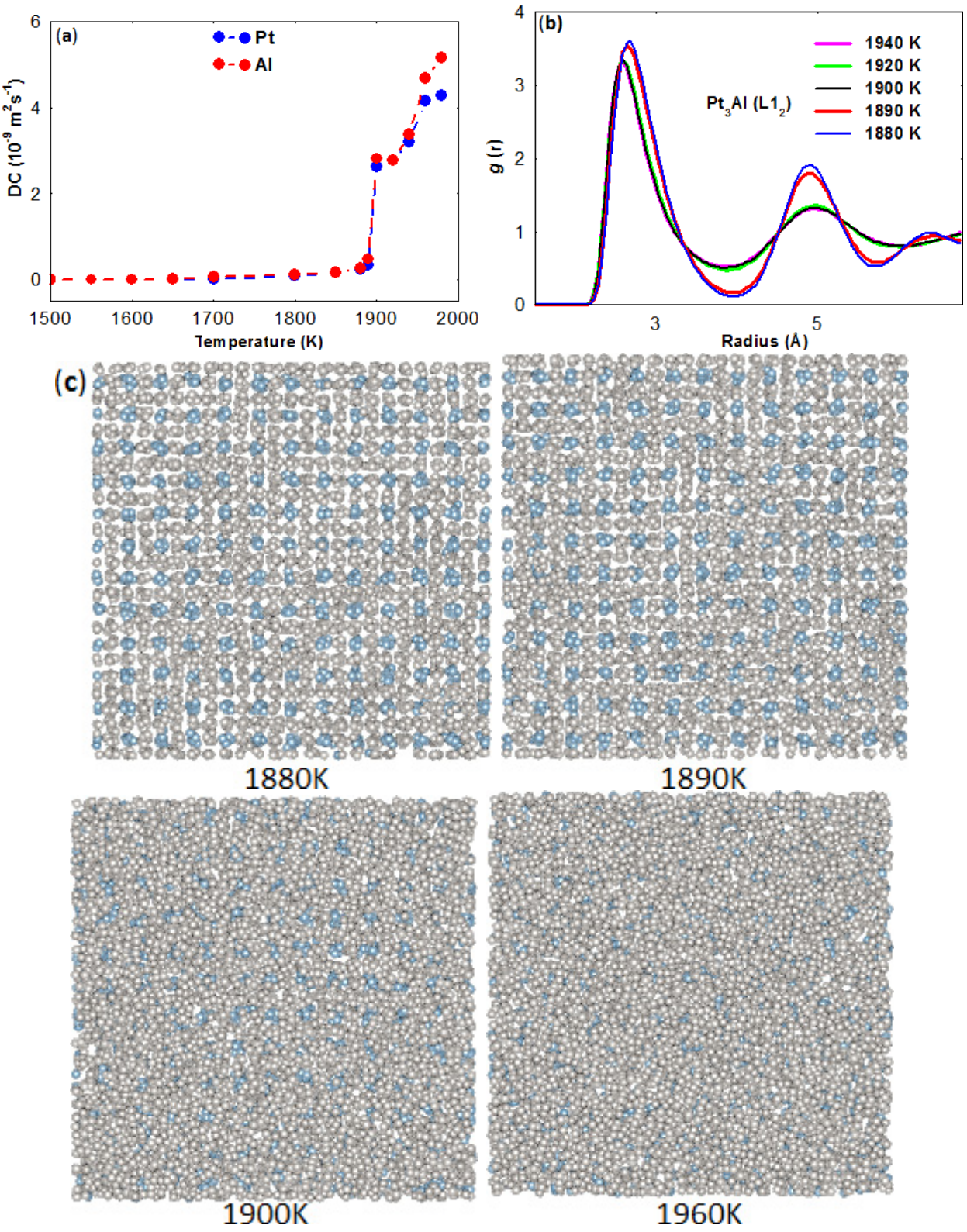

Figure 5.5: Molecular dynamics results for (a) the diffusion constant, (b) radial distribution function and (c) atom distribution near the melting point at 1880K, 1890K, 1900K and 1960K in $L1_2$-Pt_3Al.

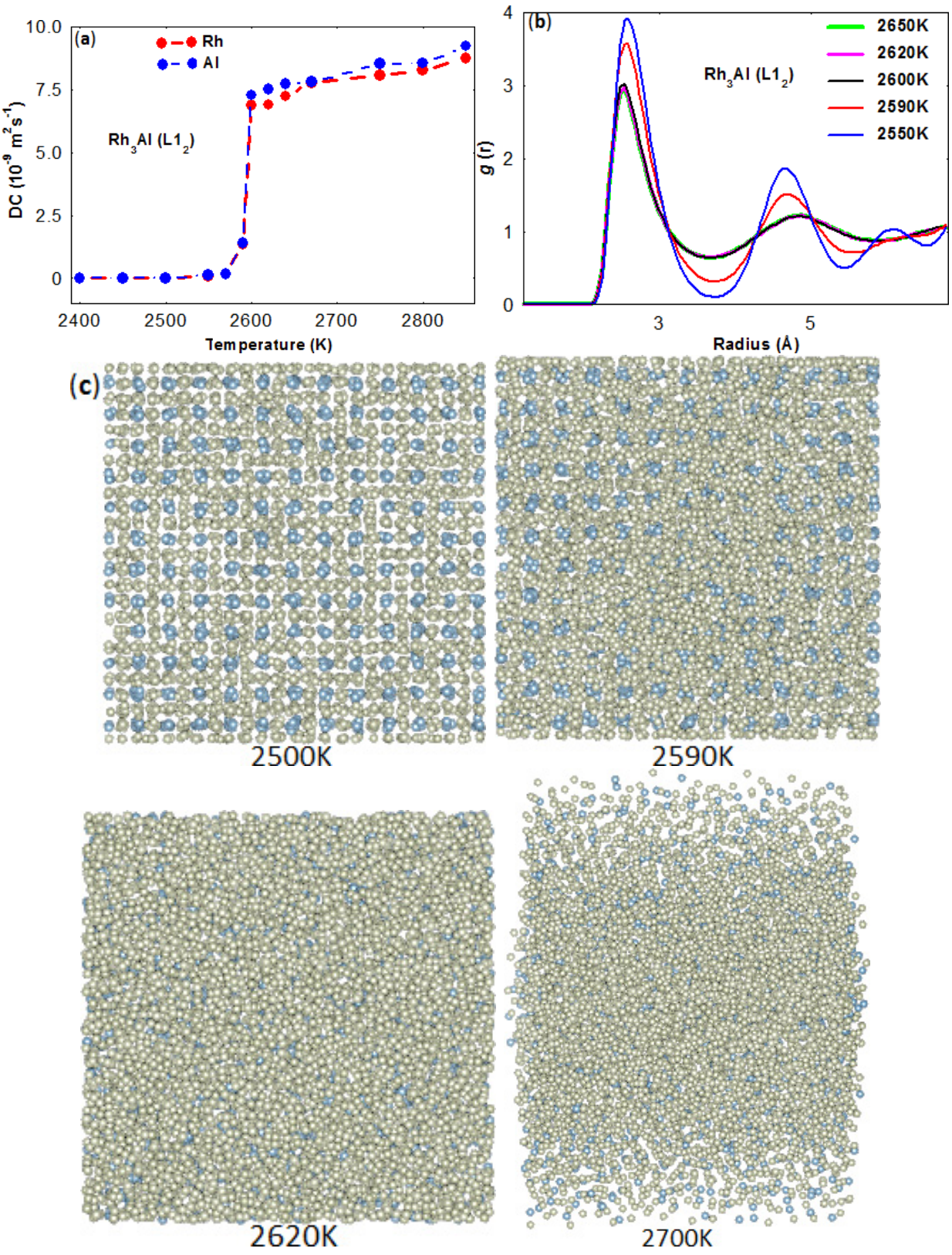

Figure 5.6: Molecular dynamics results for (a) the diffusion constant, (b) radial distribution function and (c) atom distribution near the melting point at 2500K, 2590K, 2620K and 2700K in $L1_2$-Rh_3Al.

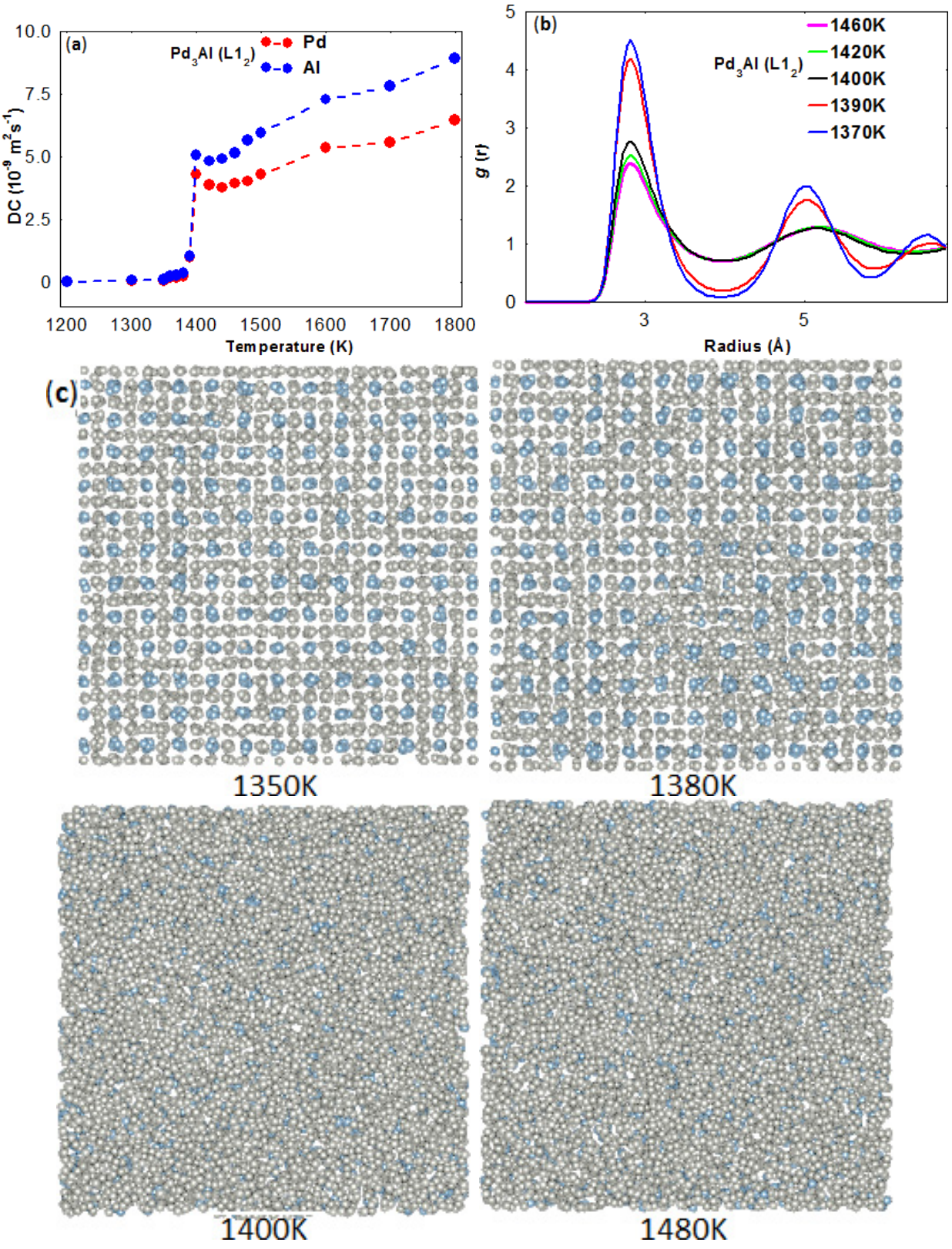

Figure 5.7: Molecular dynamics results for (a) the diffusion constant, (b) radial distribution function and (c) atom distribution near the melting point at 1350K, 1380K, 1400K and 1480K in $L1_2$-Pd_3Al.

All the three results in Figure 5.7 agreed and showed that $L1_2$-Ir_3Al melted between 2720 & 2730K. In $L1_2$-Os_3Al compound, melting was observed between 3000 & 3100K. This is shown by the DCO, RDF and atom distribution as a function of temperature in Figure 5.8.

In $L1_2$-Ru_3Al compound, melting was observed between 2700K and 2800K. This is shown by the DCO, RDF and atom distribution as a function of temperature in Figure 5.9.

5.7 Predicted melting temperatures: comparison of ab-inito, MD and experimental results

From the results in Table 5.4, experimental melting points were over-predicted by both MD and ab initio calculations. Although, the trend from the two approaches were similar and consistent. The higher the experimental melting point of an element, the higher the ab-inito and MD melting points. The over-prediction may have been due to factors that promote melting, such as defects. For Pt_3Al, the MD calculated melting point was just 3.88% more than experimental value.

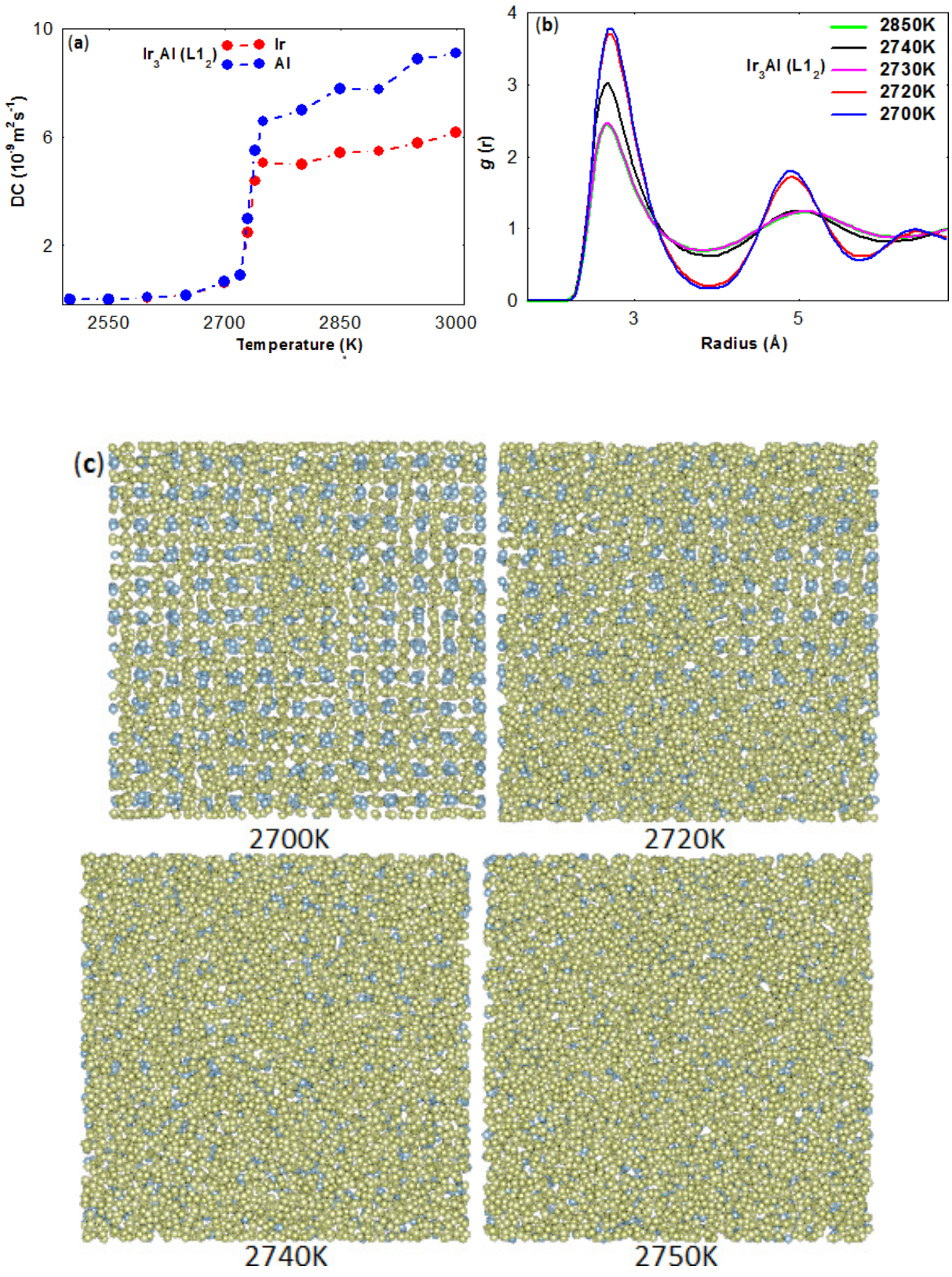

Figure 5.8: Molecular dynamics results for (a) the diffusion constant, (b) radial distribution function and (c) atom distribution near the melting point at 2700K, 2720K, 2740K and 2750K in $L1_2$-Ir_3Al.

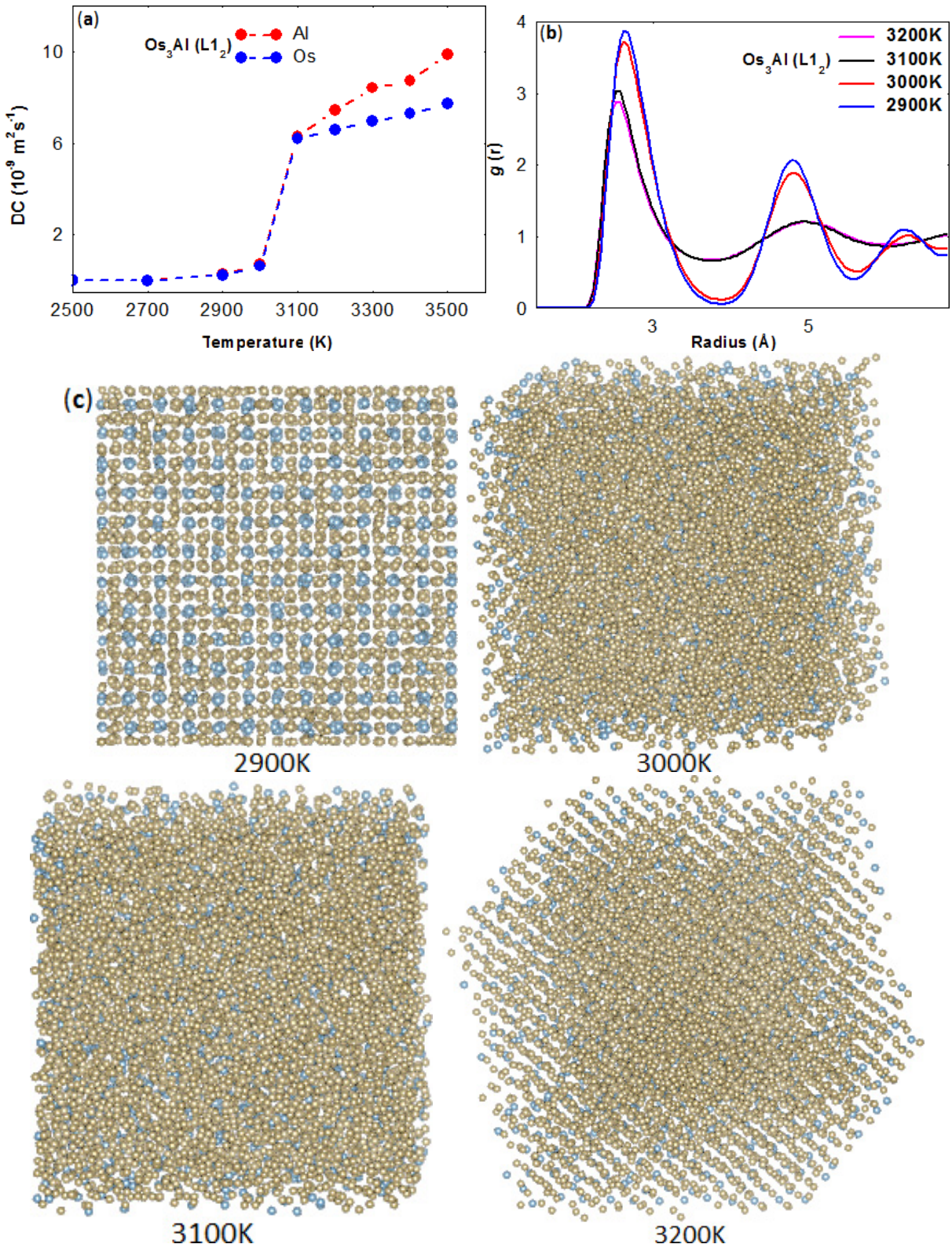

Figure 5.9: Molecular dynamics results for (a) the diffusion constant, (b) radial distribution function and (c) atom distribution near the melting point at 2900K, 3000K, 3100K and 3200K in $L1_2$-Os_3Al .

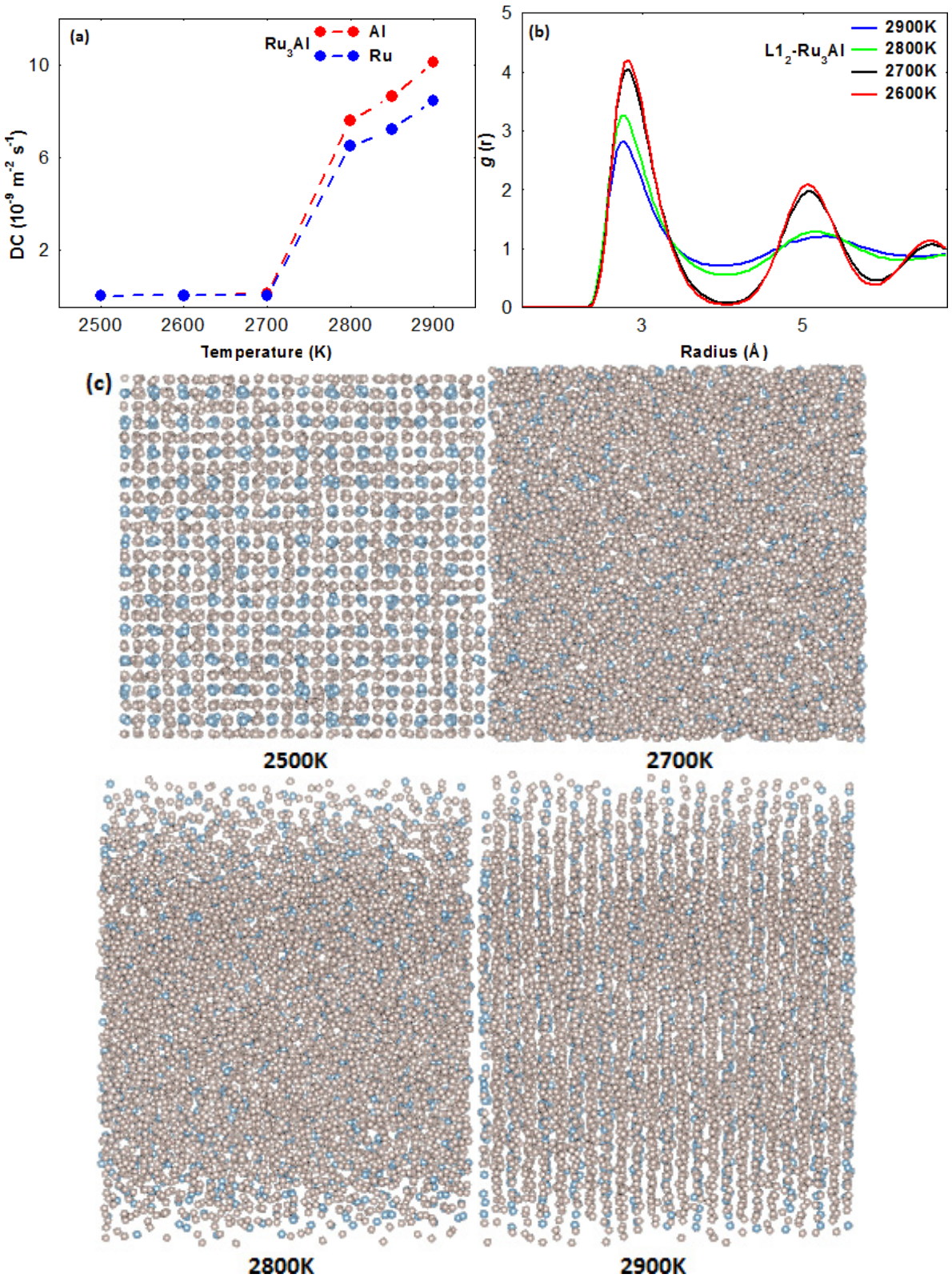

Figure 5.10: Molecular dynamics results for (a) the diffusion constant, (b) radial distribution function and (c) atom distribution near the melting point at 2500K, 2700K, 2800K and 2900K in $L1_2$-Ru_3Al.

Table 5.4: Calculated melting temperatures, *ab initio* (AI) and MD in X_3Al alloys.

Mater.	AI (K)	MD (K)	Expt. (K)
Ni	**2213±300**	**1850±50**	**1728**
Pd	**1747±300**	**1950±50**	**1828**
Pt	**2328±300**	**2300±50**	**2041**
Ir	**3914±300**	**3600±50**	**2739**
Rh	**2927±300**	**2850±50**	**2237**
Ru	**3037±300**	**3200±50**	**2607**
Os	**3903±300**	**3700±50**	**3306**
Pt_3Al	**2486±300**	**1900±50**	**1829**
Ir_3Al	**2846±300**	**2740±50**	**-**
Os_3Al	**2957±300**	**3100±50**	**-**
Rh_3Al	**2155±300**	**2600±50**	**-**
Pd_3Al	**1566±300**	**1400±50**	**-**
Ru_3Al	**1835±300**	**2700±50**	**-**

Experimental data are from Refs [78, 83, 87, 259, 260]

5.8 Summary

When the result in Table 4.2 (ab initio) is combined with that in Figure 5.3 (MD), the most promising compounds are Pt_3Al and Ir_3Al. These compounds had higher melting/mechanical properties compared with Ni_3Al and are predicted to maintain their mechanical properties over a wide temperature range (see Fig. 5.3).

Chapter 6

Other X_3B cubic intermetallic compounds

6.1 Introduction

The compounds discussed in previous sections were those formed between the noble metals and aluminium. A survey of alloy phase diagram databases [219], indicated that other elements such as scandium, zirconium and hafnium will also form solid solution with most noble metals. The use of scandium, zirconium and hafnium as an alloying element is of interest due to their many potentials. One of the basic scientific interest is to improve the properties that can be achieved by the addition. Scandium is a silvery white metal and the eighth most abundant rare element on earth. There are no known resources that are explorable for Sc. It is extracted from the earth's crust and as a by-products from processing of ores of other

metals such as W, Sn, U and Al [82]. Scandium is a light metal, and it has the capability to improve the strength of aluminum alloys by almost 50% [261]. The density of scandium is approx. 3 g.cm^{-3} with high melting point (1813K).

Due to its ability to withstand incredible forces, it has been used as guiding fins on missiles. Its addition into aircraft materials has become highly advantageous, giving them incredible weight, maneuverability and range advantages [261]. Although, the global yearly demand for metallic Sc is very small and its commercial use is still scanty [262] . However, the various attractive properties of scandium qualifies it as an alloying element in lightweight high temperature applications.

In nature, hafnium is always found associated with zirconium in minerals such as zircon and baddeleyite [263]. Except the inert gases [264], the chemical similarity between hafnium and zirconium is more pronounced than any other two elements in the periodic table. Due to similarity in their chemistry, the separation of hafnium and zirconium is extremely difficult. Hafnium and zirconium will form intermetallic compounds with most metallic elements, except the alkali metals and some alkaline earth metals [264]. Very often, Hafnium and zirconium are considered for the same applications due to their very similar physical and chemical characteristics. Other than the higher transition temperatures ($\alpha \rightarrow \beta$) for hafnium [264], the only other property showing a major difference between them is the density.

Due to its corrosion resistance and high cross-section for neutron absorption [265], Hafnium

is widely used for the design of the safety and control mechanisms in nuclear reactors. Future advanced reactors is believed [266] will use more of hafnium plated nuclear fuel rods. Under extreme conditions, the strength of niobium, nickel, titanium, tungsten, molybdenum and tantalum alloys were found improved with hafnium addition [265, 267]. Due to their bio-compatibility and corrosion resistance, they are used to manufacture medical implants and devices [268]. Good mechanical properties, high temperature martensitic transformations and shape memory behavior had been observed [269] in alloys comprising nickel-titanium-hafnium. Some intermetallic compounds of hafnium and cobalt, iron, platinum and palladium have shown potential as materials for hydrogen storage [270].

While available information [218, 219] showed that the $L1_2$ phase had been reported in Pt_3Sc, Ir_3Sc, Ir_3Zr, Ir_3Hf, Rh_3Sc, Rh_3Zr, Rh_3Hf, Pd_3Sc and Ru_3Sc, some other information gives conflicting report regarding the structure of other compounds [271, 272, 273, 274, 275]. For example, both the $L1_2$ and $D0_{24}$ structure have been reported in Pt_3Zr, Pt_3Hf, Pd_3Zr and Pd_3Hf. The intention of this chapter is to use various density functional schemes to calculate the heat of formation, elastic moduli, Debye temperature, melting point and the electronic structure of noble metal compounds in the stoichiometry X_3B (where B = Sc, Hf, Zr). These calculations are to provide clarification where necessary on compounds with competing structures.

6.2 Calculation Methods and Results

For compounds with cubic structures, calculation methods were similar to the one described in section 4.1. For other structures, the gamma centered scheme was used in the sampling of the Brillouin zone. Table 6.1, shows the sets of data obtained from the *ab initio* calculations. Again, the elastic stiffness coefficients (c_{11}, c_{12} & c_{44}) satisfied the generalized mechanical stability criteria (Equation 3.35) for the cubic structures.

6.2.1 Heats of formation and thermodynamic stability

For stable and high-performance alloys, the heat of formation ($\triangle H_f$) is expected to be negative. The more negative $\triangle H_f$ is, the more stable the structure. In addition, miscibility in a compound between competing species can be readily evaluated by $\triangle H_f$ results. Alloys with positive heat of formation are immiscible in thermodynamic equilibrium. The heats of formation in Figure 6.1 showed that $L1_2$-Os_3Sc is not energetically favored because it has positive heats of formation, and $\triangle H_f$ for $L1_2$-Ru_3Sc, $L1_2$-Ru_3Zr, $L1_2$-Os_3Hf and $L1_2$-Os_3Zr were so small that their thermodynamic formation in the $L1_2$ phase is unfavorable. All compounds with appreciable negative $\triangle H_f$ are predicted to be thermodynamically stable and should be possible to synthesize some by conventional means.

According to the $\triangle H_f$ calculations, $L1_2$-Pt_3Hf would be the most stable structure, followed

Table 6.1: Calculated lattice constant (a), elastic constants (c_{ij}), Moduli (B, G, E), Poisson's ratio (v), density (ρ^{cal}), Debye temperature (Θ_D/K), melting temperature (MT$\pm$300K) and heat of formation (H_f) in eV/at. All elastic constants and modulus are in GPa.

Alloy	a ($\AA$)	c_{11}	c_{12}	c_{44}	B	G	E	B/G	v	ρ^{cal}	P^C	Θ_D	MT	$\triangle H_f$
Ir_3Sc	3.949	358	198	164	252	139	352	1.81	0.27	12.79	35	281	2667	-0.60
Ir_3Zr	3.983	399	209	194	272	165	412	1.65	0.25	14.90	14	294	2910	-0.72
Ir_3Hf	3.968	410	214	204	279	172	429	1.62	0.24	19.70	10	281	2976	-0.80
Os_3Sc	3.954	327	234	105	265	86	233	3.07	0.35	12.63	129	234	2486	0.08
Os_3Zr	3.993	386	242	140	290	121	319	2.39	0.32	14.68	102	264	2837	-0.04
Os_3Hf	3.978	394	248	144	296	124	327	2.39	0.32	19.46	103	250	2879	-0.11
Pt_3Sc	4.011	292	162	115	205	103	265	1.99	0.29	12.36	47	246	2277	-1.05
Pt_3Zr	4.050	338	179	119	232	113	292	2.05	0.29	14.31	60	252	2552	-1.03
Pt_3Hf	4.035	351	181	126	238	120	309	1.98	0.28	18.88	55	243	2626	-1.09
Pd_3Sc	4.019	201	124	89	151	69	180	2.19	0.30	7.78	42	265	1735	-0.86
Pd_3Zr	4.035	257	140	94	179	86	222	2.09	0.29	10.01	49	281	2079	-0.81
Pd_3Hf	4.018	270	142	102	185	94	242	1.96	0.28	14.64	41	265	2151	-0.87
Rh_3Sc	3.935	258	159	119	192	96	246	2.01	0.29	8.06	40	310	2080	-0.61
Rh_3Zr	3.963	313	171	137	219	119	301	1.84	0.27	10.36	35	325	2402	-0.69
Rh_3Hf	3.949	322	178	147	226	125	317	1.81	0.27	15.18	31	301	2461	-0.75
Ru_3Sc	3.938	244	191	84	208	61	167	3.40	0.37	7.94	107	262	1992	-0.04
Ru_3Zr	3.969	294	203	112	233	89	237	2.62	0.33	10.21	91	292	2290	-0.11
Ru_3Hf	3.955	300	209	118	239	92	245	2.60	0.33	15.00	91	267	2324	-0.22

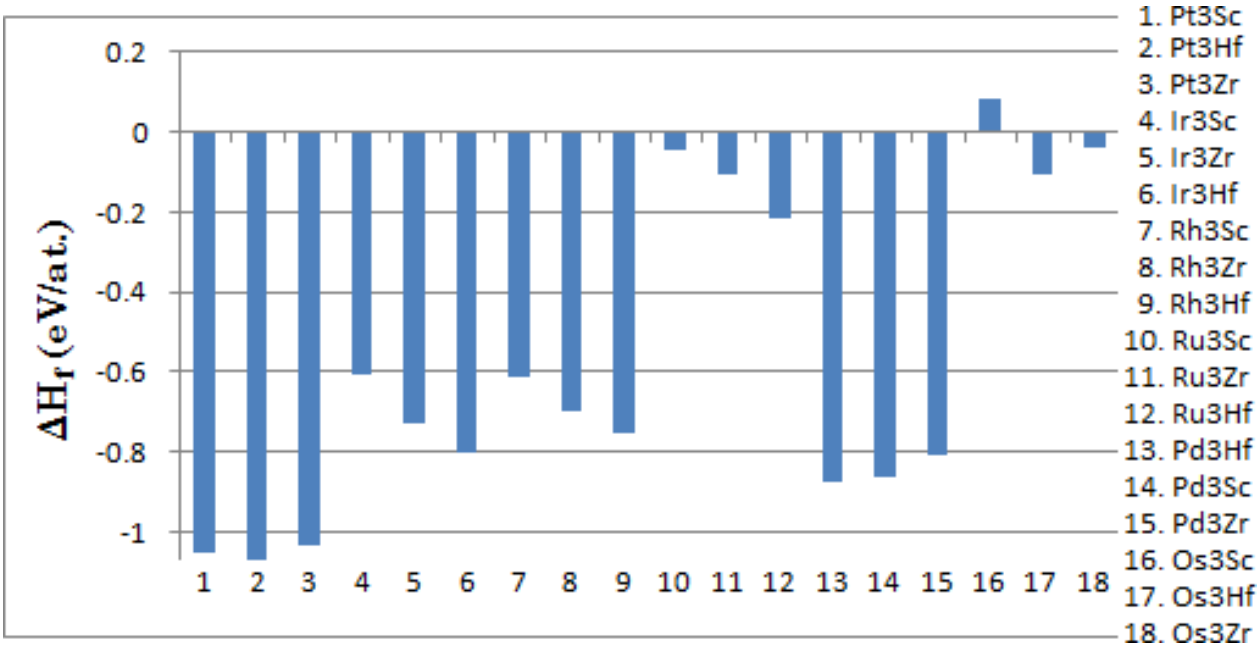

Figure 6.1: Heats of formation for fcc X_3B compounds.

by $L1_2$-Pt_3Sc and $L1_2$-Pt_3Zr, while the least stable structure were those of $L1_2$-Ru_3Sc and $L1_2$-Os_3Zr. The formation of solid-solution is predicted to be highest in those compounds with high negative heat of formation and hence, the strength of interaction between element X (where X = Pt, Ir, Os, Rh, Pd Ru) and B (where B = Sc, Zr, Hf) to form the compound X_3B , varies in the order of X-Hf > X-Zr > X-Sc (trend shown in Figure 6.2).

6.2.2 Shear Modulus and Hardness

The shear modulus was obtained from the elastic stiffness constants according to the Voigt-Reuss-Hill averaging methods [148]. Since the shear modulus correlates with hardness better than the bulk modulus, the shear modulus was used in this work to gauge hardness. According

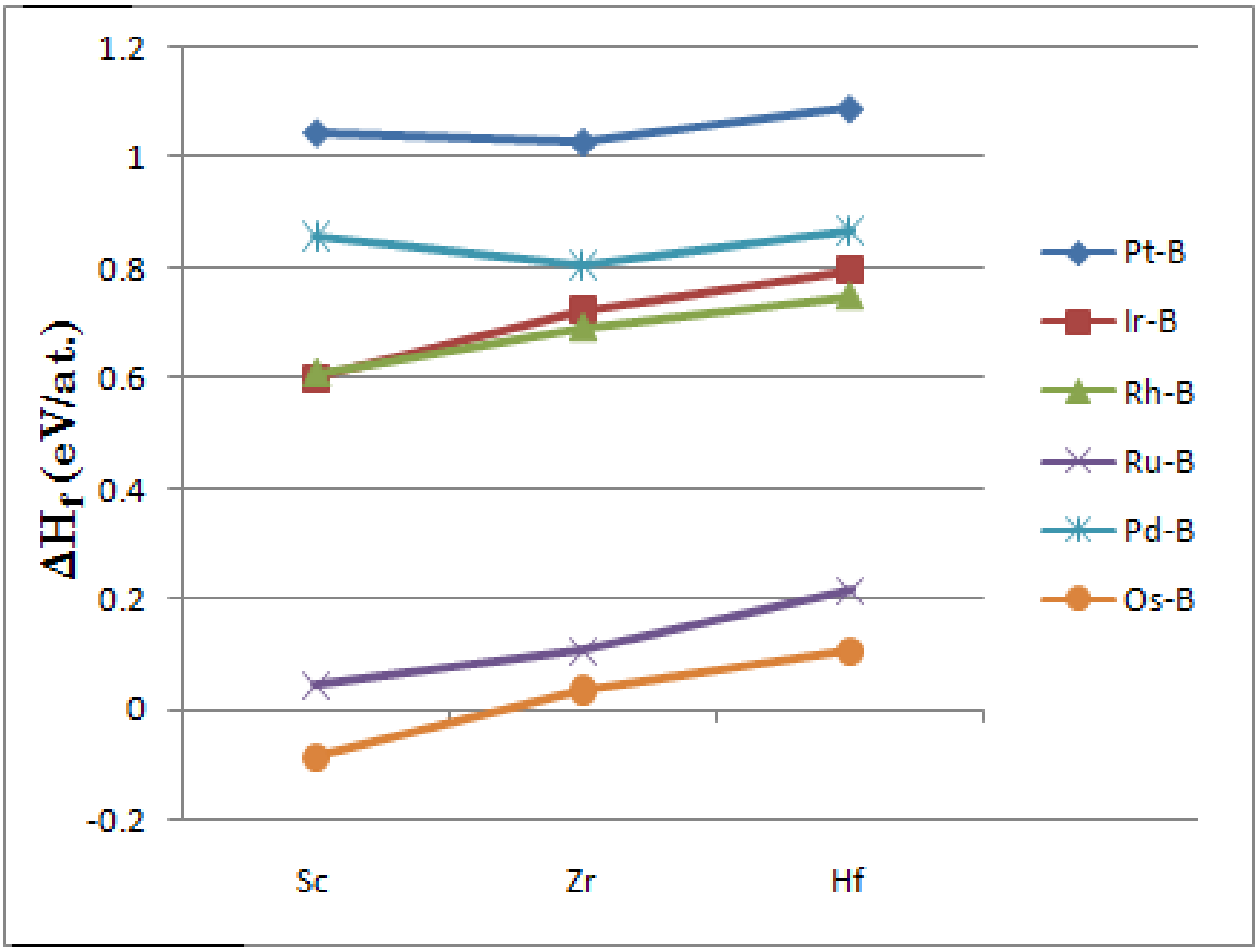

Figure 6.2: Reaction trend between elements X and B to form fcc X_3B compounds

to the calculations, the shear modulus Figure 6.3. predicted highest hardness for $L1_2$-Ir_3Hf, while the compound with least hardness was $L1_2$-Ru_3Al.

6.2.3 Cauchy Pressure, B/G ratio and Ductility

The Cauchy Pressure (CP) and/or the bulk (B) to shear (G) modulus B/G ratio have been used with success to characterize ductile/brittle behavior in a compound. Cauchy pres-

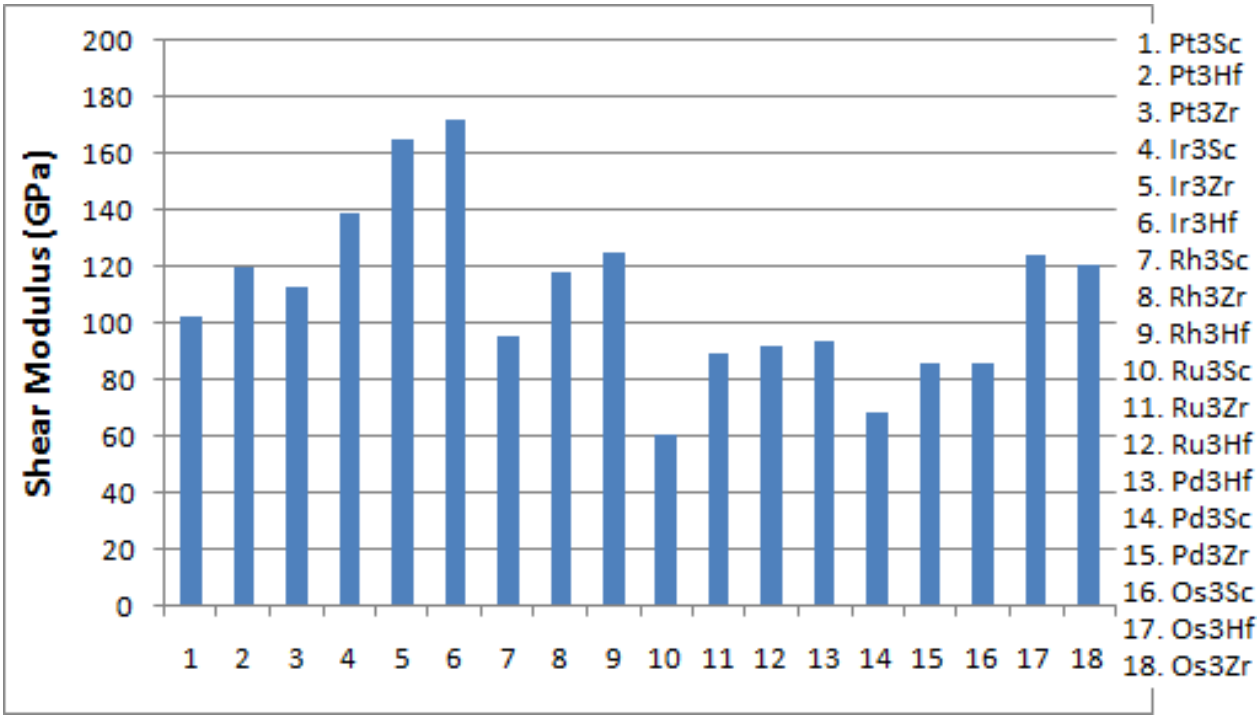

Figure 6.3: Calculated shear modulus for fcc X_3B compounds.

sure is defined as C_{12} - C_{44}. According to this calculation, both CP and B/G ratio gave similar trend. A plot of B/G ratio against CP is shown in Figure 6.4 for all the X_3B compounds. Any compound with B/G $>$ 1.75 and high CP value is considered ductile. The higher the CP value, the more ductile the compound. According to Figure 6.4, most of the compounds, especially; $L1_2$-Os_3Sc, $L1_2$-Ru_3Sc, $L1_2$-Ru_3Hf, $L1_2$-Ru_3Zr, $L1_2$-Os_3Hf, $L1_2$-Os_3Zr, $L1_2$-Pt_3Sc, $L1_2$-Pt_3Zr, $L1_2$-Rh_3Sc, $L1_2$-Pd_3Sc and $L1_2$-Pd_3Zr was predicted to exhibit good ductility. $L1_2$-Ir_3Zr and $L1_2$-Ir_3Hf were predicted to be brittle compounds. Also, the calculation showed that $L1_2$-Ir_3Sc, $L1_2$-Rh_3Zr and $L1_2$-Rh_3Hf were borderline compounds. However, being metallic compounds, it is predicted that they will show a more ductile than brittle behavior. Platinum is the most ductile metal [276, 277] and this was confirmed by this calculation.

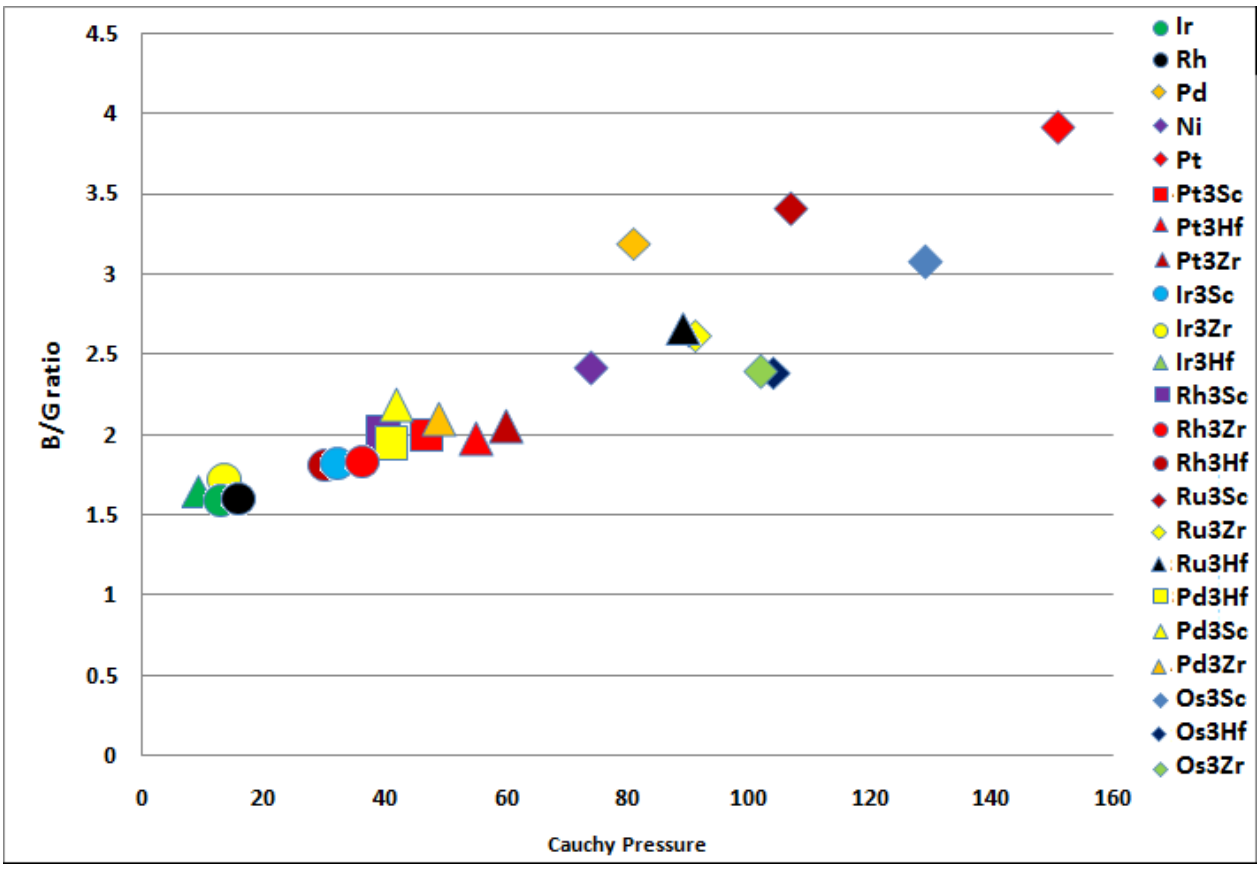

Figure 6.4: B/G ratio and Cauchy Pressure plot in fcc X_3B compounds.

6.2.4 Poisson's ratio, B/G ratio and Hardness

The Shear modulus (G) is related to the Poisson's ratio (v) as: $3/G = 2B \times (1-2v) \times (1+v)$. For hard materials, highly directional bonds plays a major role. The shear modulus will increase and give a low Poisson's ratio. Both the Poisson's and B/G ratios should be as low as possible for a hard material. According to the results in Figure 6.5, the compound with the highest hardness was predicted to be $L1_2 - Ir_3Hf$ and the least hard was $L1_2 - Os_3Al$.

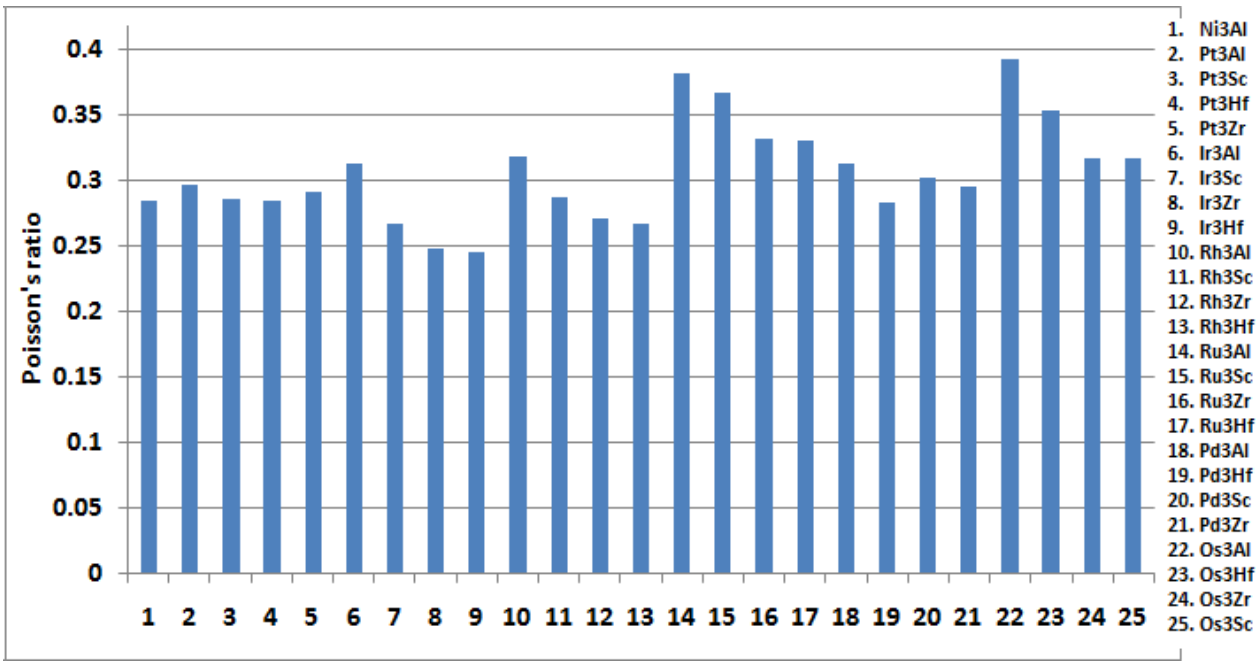

Figure 6.5: Calculated Poisson's ratio for some noble metal compounds.

6.2.5 Melting Points

From the elastic stiffness coefficients, the melting point of the fcc X_3B compounds was evaluated. According to Figure 6.5, the compound with highest melting point was Ir_3Hf.

6.3 Electronic Density of States for fcc X_3B compounds

The DOS plot for the $L1_2$-X_3B compounds are shown in Figure 6.6. At zero temperature, the $L1_2$ phase is not feasible in Os_3Sc, Os_3Zr, Os_3Hf, Ru_3Hf and Ru_3Zr. The Fermi level, E_F, on the DOS of these compounds falls on a peak, which is an indication of an unstable structure.

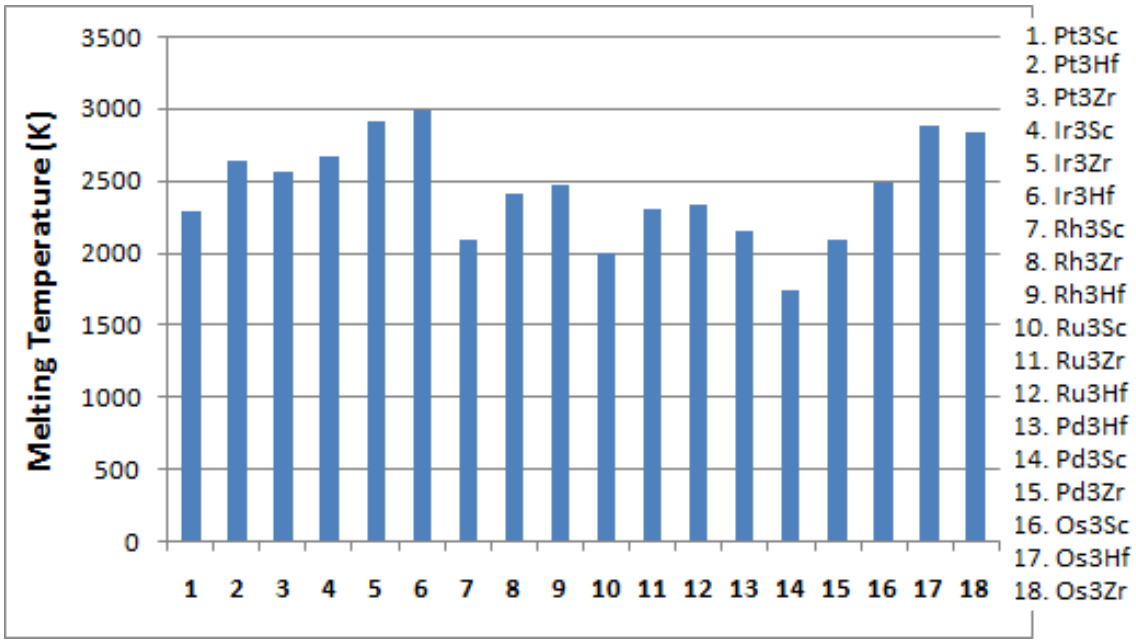

Figure 6.6: Calculated melting point for fcc X_3B compounds.

The formation of Pt_3Hf, Pt_3Zr, Pt_3Sc, Ir_3Sc, Ir_3Zr, Ir_3Hf, Rh_3Sc, Rh_3Zr, Rh_3Hf, Pd_3Sc and Ru_3Sc in the $L1_2$ phase is predicted by the DOS plots. For some of these compounds, E_F falls on the non-bonding side of the pseudogap (e.g. Rh_3Sc, Pd_3Sc) and for some others (e.g. Pt_3Hf, Pt_3Zr, Pd_3Hf, Pd_3Zr), the E_F was more on the anti-bonding side of the pseudogap. While the compounds having their E_F on the antibonding side are predicted metastable, a more stable structure can be achieved with element addition (ternary alloying). Elements such as Ru, Rh, Mo, Nb and Lr should be beneficial in this regard. Again, the density of the chosen element must be given adequate consideration to attain lightweight in the ternary compound.

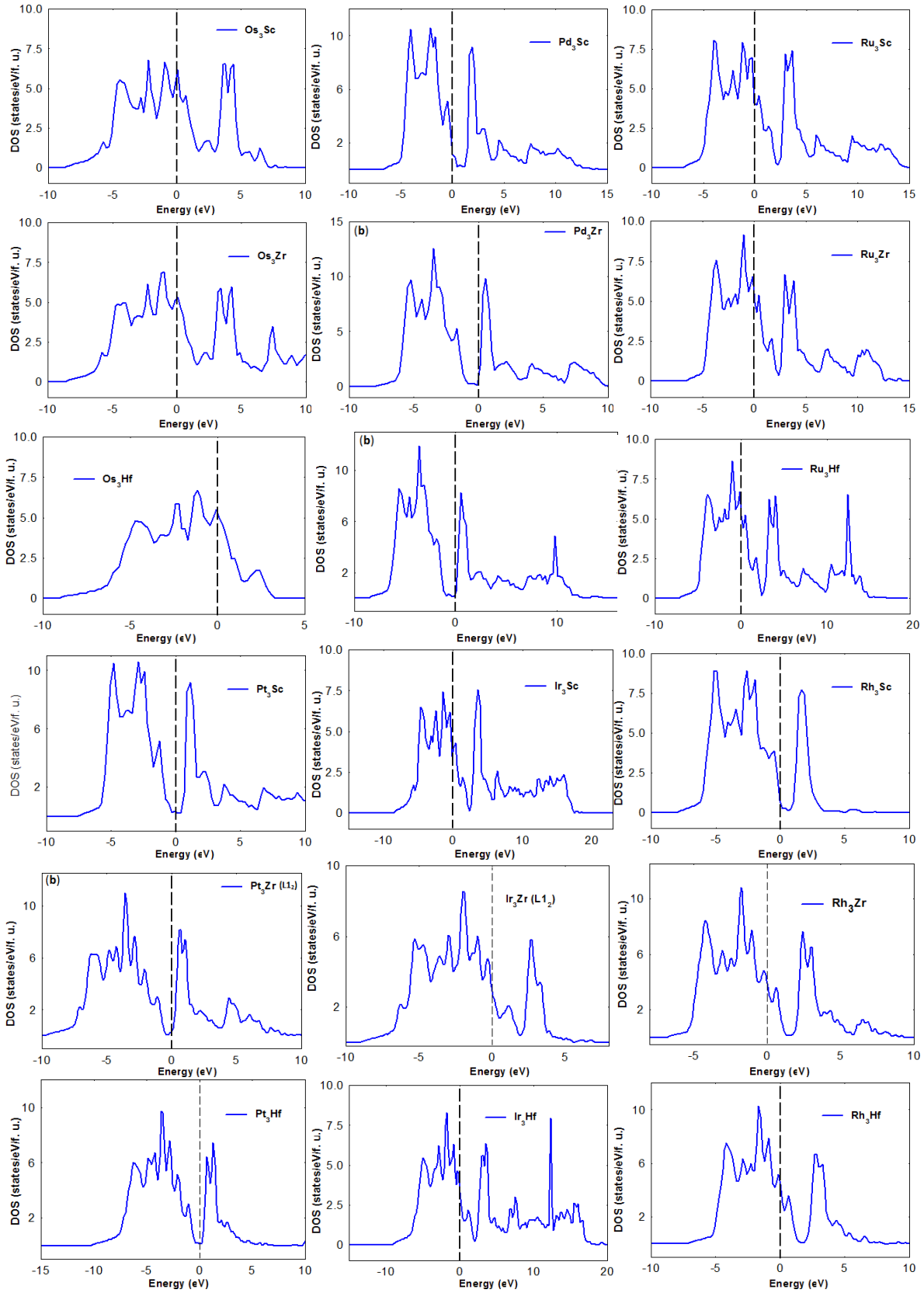

Figure 6.7: The total electronic density of states for phases of X_3B compounds. Energies relative to Fermi level are indicated by the dotted vertical line.

6.4 Summary

The results discussed hitherto have been on X_3B compounds with the fcc ($L1_2$) structures. Both $\triangle H_f$ (Figure 6.1) and DOS (Figure 6.7) agreed and predicts the existence of Pt_3Sc, Ir_3Sc, Ir_3Zr, Ir_3Hf, Rh_3Sc, Rh_3Zr, Rh_3Hf, Pd_3Sc, Pd_3Hf, Pd_3Zr and Ru_3Sc with the $L1_2$ structure, while Os_3Sc, Os_3Zr, Os_3Hf, Ru_3Hf and Ru_3Zr are unstable structures in the $L1_2$ phase. Available information [218, 219], showed that there is no reported phases in the Os-Sc system, while the stoichiometry; $L1_2$-Os_3Zr, $L1_2$-Os_3Hf, $L1_2$-Ru_3Hf and $L1_2$-Ru_3Zr does not exist on phase diagrams.

Two different structures have been reported for Pt_3Zr; Schulbert et al. [271] reported the $L1_2$, while Wallbaum [272] reported the $D0_{24}$ structure. The results calculated of the two competing structures (Figure 6.8) showed that the $D0_{24}$ is a more stable structure for this compound than the $L1_2$ structure.

A phase diagram of the Pt-Hf system was unknown. However, the intermetallic compound Pt_3Hf had been described [273, 274]. Similar to Pt_3Zr, both $L1_2$ and $D0_{24}$ structures have been reported for Pt_3Hf [218, 275]. The energy-volume plot and the DOS for the two competing structures are shown in Figure 6.9. By the results, both structures had equal probability for existence. This occurrence is attributable to phenomenon like inter-facial stress [278, 279]. A fit of the energy-volume curves to the Birch-Murnaghan equation of state showed that Pt_3Hf is more stable in the $D0_{24}$ structure than the $L1_2$. The fitted results are summarized

in Table 6.2.

The compound Pd_3Hf has been reported with both the $L1_2$ and $D0_{24}$ structures [218, 275]. At zero temperature, the energy-volume plot and the DOS curves (Figure 6.10) gave both phases equal probability of existence. However, a fit of the energy-volume curves to the Birch-Munaghan equation of state showed that Pd_3Hf was more stable in the $D0_{24}$ structure than the $L1_2$ structure. The fitted results are summarized in Table 6.2.

$L1_2$-Pd_3Zr was energetically favored by the $\triangle H_f$ calculation, but only the $D0_{24}$ structure is reported [280, 281]. According to the results in Figure 6.11, $D0_{24}$-Pd_3Zr was found to be more stable than $L1_2$-Pd_3Zr.

Based on the results in Table 6.2, Pt_3Hf, Pt_3Zr, Pd_3Hf and Pd_3Zr were more stable in the $D0_{24}$ structure, but harder and lighter in the $L1_2$ phase than the $D0_{24}$ phase. This prediction, which is supported by available experimental data [279] showed that the micro-hardness of $D0_{24}$-Pt_3Hf and $D0_{24}$-Pt_3Zr are $796H_V$ and $811H_V$ respectively. From the DOS results, it should be possible to stabilize the $D0_{24}$ phase to the $L1_2$ phase. Addition of low-electron elements into the compounds should be beneficial at reducing the energy of the system, thereby stabilizing the $D0_{24}$ structure to the $L1_2$ phase.

Conversely, it is possible for the other compounds with the $L1_2$ structure (i.e. Pt_3Sc, Ir_3Sc, Ir_3Zr, Ir_3Hf, Rh_3Sc etc.), to exhibit other phases when under different types of stress.

Table 6.2: Calculated lattice parameter (LP), equilibrium bulk modulus (B_0), equilibrium energy (E_0) , density (ρ^{cal}) and the melting points (m. p.) of some X_3B compounds with $L1_2$ and $D0_{24}$ structures . Experimental results are in brackets.

Compd.	phase	LP($\AA$)	B_0(GPa)	E_0(eV/at.)	ρ^{cal}(g.cm^{-3})	m.p. (K)	Refs.
	$L1_2$	4.035 [4.02]	290	-8.129	18.88		[279]
Pt_3Hf	$D0_{24}$	a = 5.636 [5.636]	151	-8.135	19.59[19.62]	2011±500	
		c = 9.208 [9.208]				[2400]	[279, 280, 282]
	$L1_2$	4.035	217	-6.957	10.01		
Pd_3Zr	$D0_{24}$	a = 5.612 [5.612]	216	-6.974	10.42	2621±500	
		c = 9.235 [9.235]				[2163±283]	[274, 280, 281]
						[2053±298]	
	$L1_2$	4.018	224	-7.392	14.64		
Pd_3Hf	$D0_{24}$	a = 5.595 [5.595]	220	-7.393	15.19	2661±500	
		c = 9.192 [9.192]				[2243]	[283, 284]
	$L1_2$	4.050	282	-7.693	14.31		
Pt_3Zr	$D0_{24}$	a = 5.644 [5.644]	280	-7.701	16.96[18.13]	3212±500[2523]	[213, 279, 282]
		c = 9.225 [9.225]					

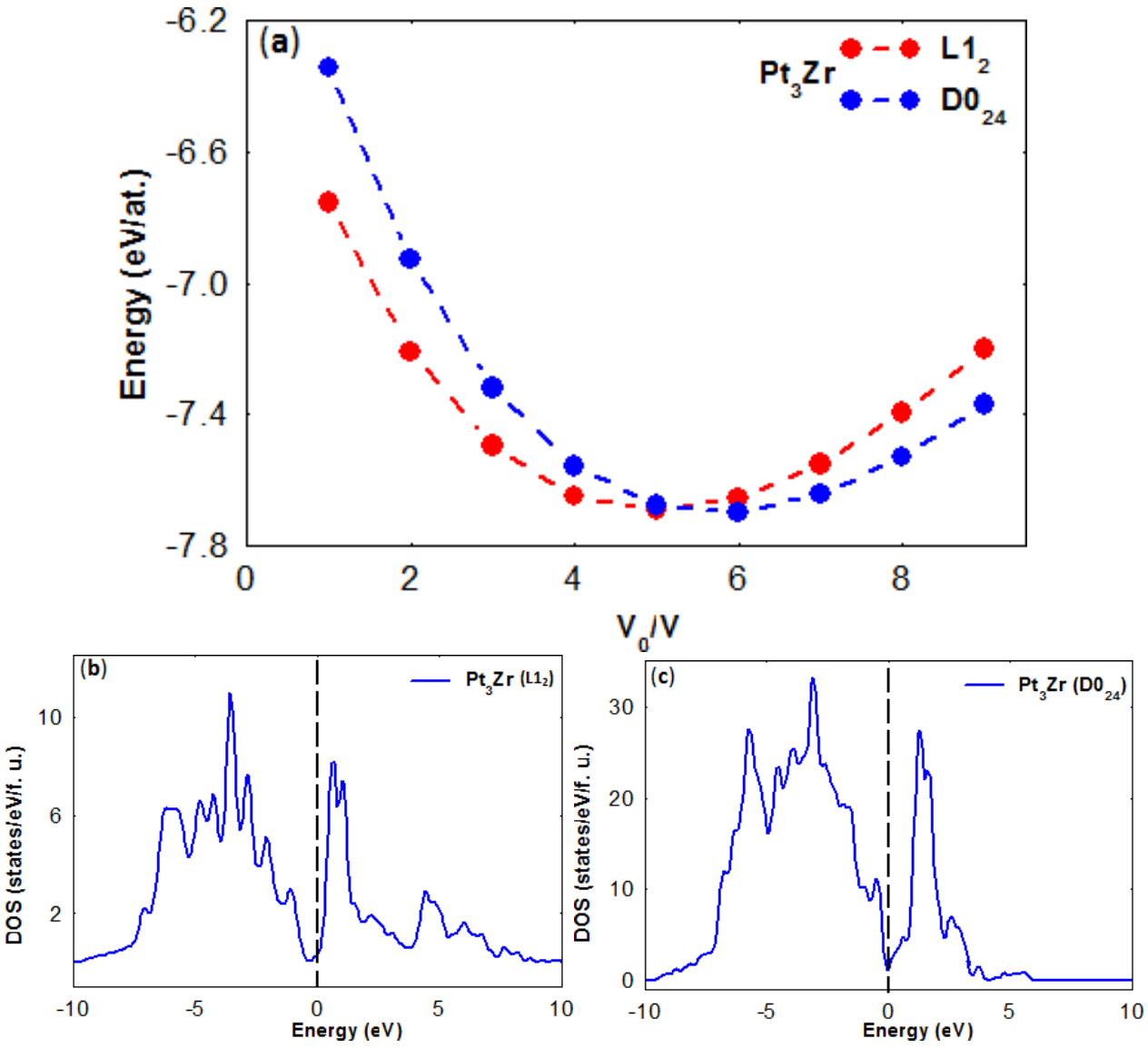

Figure 6.8: (a) calculated total energy-volume curve, (b) DOS for $L1_2$-Pt_3Zr and (c) DOS for $D0_{24}$-Pt_3Zr structures. The V_0/V axis had been magnified by a factor of 100 for better resolution.

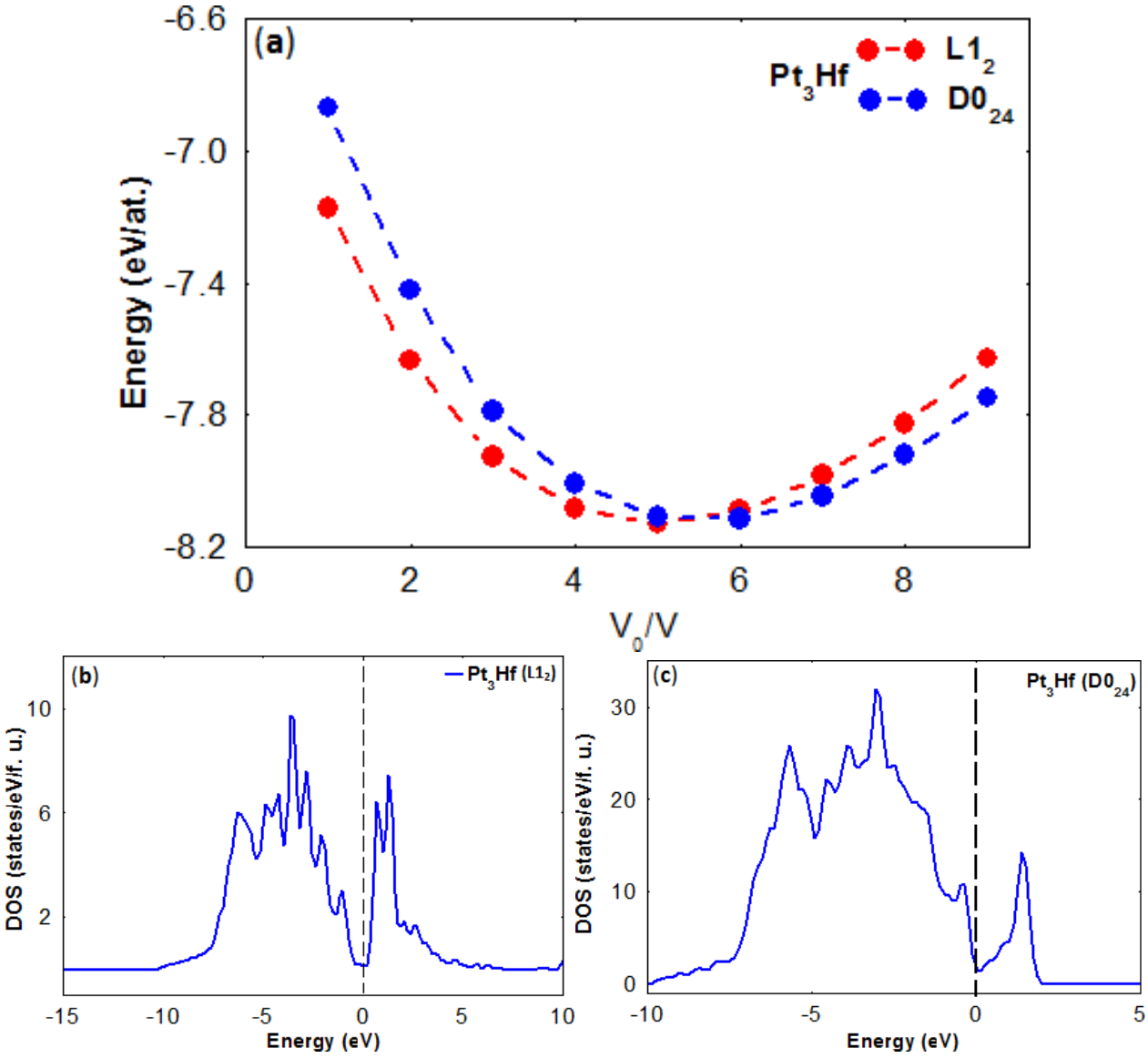

Figure 6.9: (a) calculated total energy-volume curves, (b) DOS for $L1_2$-Pt_3Hf and (c) DOS for $D0_{24}$-Pt_3Hf structures. The V_0/V axis had been magnified by a factor of 100 for better resolution.

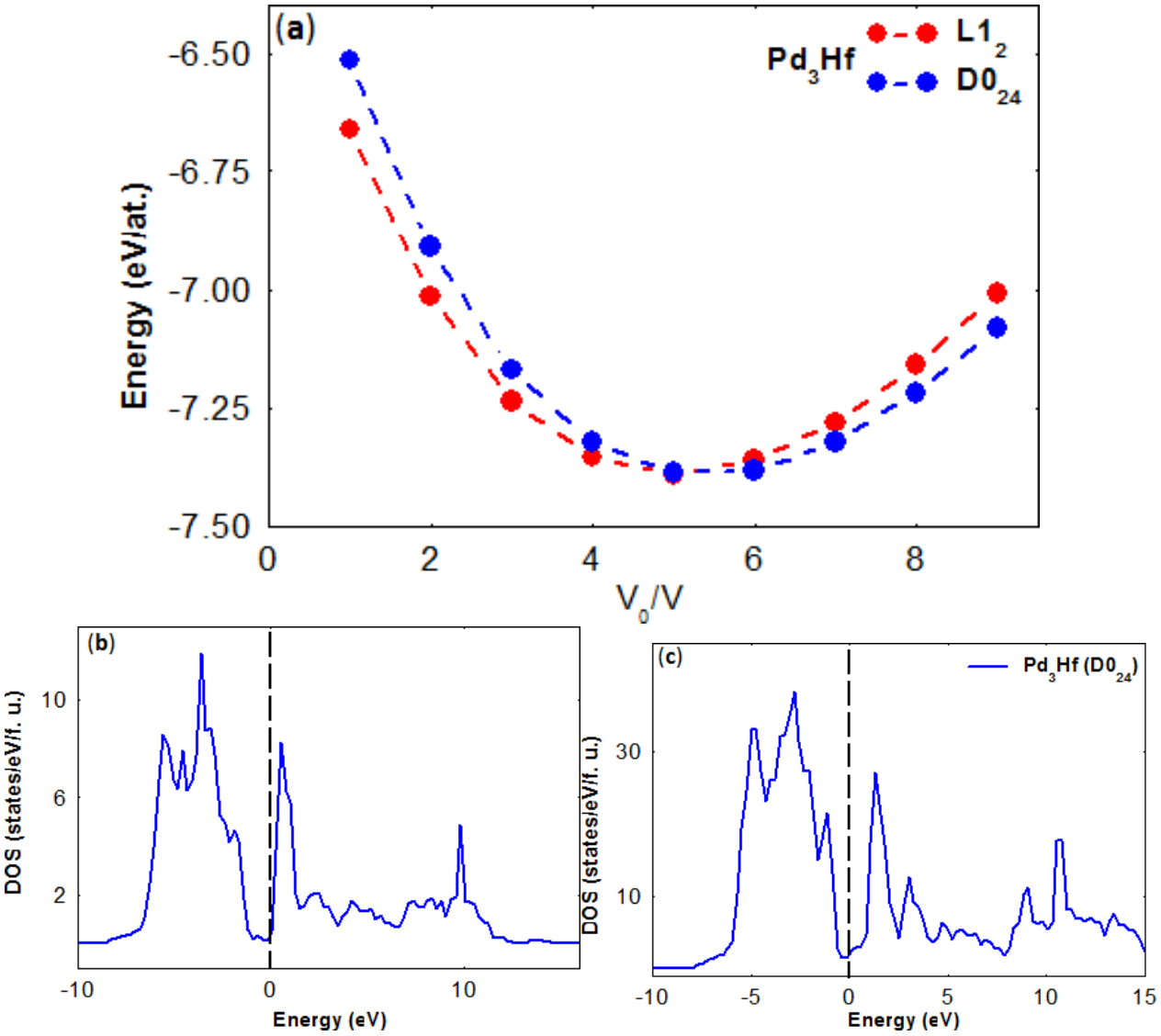

Figure 6.10: (a) calculated total energy-volume curves, (b) DOS for $L1_2$-Pd_3Hf and (c) DOS for $D0_{24}$-Pd_3Hf structures. The V_0/V axis had been magnified by a factor of 100 for better resolution.

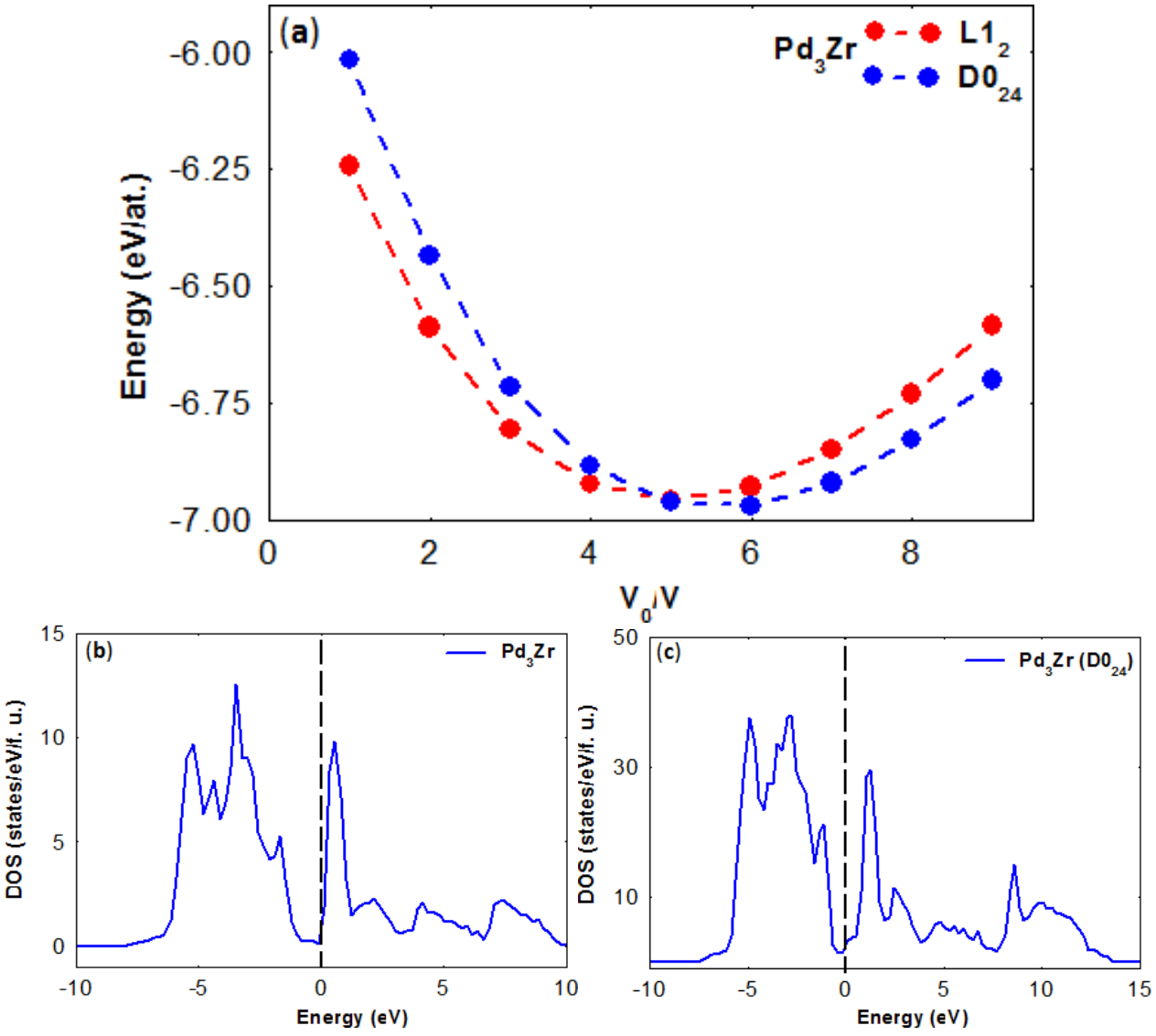

Figure 6.11: (a) calculated total energy-volume curves, (b) DOS for $L1_2$-Pd_3Zr and (c) DOS for $D0_{24}$-Pd_3Zr structures. The V_0/V axis had been magnified by a factor of 100 for better resolution.

Chapter 7

7.1 Conclusions

Both *ab initio* and molecular dynamics were used together in this thesis to study, ground state properties of noble metal compounds in the stoichiometry X_3Al and X_3B (where X = Pt, Ir, Rh, Ru, Pd and B = Sc, Zr, Hf). All *ab initio* results were obtained using density functional electronic structure total energy calculations. Sutton-Chen potentials were obtained for all noble metals and these were used to investigate the physics of the melting process in a typical X_3Al alloy. It was found that Al shows greater diffusion than the other metal in each of the alloys. Based on the PAW-GGA pseudopotential method, the elastic constants, phase stability, heat of formation, Debye temperature and the melting temperatures of these compounds were systematically studied. The calculated heat of formation showed that compounds in the stoichiometry $L1_2$-Os_3Al, $L1_2$-Os_3Sc, $L1_2$-Ru_3Al, $L1_2$-Ru_3Sc, $L1_2$-Ru_3Zr, $L1_2$-Os_3Hf and $L1_2$-Os_3Zr were not probably energetically favored.

Regarding phase stability, compounds like Pt_3Sc, Ir_3Sc, Ir_3Zr, Ir_3Hf, Rh_3Sc, Rh_3Zr, Rh_3Hf and Pd_3Sc are predicted to be stable in the $L1_2$ phase, while Pt_3Hf, Pt_3Zr, Pd_3Hf and Pd_3Zr are metastable and would have the $D0_{24}$ structure at ground state. However, as the compounds with the ground state $D0_{24}$ structures are harder and lighter in the $L1_2$ phase than in the $D0_{24}$ phase, the stability of these compounds from the $D0_{24}$ to the $L1_2$ phase will be beneficial. Apart from the high shear modulus values $L1_2$-Pt_3Hf (120 GPa) and $L1_2$-Pt_3Zr (113 GPa), solid solution is readily formed in these compounds.

The shear modulus among compounds with the $L1_2$ structures, compared with $L1_2$-Ni_3Al (92 GPa) showed that $L1_2$-Ir_3Hf (172 GPa), $L1_2$-Ir_3Zr (165 GPa), $L1_2$-Ir_3Sc (139 GPa), $L1_2$-Pt_3Sc (103 GPa), $L1_2$-Rh_3Zr (119 GPa) and $L1_2$-Rh_3Hf (125 GPa) had higher values and are predicted to give better mechanical property than $L1_2$-Ni_3Al. The calculated melting point for these compounds were at least 500K above the melting point for $L1_2$-Ni_3Al.

The melting points predicted by the Q-Sc potentials for elements with low melting points was within acceptable ranges, while the results for elements with high melting points was grossly over-predicted. Although the melting points were over-predicted similar trends were obtained from both *ab initio* and MD calculations. The melting point given by MD calculation for Pt_3Al was only 3.8% more than the experimental value, which does not in anyway suggest that the melting point for other high melting compounds may not have suffered from over-prediction. The over-prediction could be as a result of defects and imperfection in crystal structures. This tendency needs to be considered whenever the S-C potential is used in

simulating high temperature metallic phases.

As indicated by the density (ρ^{cal}), shear modulus (G) and B/G ratio calculations, compounds with highest potential were; $L1_2$-Ir_3Al, $L1_2$-Pt_3Al, $L1_2$-Pt_3Sc, $L1_2$-Ir_3Sc, $L1_2$-Rh_3Sc and $L1_2$-Rh_3Zr. Other compounds with densities comparable to $L1_2$-Ni_3Al such as $L1_2$-Rh_3Al, $L1_2$-Ru_3Al, $L1_2$-Pd_3Sc and $L1_2$-Ru_3Sc were found with lower strength. The results obtained from the MD and *ab initio* bulk modulus showed similar trends (i.e. $Os_3Al > Ir_3Al > Pt_3Al > Rh_3Al$), suggesting an agreement between the two methods of calculation.

7.2 Outlook

The present work had performed *ab initio* DFT and MD calculations on some binary as well as ternary noble metal alloys. Based on available codes - VASP and DL-POLY, the melting and mechanical properties of these compounds have been studied. In the context of several available approaches, it is suggested that these compounds be investigated with other codes and result compared with the data discussed here.

It is well established that imperfection in crystal structures and different defect types can impact on crystal properties (i.e. melting etc.), the compounds discussed in this thesis are suggested for further investigation particularly regarding defects. The temperature and pressure dependence (phase diagram) of the compounds were not systematically studied.

This area is also suggested for further work.

The DOS results presented in this study was primarily to understand phase stability. Other approaches such as the band-structure, electron localization function, charge density etc will provide the same information. However, for more detailed information, particularly regarding bonding, these other studies are suggested on these compounds in any future work.

References

[1] W. Kohn and L.J. Sham. *Phys. Rev.*, 140:A1133 – A1138, 1965.

[2] L. Hedin and B.I. Lundqvist. *J. Phys. C: Solid State Phys.*, 4:2064 – 2085, 1971.

[3] D.M. Ceperley and B.J. Alder. *Phys. Rev. Lett.*, 45:566 – 569, 1980.

[4] J.P. Perdew and A. Zunger. *Phys. Rev. B*, 23:5048 – 5079, 1981.

[5] M.J. Mehl and D.A. Papaconstantopoulos. *Phys. Rev. B*, 54:4519 – 4530, 1996.

[6] N.I. Papanicolaou, H. Chamati, G.A. Evangelakis and D.A. Papaconstantopoulos. *Comput. Mater. Sci.*, 27:191 – 198, 2003.

[7] T. Cagin, G. Dereli, M. Uludogan and M. Tomak. *Phys. Rev. B*, 59:3468 – 3473, 1999.

[8] S.L. Kakani and Amit Kakani. *Material Science*. New Age International Publishers, New Delhi, 2006.

[9] E.P. Busso and F.A. Mcclintock. *Acta Metall. Mater.*, 42:3263 – 3275, 1994.

[10] A.I. Taub and R.L. Fleischer. *Science*, 243:616 – 621, 1989.

[11] http://www.ndt-ed.org Accessed August 18, 2011.

[12] W. Hume-Rothery and H.M. Powell. *Z. Kristallogr.*, 91:23, 1935.

[13] W. Hume-Rothery, R.W. Smallman and C.W. Haworth. *The Structure of Metals and Alloys*. The Institute of Metals, London, 1969.

[14] www.synl.ac.cn/org/non/zu1/knowledge/Hume-Rothery-rules. Accessed July 10, 2012.

[15] C.T. Sims, N.S. Stoloff and W.C. Hagel (Eds.). *Superalloys II*. Wiley Inter-Science, New York, 1987.

[16] G.K. Dey and J.A. Sekhar. *Metall. Mater. Trans. B*, 28:905 – 918, 1997.

[17] K. Aoki and O. Izumi. *J. Mater. Sci.*, 14:1800 – 1806, 1979.

[18] K. Aoki and O. Izumi. *Jpn. Inst. Met.*, 43:1190, 1979.

[19] W.B Pearson. *A Handbook of Lattice Spacings and Structures of Metals and Alloys*. Pergamon, Oxford, 1967.

[20] L.A. Cornish, B. Fischer and R. Völkl. *MRS Bulletin*, 28:632 – 638, 2003.

[21] C.L. Briant. *Mater. Res. Soc. Symp. Proc.*, 232:305 – 310, 1994.

[22] Y. Yamabe et al. *Scripta Mater.*, 35:211 – 215, 1996.

[23] I.M. Wolf and P.J. Hill. *Plat. Met. Rev.*, 44:158 – 165, 2000.

[24] P.J. Hill, L.A. Cornish, M.J. Witcomb and I.M. Wolf. *Proc. Int. Symp. on High Temperature Corrosion and Protection*. Science Reviews, Japan, 2000.

[25] J.B. Knight and B. Taylor. *Powder Metallurgy*, 10:108 – 118, 1962.

[26] L.A. Cornish, J. Hohls, P.J. Hill, S. Prins, R. Süss and D.N. Compton. *J. of Min. and Metall.*, 38:197 – 204, 2002.

[27] M.V. Whalen. *Plat. Met. Rev.*, 32:2 – 10, 1988.

[28] Y. Yamabe-Mitarai, Y. Gu, C. Huang, R. Völkl and H. Harada. *JOM*, 56:3 – 39, 2004.

[29] C. Kittel. *Introduction to Solid State Physics*. Wiley and Sons, India, 2004.

[30] M. Hansen and K. Andreco. *Constitution of binary alloys*. McGraw-hill, New-York, 1958.

[31] Y. Yamabe-Mitarai, M-H. Hong, Y. Ro, and H. Harada. *Phil. Mag. Lett.*, 79:673 – 682, 1999.

[32] Y. Yamabe-Mitarai, Y. Ro and S. Nakazawa. *Intermetallics*, 9:423 – 429., 2001.

[33] D.M. Wee and T. Suzuki. *Trans. JIM*, 20:634 – 646, 1979.

[34] S. Miura, K. Honma, Y. Terada, J.M. Sanchez and T. Mohri. *Intermetallics*, 8:785 – 791, 2000.

[35] Y.F. Gu, Y. Yamabe-Mitarai, Y. Ro, T. Yokokawa and H. Harada. *Met. Mater. Trans. A*, 30:2629 – 2639, 1999.

[36] Y.F. Gu, Y. Yamabe-Mitarai and H. Harada. *Proc. Int. Symp. on Iridium. TMS, Nashville, Tennessee, USA*, 2000.

[37] Y.F. Gu, Y. Yamabe-Mitarai, S. Nakazawa and H. Harada. *Scripta Mater.*, 46:137 – 142, 2002.

[38] J.H. Westbrock. *Trans. Metall. Soc. AIME*, 209:898 – 904, 1957.

[39] R.L. Fleischer, R.D. Field and C.L. Briant. *Met. Trans. A*, 22A:129 – 137, 1991.

[40] Y. Yamabe-Mitarai, S. Nakazawa and H. Harada. *JSME Inter. Jour. A*, 45:2 – 7, 2002.

[41] Y. Yamabe-Mitarai, Y. Koizumi, H. Murakami, Y. Ro, T. Maruko and H. Harada. *Scripta Mater.*, 36:393 – 398, 1997.

[42] Y.F. Gu, Y. Yamabe-Mitarai, Xihong Yu and H. Harada. *Mater. Lett.*, 41:45 – 51, 1999.

[43] Y. Gu, Y. Yamabe-Mitarai and H. Harada. *Metall. Mater. Trans.*, 33A:1281 – 1283, 2002.

[44] W. Bronger and W. Klemm. *Z. Anorg. Allg. Chem.*, 319:58 – 80, 1962.

[45] Y. Yamabe-Mitarai, Y. Ro, T. Maruko and H. Harada. *Metall. Mater. Trans A*, 29:537 – 549, 1998.

[46] X.H. Yu, Y. Yamabe-Mitarai, Y. Ro and H. Harada. *Metall. Mater. Trans. A*, 31:173 – 178, 2000.

[47] X.H. Yu, Y. Yamabe-Mitarai, S. Nakazawa, Y. Ro and H. Harada. *Metall. Mater. Trans. A*, 32A:1347 – 1353, 2001.

[48] C. Huang, K. Nishida, Y. Yamabe-Mitarai and H. Harada. *Intermetalics*, 10:893 – 902, 2002.

[49] C. Huang, Y. Yamabe-Mitarai, K. Nishida and H. Harada. *Intermetallics*, 11:917 – 926, 2003.

[50] C. Huang, Y. Yamabe-Mitarai and H. Harada. *J. Alloys Comp.*, 366:217 – 221, 2004.

[51] Y. Yamabe-Mitarai, Y. Gu and H. Harada. *Metall. Mater. Trans.*, 34A:2207 – 2215, 2003.

[52] Y. Gu, Y. Yamabe-Mitarai, S. Nakazawa and H. Harada. *JSME Inter. Jour. A*, 45:8 – 13, 2002.

[53] Y. Yamabe-Mitarai and H. Harada. *J. Alloys and Comp.*, 361:169 – 179, 2003.

[54] B. Fischer, A. Behrends, D. Freund, D.E. Lupton and Jürgen Merker. *Plat. Met. Rev.*, 43:18 – 28, 1999.

[55] D.M. Wee, O. Noguchi, Y. Oya and T. Suzuki. *Trans. JIM*, 21:237 – 242, 1980.

[56] D.M. Wee, D.P. Pope and V. Vitek. *Acta Metall.*, 32:829 – 836, 1984.

[57] L.A. Cornish, J. Hohls, P.J. Hill, S. Prins, R. Süss and D.N. Compton. *J. Min. Met.*, 38:197 – 204, 2002.

[58] P.J. Hill, T. Biggs, P. Ellis, J. Hohls, S. Taylor and I.M. Wolff. *Mater. Sci. Eng. A*, 301:167 – 179, 2001.

[59] P.J. Hill, N. Adams, T. Biggs, P. Ellis, J. Hohls, S.S. Taylor and I.M. Wolff. *Mater. Sci. Eng.*, 329A:295 – 304, 2002.

[60] H. Meininger and M. Ellner. *J. Alloys Comp.*, 353:207 – 212, 2003.

[61] T. Biggs, M.B. Cortie, M.J. Witcomb and L.A. Cornish. *Plat. Met. Rev.*, 47:142 – 156, 2003.

[62] R. Völkl, D. Freund and B. Fischer. *J. Test. Eval.*, 31:35 – 43, 2003.

[63] R. Süss, R. Völkl, D. Freund, B. Fischer, P.J. Hill, P. Ellis and I.M. Wolff. *Mater. Sci. Eng.*, A338:133 – 141, 2002.

[64] O.K. Andersen, O. Jepsen and D. Glotzel. *in Highlights of Condensed Matter Theory, editors: F. Bassani, F. Fumi and M. Tosi*. North-Holland, New York, 1985.

[65] A.V. Ruban and H.L. Skriver. *Comput. Mater. Sci.*, 15:119, 1999.

[66] G.H. Johannesson, T. Bligaard, A.V. Ruban, H.L. Skriver, K.W. Jacobsen and J. K. Norskov. *Phys. Rev. Lett.*, 88(25):255506 (1 – 5), 2002.

[67] V.I. Razumovskiy, E.I. Isaev, A.V. Ruban and P.A. Korzhavyi. *Intermetallics*, 16:982 – 986, 2008.

[68] S.V. Prikhodko, H. Yang, A.J. Ardell, J.D. Carnes and D.G. Isaak. *Metall. Mater. Trans. A*, 30:2403, 1999.

[69] K. Chen, L.R. Zhao and J.S. Tse. *J. Appl. Phys.*, 93:2414 2417, 2003.

[70] M.H. Yoo and C.L. Fu. *ISIJ Inter.*, 31:1049 – 1062, 1991.

[71] Y. Terada, K. Ohkubo, S. Miura, J.M. Sanchez and T. Mohri. *J. Alloys and Comp.*, 354:202 – 207, 2003.

[72] M. Rajagopalan and M. Sundareswari. *Jour. of Alloys and Comp.*, 379:8 – 15, 2004.

[73] M.A. Schtremel. *Firmness of alloys; Defects of a lattice*. Metallurgy, Moscow, 1982.

[74] L.I. Vasilev and A.N. Orlov. *Phys. of metals and metall.*, 15, 1963.

[75] J.J. Lagowski (Ed.). *Chemistry Foundations and Applications*. Thomson Gale, NewYork, 2004.

[76] R. David. *Handbook of Chemistry and Physics*. CRC Press, New York, 2007 - 2008.

[77] G.V. Samsonov (Ed.). *Handbook of the physicochemical properties of the elements*. IFI-Plenum, New York, USA, 1968.

[78] G.W.C. Kaye and T.H. Laby. *Tables of physical and chemical constants*. Longman, London, 1993.

[79] Rhodium. www.periodic.lanl.gov. Accessed December, 2010.

[80] www.chemicool.com/elements/ruthenium. Accessed May 18, 2012.

[81] L.B. Hunt. *Plat. Met. Rev.*, 31:32 – 41, 1987.

[82] D.R. Lide (ed). *CRC handbook of chemistry and physics*. CRC Press, Boston, USA, 1990.

[83] A.M. James and M.P. Lord. *Macmillan's Chemical and Physical Data*. Macmillan, London, 1992.

[84] http://heraeus-catalysts.com. Accessed April 12, 2012.

[85] J.R. Minkel. *Phys. Rev. Focus 9*, 23, 2002.

[86] M.B. Weinberger, S.H. Tolbert and A. Kavner. *Phys. Rev. Lett.*, 100:045506 (1 – 4), 2008.

[87] C. Hyunchae, J.E. Klepeis, C.S. Yeo and D.A. Young. *Phys. Rev. Lett.*, 88:135701 – 135704, 2002.

[88] B.R. Sahu and L. Kleinman. *Phys. Rev. B*, 72:113106 (1 – 3), 2005.

[89] http://education.jlab.org/itselemental/ele076.htm. Accessed April 12, 2012.

[90] R.M. Martin. *Electronic Structure, Basic Theory and Practical Methods*. Cambridge University Press, UK., 2004.

[91] M. Born and J.R. Oppenheimer. *"Zur Quantentheorie der Molekeln," Ann. Physik*, 84:457 – 484, 1927.

[92] D.R. Hartree. *Proc. Cambridge Phil. Soc.*, 24:89 – 110, 1928.

[93] V. Fock. *Zeitsschrift fur Physik*, 61:126, 1930.

[94] J.C. Slater. *Phys. Rev.*, 51:846 – 851, 1937.

[95] M.P. Marder. *Condensed Matter Physics*. John Wiley and Sons, New York, 2000.

[96] L.H. Thomas. *Proc. of Cambridge Philo. Soc.*, 23:542 – 548, 1927.

[97] E. Fermi. *Zeitschrift Fur Physik*, 43:73, 1928.

[98] P. Hohenberg and W. Kohn. *Phys. Rev. B*, 136:864 – 871, 1964.

[99] U. Von Barth and L. Hedin. *J. Phys. C: Solid State Phys.*, 5:1629 – 1642, 1972.

[100] J.F. Janak. *Solid State Commun.*, 25:53, 1978.

[101] S.H. Vosko, L. Wilk and M. Nusair. *Can. J. Phys.*, 58:1200 – 1211, 1980.

[102] J.P. Perdew and Y. Wang. *Phys. Rev. B*, 45:13244 – 13249, 1992.

[103] J.P. Perdew, J.A. Chevary, S.H. Vosko, K.A. Jackson, M. Pederson, D.J. Singh and C. Fiolhais. *Phys. Rev. B*, 46:6671 – 6687, 1992.

[104] A.D. Becke. *Phys. Rev. A*, 38:3098 – 3100, 1988.

[105] M. Levy and J.P. Perdew. *Phys. Rev. A*, 32:2010 – 2021, 1985.

[106] E.H. Lieb and S. Oxford. *Int. J. Quantum Chem.*, 19:427 – 439, 1981.

[107] J.P. Perdew, K. Burke and M. Ernzerhof. *Phys. Rev. Lett.*, 77:3865 – 3868, 1996.

[108] J.P. Perdew, K. Burke and M. Ernzerhof. *Phys. Rev. Lett.*, 78:1396 – 1396, 1997.

[109] J. Hafner. *J. of Comput. Chem.*, 29:2044 – 2078, 2008.

[110] L.J. Sham and W. Kohn. *Phys. Rev.*, 145:561 – 567, 1966.

[111] Stewart Clark. *Complex Structure in Tetrahedral Semiconductors.* PhD Thesis, University of Edinburgh, 1994.

[112] A. Balereschi. *Phys. Rev. B*, 7:5212 – 5215, 1973.

[113] S. Froyen. *Phys. Rev. B*, 39:3168 – 3172, 1989.

[114] J. Moreno and J.M. Soler. *Phys. Rev. B*, 45:13891 – 13898, 1992.

[115] H.J. Monkhorst and J.D. Pack. *Phys. Rev. B*, 13:5188 – 5192, 1976.

[116] Carsten Rostgaard. *The Projector Augmented-wave Method*. www.arxiv.org. Accessed Sept. 10, 2012.

[117] J.C. Phillips and L. Kleinman. *Phys. Rev.*, 116:287 – 294, 1959.

[118] M.L. Cohen and V. Heine. *Solid State Physics*, volume 24. Academic Press, New York, 1970.

[119] Philip P. Rushton. *Towards a non-local density functional description of exchange and correlation*. PhD thesis, University of Durham, 2002.

[120] T.A. Arias, M.C. Payne and J.D. Joannopoulos. *Phys. Rev. B*, 45:1538 – 1549, 1992.

[121] K. Laasonen, A. Pasquarello, R. Car, C. Lee and D. Vanderbilt. *Phys. Rev. B*, 47:10142 – 10153, 1993.

[122] L.Kleinman and D.M.Bylander. *Phys. Rev. Lett.*, 48:1425 – 1428, 1982.

[123] D. Vanderbilt. *Phys. Rev. B*, 41:7892 – 7895, 1990.

[124] G. Kresse, J. Hafner and R.J. Needsf. *J. Phys. Condens. Matter*, 4:7451 – 7468, 1992.

[125] P.E. Blöchl. *Phys. Rev. B*, 50:17953 – 17979, 1994.

[126] G. Kresse and D. Joubert. *Phys. Rev. B*, 59:1758 – 1775, 1999.

[127] G. Kresse. *The PAW and US-PP database.* www.vasp.at/vasp-workshop. Accessed Sept. 6, 2012.

[128] M.C. Payne, M.P. Teter, D.C. Allan, T.A. Arias and J.D. Joannopoulos. *Rev. of Mordern Phys.*, 64:1045, 1992.

[129] M.P. Teter, M.C. Payne and D.C. Allan. *Phys. Rev. B*, 40:12255 – 12263, 1989.

[130] P.E. Gill, W. Murray and M.H. Wright. *Practical Optimization.* Academic Press, London, 1981.

[131] G. Kresse and J. Furthmüller. *Comp. Mat. Sci.*, 6:15 – 50, 1996.

[132] G. Kresse and J. Furthmuller. *Phys. Rev. B*, 54:11169 – 11186, 1996.

[133] R. Car and M. Parrinello. *Phys. Rev. Lett.*, 55:2471 – 2474, 1985.

[134] V.N. Staroverov, G.E. Scuseria, J. Tao and J.P. Perdew. *Phys. Rev. B*, 69:07102 (1 – 11), 2004.

[135] F. Mittendorfer and J. Hafner. *J. Phys. Chem. B*, 106:13299 – 13305, 2002.

[136] R. Feynman. *Phys. Rev.*, 56:340 – 343, 1939.

[137] G. Ghosh and M. Asta. *Acta Materialia*, 53:3225 – 3252, 2005.

[138] C. Ravi. *Calphad*, 33:469 – 477, 2009.

[139] C. Stample, W. Mannstadt, R. Asahi and A.J. Freeman. *Phys. Rev. B*, 63:155106 – 155117, 2001.

[140] http://www.saskschools.ca/. Accessed April 12, 2012.

[141] F.D. Murnaghan. *Proc. USA Natl. Acad. Sci.*, 30:244 – 247, 1944.

[142] P. Vinet, J.R. Smith, J. Ferrante and J.H. Rose. *Phys. Rev. B*, 35:1945 – 1953, 1987.

[143] F.J. Birch. *Phys. Rev.*, 71:809 – 824, 1947.

[144] F.J. Birch. *Geophys. Res.*, 83:1257 – 1268, 1978.

[145] J.F. Nye. *Physical Properties of Crystals*. Clarendon, Oxford, 1960.

[146] A. Reuss. *Z. Angew. Math. Mech.*, 9:49 – 58, 1929.

[147] W. Voigt. *Lehrbuch der Kristallphysik*. Teubner Verlaggeselschaft, Stutgart, 1928.

[148] R. Hill. *Proc. Phys. Soc. Sect. A*, 65:349 – 354, 1952.

[149] L. Fast, J.M. Wills, B. Johansson and O. Eriksson. *Phys. Rev. B*, 51:17431 – 17438, 1995.

[150] P. Ravindran, P. Vajeeston, R. Vidya, A. Kjekshus and H. Fjellvag. *Phys. Rev. B*, 64:224509 – 224523, 2001.

[151] Y. Lee. *First Principles Calculations for X-Ray Resonant Spectra and Elastic Properties*. PhD thesis, Iowa State University, 2004.

[152] M.J. Mehl, B.M. Klein and D.A. Papaconstantopoulos. *Intermetallic Compounds: Principles and Practice*. John Wiley and Sons, London, 1995.

[153] D.C. Wallace. *Thermodynamics of Crystals*. Wiley, New York, 1972.

[154] O. Beckstein, J.E. Klepeis, G.L.W. Hart and O. Pankrtov. *Phys. Rev. B*, 63:134112 (1 – 12), 2001.

[155] Jiemin Wang, Jingyang Wang, Yanchun Zhou and Chunfeng Hua. *Acta Materialia*, 56:1511 – 1518, 2008.

[156] C.D. Gelatt, A.R. Williams Jr. and V.L. Moruzzi. *Phys. Rev. B*, 27:2005 – 2013, 1983.

[157] A. Pastural, C. Colinet and P. Hitter. *Physica B*, 132:177, 1985.

[158] T. Hong, T.J.W. Yang, X.Q. Guo, A.J. Freeman, T. Oguchi and J.H. Xu. *Phys. Rev. B*, 43:1940 – 1947, 1991.

[159] J.H. Xu and A.J. Freeman. *Phys. Rev. B*, 41:12553 – 12561, 1990.

[160] J.H. Xu, T. Oguchi and A. J. Freeman. *Phys. Rev. B*, 36:4186 – 4189, 1987.

[161] P. Ravindran and R. Asokamani. *Bull. Mater. Sci.*, 20:613 – 622, 1997.

[162] M.E. Eberhart, D.P. Clougherty and J.M. Maclaren. *J. Mater. Res.*, 8:438 – 448, 1993.

[163] P.W. Thrush. *A Dictionary of Mining, Mineral, and Related Term.* U.S. Dept. Interior Bur. Mines Washington D.C., 1968.

[164] R.L. Bates and J.A. Jackson. *Glossary of Geology.* American Geol. Inst., 1980.

[165] R.J. Goble and S.D. Scott. *Canadian Minerologist*, 23:273 – 285, 1985.

[166] Dmitri Kopeliovich. *Hardness test methods.* www.substech.com. Accessed May 8, 2012.

[167] M. Hebbache. *Sol. St. Commun.*, 113:427 – 432, 2000.

[168] A.Y. Liu and M.L. Cohen. *Science*, 245:841 – 842, 1989.

[169] J.M. Leger, J. Haines, M. Schmidt, J.P. Petitet, A.S. Pereira and J.A.H. Dajornada. *Nature*, 383:401, 1996.

[170] D.M. Teter. *MRS Bull.*, 23:22 – 27, 1998.

[171] J.M. Leger, P. Djemia, F. Ganot, J. Haines, A.S. Pereira and J.A.H. da Jornada. *Appl. Phys. Lett.*, 79:2169 – 2171, 2001.

[172] C. Kocer, N. Hirosaki and S. Ogata. *Phys. Rev. B*, 67:035210, 2003.

[173] J.N. Plendi and P.J. Giblisse. *Z. Krist.*, 118:404 – 421, 1963.

[174] C.B. Geller et al. *Scripta Mater.*, 52:205 – 210, 2005.

[175] Engineers Edge. Ductility - strength of materials. www.engineersedge.com. Accessed March 9, 2012.

[176] S.F. Pugh. *Philos. Mag.*, 45:823 – 843, 1954.

[177] Eric A. Brandes and G.B. Brook (Editors). *Smithells Metals Reference Book*. Butterworth-Heinemann Ltd, UK, 1992.

[178] A.H. Cottrell. *Advances in Physical Metallurgy*. Institute of Metals, London, 1990.

[179] J. Schroers and W.L. Johnson. *Phys. Rev. Lett.*, 93:255506 (1 – 4), 2004.

[180] J.J. Lewandowski, W.H. Wang and A.L. Greer. *Phil. Mag. Lett.*, 85:77 – 87, 2005.

[181] I.N. Frantsevich, F.F. Voronov and S.A. Bokuta. *Handbook of Elastic Constants and Moduli of Metals and Insulators*. Naukova Dumka, Kievl, 1982.

[182] M.C. Gao, Ömer N. Dogan, P. King, A.D. Rollett and M. Widom. *The First-Principles Design of Ductile Refractory Alloys*. www.tms.org/jom.html. Accessed January 18, 2010.

[183] D.G. Pettifor. *Mater. Sci. Technol.*, 8:345 – 349, 1992.

[184] J. Dominec. *Phys. Status Solidi B*, 169:K83 – K85, 1992.

[185] G.S. Zhdanov. *Solid State Physics*. Moscow University Press, Moscow, 1961.

[186] T.L. Hill. *An Introduction to Statistical Thermodynamics*. Dover, New York, 1986.

[187] V.L. Moruzzi, J.P. Janak and K. Schwarz. *Phys. Rev. B*, 37:790 – 799, 1988.

[188] E.G. Moroni, G. Grimvall and T. Jarlborg. *Phys. Rev. Lett.*, 76:2758 – 2761, 1996.

[189] S.A. Ostaninand and V.Yu. Trubitsin. *Phys. Rev. B*, 57:13485 – 13490, 1998.

[190] G. Alers. Physical acoustics t.iii b. 1968.

[191] Anderson Liberman. Physical acoustics t.iv b. 1970.

[192] A.L. Dergachov and V.I. Starostin. *Ore Deposit Geology*, 6:67–75, 1981.

[193] O.L. Anderson. *J. Phys. Chem. Solids*, 24:909 – 917, 1963.

[194] K. Kunc and R.M. Martin. *Phys. Rev. Lett.*, 48:406 – 409, 1982.

[195] S. Baroni, P. Giannozzi and A. Testa. *Phys. Rev. Lett.*, 58:1861 – 1864, 1987.

[196] W. Frank, C. Elsasser and M. Fahnle. *Phys. Rev. Lett.*, 74:1791 – 1794, 1995.

[197] O.L. Anderson and W.P. Mason (Eds.). *Physical Acoustics III-B*. Academic Press, New York, 1965.

[198] G. Grimvall. *Thermophysical Properties of Materials*. North-Holland, Amsterdam, 1986.

[199] P. Debye. *Ann. d. Physik*, 39:789 – 839, 1912.

[200] E.Schreiber, O.L. Anderson and N. Soga. *Elastic Constants and their Measurements*. McGraw-Hill, New York, 1973.

[201] H. Siethoff and K. Ahlborn. *Phys. Status Solidi B*, 190:179 – 191, 1995.

[202] M. Blackman. *Phil. Mag.*, 42:1441 – 1442, 1951.

[203] H.B. Huntington. *Solid State Physics*. Academic Press, New York, 1958.

[204] J10 heat. www.mpec.sc.mahidol.ac.th. Accessed November, 2011.

[205] Http://En.Wikipedia.Org/Wiki/Platinum.

[206] F.A. Lindemann. *Physik Z.*, 11:609 – 612, 1910.

[207] S. Sorkin. *Point Defects, Lattice Structure, and Melting*. MSc Dissertation,Technion University, Israel, 2003.

[208] J. Solyom. *Fundamentals of the Physics of Solids*. Springer, Berlin, 2007.

[209] P. Hofmann. *Solid State Physics: An Introduction*. Wiley-VCH, 2008.

[210] D.R. Nelson. *Defects and Geometry in Condensed Matter Physics*. Cambridge University Press, Cambridge UK, 2002.

[211] M.E. Fine, L.D. Brown and H.L. Marcus. *Scrpt. Metall.*, 18:951 – 956, 1984.

[212] D.J. Skinner and M. Zedalis. *Scripta Metallurgica*, 22:1783 – 1785, 1988.

[213] G. Simmons and H. Wang. *A Handbook of Single Crystal Elastic Constants and Calculated Aggregate Properties*. MIT Press, Cambridge, 1971.

[214] R. Völkl, Y. Yamabe-Mitarai, C. Huang and H. Harada. *Metall. and Mater. Trans. A*, 36A:2881 – 2892, 2005.

[215] J. Donohue. *The Structures of the Elements*. Wiley, New York, 1974.

[216] I. Dobrina, N. Kloussis and S.P. LIM. *Phys. Rev. B*, 54:14413 – 14422, 1996.

[217] A. Tari. *The Specific Heat of Matter at Low Temperatures*. Imperial College Press, London, 2003.

[218] T.B. Massalski (Ed.). *Binary Alloy Phase Diagrams*. ASM International, Ohio, USA, 1990.

[219] www.crystdb.nims.go.jp. Accessed May 12, 2012.

[220] B.J. Alder and T.E.Wainwright. *J. Chem. Phys.*, 27:1208 – 1209, 1957.

[221] B.J. Alder and T.E.Wainwright. *J. Chem. Phys.*, 31:459 – 466, 1959.

[222] A. Rahman. *Phys. Rev.*, A136:404 – 411, 1964.

[223] A. Rahman. *Phys. Rev. Lett.*, 12:575 – 577, 1964.

[224] J.M. Haile. *Molecular Dynamics Simulation*. Wiley and Sons, Canada, 1992.

[225] D.C. Rapaport. *The Art of Molecular Dynamics Simulation*. Cambridge University Press, Cambridge UK, 1995.

[226] D. McQuarrie. *Statistical Mechanics*. Harper and Row, New York, 1976.

[227] D.W. Heermann. *Computer Simulation Methods*. Springer-Verlag, Berlin, 1990.

[228] M.W. Finnis and J.E. Sinclair. *Philos. Mag. A*, 50:45 – 55, 1984.

[229] L. Verlet. *Phys. Rev.*, 159:98 – 103, 1967.

[230] L. Verlet. *Phys. Rev.*, 163:201 – 214, 1968.

[231] J.M. Haile. *Molecular Dynamics Simulation*. Wiley and Sons, Canada, 1992.

[232] K.M. Udayanandan, R.K. Sathish and P. Sethumadhavan. *Micro Canonical Ensemble Some Case Studies*. South Asian Publishers PVT LTD, India, 2009.

[233] S. Nose. *Mol. Phys.*, 52:255 – 268, 1984.

[234] S. Nose. *J. Chem. Phys.*, 81:511 – 519, 1984.

[235] W.G. Hoover. *Phys. Rev. A*, 31:1695 – 1697, 1985.

[236] H.J.C. Berendsen, J.P.M. Postma, W.F. van Gunsteren, A. DiNola and J.R. Haak. *J. Chem. Phys.*, 81:3684 – 3690, 1984.

[237] J.C. Phillips. *Covalent Bonding in Crystals, Molecules and Polymers*. Univ. of Chicago Press, 1970.

[238] J. Whitesell and M. Fox. *Noncovalent Interactions and Molecular Recognition*. Jones and Bartlett, USA, 1997.

[239] G. Ali Mansoori. *Principles of Nanotechnology: Molecular-Based Study of Condensed Matter in Small Systems*. World Scientific Publishing Co. Pte. Ltd., Singapore, 2005.

[240] M.S. Daw and M.I. Baskes. *Phys. Rev. B*, 29:6443 – 6453, 1984.

[241] R.A. Johnson. *Phys. Rev. B*, 37:3924 – 3931, 1988.

[242] J.B. Adams, S.M. Foiles and W.G. Wolfer. *J. Mater. Res.*, 4:102 – 112, 1989.

[243] R.A. Johnson. *Phys. Rev. B*, 41:9717 – 9720, 1990.

[244] F. Ercolessi, M. Parrinello and E. Tosatti. *Phil. Mag. A*, 58:213 – 226, 1988.

[245] G.J. Ackland and V. Vitek. *Phys. Rev. B*, 41:10324 – 10333, 1990.

[246] A.P. Sutton and J. Chen. *Philos. Mag. Lett.*, 61:139 – 146, 1990.

[247] I. Todorov and W. Smith. 362:1835 – 1852, 2004.

[248] S.M. Foiles, M.I. Baskes and M.S. Daw. *Phys Rev. B*, 33:7983 – 7991, 1986.

[249] A.F. Voter. *Intermetallic Compounds Principles*. John Wiley and Sons, London, 1994.

[250] H. Rafii-Tabar. Physics reports. 325:239 – 310, 2000.

[251] H.H. Kart, M. Uludogan, T. Cargin and M. Tomak. *J. Non-Cryst. Solids*, 342:6, 2004.

[252] T. Cagin, Y. Qi, H. Li, Y. Kimura, H. Ikeda, W.L. Johnson and W.A. Goddard III. *MRS Symp.*, 554:43 – 48, 1999.

[253] I.T. Turodov, W. Smith, K. Trachenko and M.T. Dove. *J. Mater. Chem.*, 16:1911 – 1918, 2006.

[254] www.compsoc.man.ac.uk/ lucky/Democritus/Theory/rdf.

[255] W. Smith and T. Forester. *J. Molec. Graphics*, 14:136 – 141, 1996.

[256] M.P. Allen and D.J. Tildesley. *Computer Simulation of Liquids.* Clarendon Press, Oxford, 1989.

[257] Yngve Cerenius and Leonid Dubrovinsky. *J. of Alloys and Comp.*, 306:26 – 29, 2000.

[258] J. Akella. *J. Phys. Chem. Solids*, 43:941, 1982.

[259] Takemura Kenichi. *Phys. Rev. B*, 70:012101 (1 – 4), 2004.

[260] Florent Occelli, Daniel L. Farber, James Badro, Chantel M. Aracne, David M. Teter, Michael Hanfland, Bernard Canny and Bernard Couzinet. *Phys. Rev. Lett.*, 93:095502 (1 – 4), 2004.

[261] http://www.konabikeworld.com. Accessed July 10, 2012.

[262] Jostein Röyset. www.teksidaluminum.com. Accessed May 18, 2012.

[263] D.R. Holmes, ATI Wah Chang and Allegheny Technologies. *ASM Handbook on Corrosion: Materials (06508G).* ASM International, Ohio, USA, 2005.

[264] R.J.H. Clark. *The Chemistry of Titanium, Zirconium and Hafnium*. Pergamon Press, Oxford, UK, 1973.

[265] S.D. Cramer and B.S. Covino. *ASM Handbook*. ASM International, Metals Park (OH), 2005.

[266] J. Wallenius and D. Westlen. *Annals of Nucl. Energy*, 35:60, 2008.

[267] R.H. Nielsen. *Ullmans encyclopedia of industrial chemistry*. Weinheim VCH Verlagsgesellschaft, 1989.

[268] J.A. Davidson. *US Patent 5954724*, 1999.

[269] X.L. Meng, Y.D. Fu, W. Cai, Q.F. Li and L.C. Zhao. *Phil. Mag. Lett.*, 89:431 – 438, 2009.

[270] A. Baudry, P. Boyer, L.P. Ferreira, S.W. Harris, S. Miraglia and L. Pontonnier. *J. Phys. Cond. Matter*, 4:5025 – 5036, 1992.

[271] K. Schubert, S. Bhan, T.K. Biswas, K. Frank and P.K. Pandy. *Naturwisenchaften*, 55:704 – 705, 1968.

[272] H.J. Wallbaum. *Naturwisenchaften*, 31:91 – 92, 1943.

[273] C.E. Holcombe Jr. *J. Less-Common Met.*, 44:331 – 335, 1976.

[274] E.M. Savitsky, V.P. Polyakova, B.P. Kridin, A.A. Kozlov, and E.M. Khorlin. Nauk Publ. Moscow, 1971.

[275] P. Villars, M. Berndt, K. Brandenburg, K. Cenzual, J. Daams, F. Hulliger, T. Massalski, H. Okamoto, K. Osaki, A. Prince, H. Putz and S. J. Iwata. *J. Alloys Comp.*, 367:293 – 297, 2004.

[276] John Vaccaro. *Materials handbook*. McGraw-Hill, New York, 2002.

[277] M. Schwartz. *CRC encyclopedia of materials parts and finishes*. CRC Press, USA, 2002.

[278] W. Hume-Rothery. *Prog. in Mat. Sci.*, 13:231 – 265, 1967.

[279] L.M. Pecora and P.J. Ficalora. *Journal of Electronic Materials*, 6:531 – 540, 1977.

[280] R.P. Elliott. *Constitution of binary alloys*. McGraw-Hill, New-York, 1968.

[281] R.M. Waterstrata, A. Shapiroa and A. Jeremie. *J. of Alloys and Comp.*, 290:63 – 70, 1999.

[282] K. Upadhya, J.M. Yang and W. Hoffman. Advanced materials for ultrahigh temperature structural applications above 2000 degree celsius. www.dtic.mil. Accessed August 25, 2011.

[283] A.E. Dwight and P.A. Beck. *Metall. Trans. AIME*, 215:976 – 979, 1959.

[284] S.N. Tripathi and S.R. Bharadwaj. *J. of Phase Equilibria*, 16:527 – 531, 1995.